Bacterial traps and advances in nanobiotechnology for atomic force microscopy

THÈSE N^O 8003 (2018)

PRÉSENTÉE LE 16 MARS 2018

À LA FACULTÉ DES SCIENCES ET TECHNIQUES DE L'INGÉNIEUR

LABORATOIRE DE BIO- ET NANO-INSTRUMENTATION

PROGRAMME DOCTORAL EN MICROSYSTÈMES ET MICROÉLECTRONIQUE

ÉCOLE POLYTECHNIQUE FÉDÉRALE DE LAUSANNE

POUR L'OBTENTION DU GRADE DE DOCTEUR ÈS SCIENCES

PAR

Oliver PERIC

acceptée sur proposition du jury:

Prof. H. Shea, président du jury
Prof. G. Fantner, directeur de thèse
Prof. F. Lafont, rapporteur
Prof. G. Francius, rapporteur
Prof. J. Brugger, rapporteur

EPFL

ÉCOLE POLYTECHNIQUE
FÉDÉRALE DE LAUSANNE

Suisse
2018

That's one small step for a man,
one giant leap for mankind.
— *Neil A. Armstrong*

Abstract

The atomic force microscope (AFM) allows the analysis of living microorganisms in physiological conditions on the nanometer scale. The observation of bacteria in physiological aqueous medium necessitates a robust immobilization of the bacterium to the surface, in order to withstand the lateral forces exerted by the AFM cantilever tip during scanning. Different immobilization techniques for AFM analysis of bacteria in aqueous media have been developed hitherto, however the immobilization techniques were dependent on the bacterial species and/or the aqueous imaging medium.

We propose a robust bacterial immobilization method allowing bacterial species and medium independent analysis. We demonstrate the immobilization and AFM analysis of different bacterial species such as gram-positive and -negative, motile and non-motile, and rod-shaped, ovococcal, and crescent bacteria. The developed bacterial traps were used together with *Escherichia coli*, *Bacillus subtilis*, *Caulobacter crescentus*, *Streptococcus pneumoniae*, and *Acidiphilium cryptum* bacteria in their corresponding physiological aqueous medium.

The developed microfluidic device allows simultaneous fluorescence and atomic force microscopy of bacteria. Moreover, we developed two different cleanroom microfabrication techniques for the bacterial traps. We thus fabricated nanotailored bacterial traps, allowing the immobilization of rod-shaped bacteria along their longitudinal axis as well as by the bacterial poles.

Furthermore, we discuss the nanomechanical analysis of suspended silicon nanowires and hydrogels using the AFM. In the final part of the thesis, we explain the microfabrication method for AFM cantilevers with a low quality factor and elucidate hard tip integration into the developed multilayer AFM cantilevers.

Key words: atomic force microscope (AFM); microfabrication; microfluidics; bacterial immobilization; correlative microscopy; nanomechanical characterization; cantilever.

Zusammenfassung

Das Rasterkraftmikroskop ermöglicht die Analyse lebender Mikroorganismen unter physiologischen Bedingungen auf der Nanometer Skala. Die Analyse der Bakterien in flüssigem, physiologischem Nährmedium erfordert eine robuste Immobilisation auf der Oberfläche, um den lateralen Kräften zu wiederstehen, welche durch die Messspitze während der Messung ausgeübt werden. Bis anhin wurden verschiedene Immobilisationsmethoden für die Rasterkraftmikroskopanalyse der Bakterien entwickelt, welche aber abhängig der zu analysierenden Bakterienart und/oder des flüssigen Nährmediums sind.

Wir erläutern hier eine robuste Bakterienimmobilisierungsmethode, welche unabhängig der zu analysierenden Bakterienart oder des Nährmediums ist. Des Weiteren veranschaulichen wir die Immobilisation und Analyse der verschiedenen Bakterienarten wie grampositive und gramnegative, freibewegliche und unbewegliche, sowie stabförmige, ellipsoid-förmige und sichelförmige Bakterien. Wir benutzten unsere Immobilisationsmethode mit den Bakterien *Escherichia coli*, *Bacillus subtilis*, *Caulobacter crescentus*, *Streptococcus pneumoniae* und *Acidiphilium cryptum* in ihren entsprechenden physiologischen Nährmedien.

Wir entwickelten ein mikrofluidisches Instrument, welches eine simultane Bakterienobservation durch ein Fluoreszenzmikroskop und ein Rasterkraftmikroskop erlaubt. Des Weiteren haben wir zwei verschieden Rheinraummikrofabrikationstechniken entwickelt, welche die nanoskopisch massgeschneiderte Fabrikation unserer Bakterienimmobilisierungsmethode ermöglichte, dass wir anhand der Immobilisation stabförmiger Bakterien entlang der Längsachse, sowie auch anhand den abgerundeten Enden.

Des Weiteren erläutern wir die nanomechanische Analyse von Siliziumnanodrähten sowie auch von Hydrogels. Im letzten Teil der Thesis veranschaulichen wir den Rheinraummikrofabrikationsprozess von Rasterkfraftmikroskopmessspitzen, den sogenannten cantilever, welche einen tiefen Qualitätsfaktor besitzen, und erläutern die Integration harter Messspitzen.

Zusammenfassung

Stichwörter: Rasterkraftmikroskop; Mikrofabrikation; Mikrofluidik; Bakterienimmobilisierung; korrelative Mikroskopie; nanomechanische Charakterisierung; Messspitze.

Résumé

Le microscope à force atomique (AFM) rend possible l'analyse des microorganismes vivants dans des conditions physiologiques à l'échelle nanométrique. L'observation des bactéries dans un milieu aqueux et physiologique nécessite une immobilisation robuste des bactéries à la surface afin de résister aux forces latérales exercées par le cantilever de l'AFM pendant l'acquisition d'image. Jusqu'à présent, plusieurs méthodes d'immobilisation des bactéries pour l'analyse avec l'AFM dans les milieux aqueux ont été développées. Celles-ci sont toutefois dépendantes des souches bactériennes et/ou du milieu aqueux.

Nous proposons une méthode robuste d'immobilisation des bactéries qui permet une analyse de celles-ci indépendemment de leur souche ou du milieu aqueux. Nous démontrons qu'une immobilisation et une analyse par l'AFM de bactéries avec des propriétés différentes telles que gram-positives et –négatives, mobiles et immobiles ainsi que des bactéries en forme de tige, de croissant et ellipsoïdes est possible. Le dispositif pour l'immobilisation des bactéries a été utilisé avec les bactéries *Escherichia coli*, *Bacillus subtilis*, *Caulobacter crescentus*, *Streptococcus pneumoniae*, et *Acidiphilium cryptum* dans leur milieu aqueux et physiologique correspondant.

Le dispositif microfluidique que nous avons développé permet une observation simultanée de bactéries à travers un microscope à fluorescence et un AFM. De plus, nous avons développé deux techniques différentes de micro-fabrication pour les pièges bactériens. Nous avons en outre fabriqué des pièges bactériens nanoscopiques permettant l'immobilisation de bactéries en forme de tige par l'axe longitudinale ainsi que par les pôles.

De plus, nous traitons de l'analyse nanoméchanique de nanofils de silicium encastrés ainsi que d'hydrogels en utilisant l'AFM. Dans la partie finalisant la thèse nous expliquons la méthode de microfabrication des cantilevers d'AFM ayant un facteur de qualité bas et nous concluons en abordant l'intégration des pointes dures dans les cantilevers à multicouches d'AFM.

Mots clefs : microscope à force atomique (AFM) ; microfabrication ; microfluidique ; immobilisation des bactéries ; microscopie corrélative ; caractérisation nanomécanique ; cantilever.

Contents

Contents

List of Figures

List of Tables

Abbreviations

AFM atomic force microscope

AMP antimicrobial peptide

BCB benzocyclobutene

CMC carboxymethyl-cellulose

CMOS complementary metal oxide semiconductor

e-beam electron beam

FEA finite element analysis

FET field effect transistors

HF hydrofluoric acid

KOH potassium hydroxide

LB lysogeny broth

LPCVD low pressure chemical vapor deposition

LPS lipopolysaccharide

MEMS microelectromechanical system

MIC minimum inhibitory concentration

NIL nanoimprint lithography

PDMS polydimethylsiloxane

Abbreviations

PEG polyethylene glycol

PI propidium iodide

PPA polyphthalaldehyde

PYE peptone yeast extract

QNM quantitative nanomechanical mapping

RIE reactive ion etching

SEM scanning electron microscope

SiN silicon nitride

SiNW silicon nanowire

SiO$_2$ silicon dioxide

SOI silicon on insulator

STM scanning tunneling microscope

t-SPL thermal scanning probe lithography

TEM transmission electron microscope

UV ultraviolet

1 Introduction to atomic force microscopy of living samples

1.1 Imaging at nanometer scale

The observation of a sample using light and a set of lenses, in order to magnify objects barely visible by eye, is limited by the diffraction of light. Abbe formulated this lateral resolution limitation with the wavelength of light, λ, and the numerical aperture of the imaging lens, NA, through $\lambda/2$NA [1]. Therefore, in order to observe two objects as such, the distance between the objects has to be larger than roughly half the wavelength of light. Yet optical microscopes are an essential tool in every laboratory setup.

Continuous technical improvements allowed to surpass the diffraction limitation by near-field techniques using surface plasmons [2], or by far-field fluorescence techniques as demonstrated through the different super-resolution optical microscopy techniques [3]. Most recent advances in far-field fluorescence nanoscopy resolved objects being six nanometers apart, which allowed imaging of molecular structures inside living bacteria [4].

Using electrons instead of photons decreases the distance to resolve two objects, since the de Broglie wavelength of an electron is three orders of magnitude smaller than the wavelength of visible light, thus allowing nanometer lateral resolution [5]. Electron microscopes such as the scanning electron microscope (SEM) and transmission electron microscope (TEM) rely on a vacuum chamber for sample analysis. For this purpose, biological samples had to be prepared following particular protocols and the observation was limited to dead samples [6]. Only recent technical advances, in particular by using a fluid cell inside the vacuum chamber, made it possible to use electron microscopy on samples in liquid, allowing the observation of living bacteria [7].

1

An entirely different approach for imaging at the nanometer scale is achieved by the AFM. Invented over thirty years ago, the AFM is inherently suitable for imaging samples with nanometer precision in vacuum, in air, as well as in aqueous environments [8].

The beginning of the AFM takes place at IBM in Zürich and starts with the invention of the scanning tunneling microscope (STM) [9, 10]. The STM visualized of the atomic structure of the sample surface [11] by measuring the tunnel current between the sharp tip apex of the STM probe and the sample surface. To enable the analysis on non-conductive sample surfaces, Binnig *et al.* placed a cantilever with a sharp tip under the STM probe and thus created the AFM [8]. The deflection of the cantilever was read out by the tunnel current, whereas the cantilever deflection was a function of interaction forces at the sample surface. Hence, the topography of samples, independent of the sample material was achievable at the nanometer scale. Although the samples were analyzed in air or in vacuum, medium independent AFM analysis was made possible by replacing the STM probe with an optical read-out, allowing nanometer resolution even in aqueous environments [12]. Through further technological advances of the AFM, observations of dynamic phenomena in microbiology were enabled [13, 14].
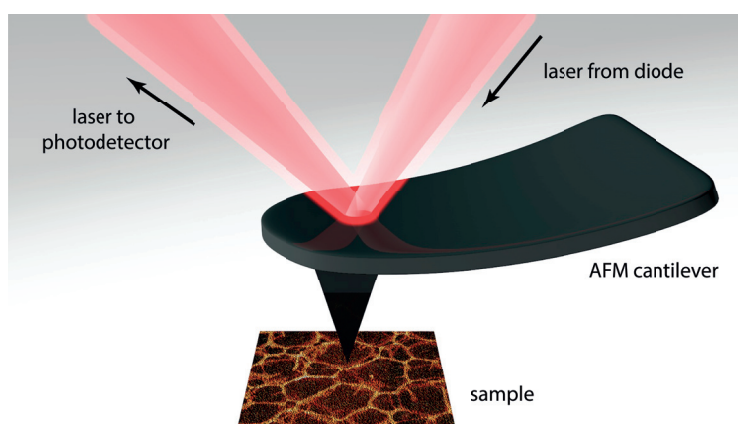
Figure 1.1 – Simplified working schematics of an AFM. A laser diode is reflected from a bent AFM cantilever during sample analysis and the deflection is measured by a photodiode.

Although the cantilever deflection can be read out by various methods, the most common read-out method is a laser beam that is reflected on the cantilever surface and read out by a photodetector, as shown in figure 1.1. The sample is imaged by moving the cantilever in-plane, or in some AFM systems the sample stage, with a piezoelectric actuator. In order to follow the topography during imaging, the vertical cantilever position, or in some AFM systems the vertical sample stage position, is controlled through an additional piezoelectric actuator. Various different modes of operation of an AFM exist, and here only

the most common modes are explained that is found in commercially available AFMs.

In contrast to optical and electron microscopy, the AFM is a scanning probe microscopy technique, allowing nanometer scale observation of samples by three-dimensional reconstruction of the sample topography. Through the repulsive or attractive interaction forces between the sample surface and the AFM cantilever tip apex, additional information of the sample can be obtained during scanning. Nanomechanical properties of the sample can thus be extracted during the data acquisition of the sample topography. Furthermore, by functionalizing the cantilever tip surface, the deflection of the cantilever can be a function of e.g. magnetic or biomolecular forces, alongside e.g. van der Waals forces or electrostatic forces, opening the utilization of the AFM to broad field of applications [15, 16]. Recent advances combine the power of the AFM with super-resolution far-field fluorescence microscopy to extract novel findings from the two complementary imaging techniques [17].

1.2 AFM imaging modes

While various imaging modes of the AFM exist, the focus will be given on three main imaging modes used in the experiments of this thesis. The imaging modes are *contact mode*, *tapping mode*, and *off-resonance tapping*, whereas the later mode is commercially known as *PeakForce quantitative nanomechanical mapping (QNM)*®, *HybriD Mode™*, *QI™ mode*, *Pulsed Force Mode™*, or jumping mode, and is referred to as QNM throughout this manuscript. These modes distinguish themselves in particular by a different feedback and actuation, which is used to control the vertical z-position of the cantilever. In contact mode, the deflection of the cantilever is fed back and maintained constant. In tapping mode, the cantilever is oscillating and the amplitude of the oscillation is maintained constant. The main benefit of this mode is that the interaction with the sample is more gentle as compared to contact mode, where a soft sample can easily be damaged by the cantilever tip. In QNM mode the cantilever is as well oscillating, although the feedback is not the oscillation amplitude of the cantilever such as in tapping mode, but the main feedback parameter is the exerted force of the cantilever tip on the sample. The tip-sample interaction can be controlled with a higher precision and the imaging sensitivity is therefore higher as compared to the tapping mode. Softer samples can thus be imaged without damage.

In QNM, every data point bears not only the sample topography information, but as well the material properties such as adhesion and elastic modulus. This information is extracted from each force curve, schematically depicted in figure 1.2.
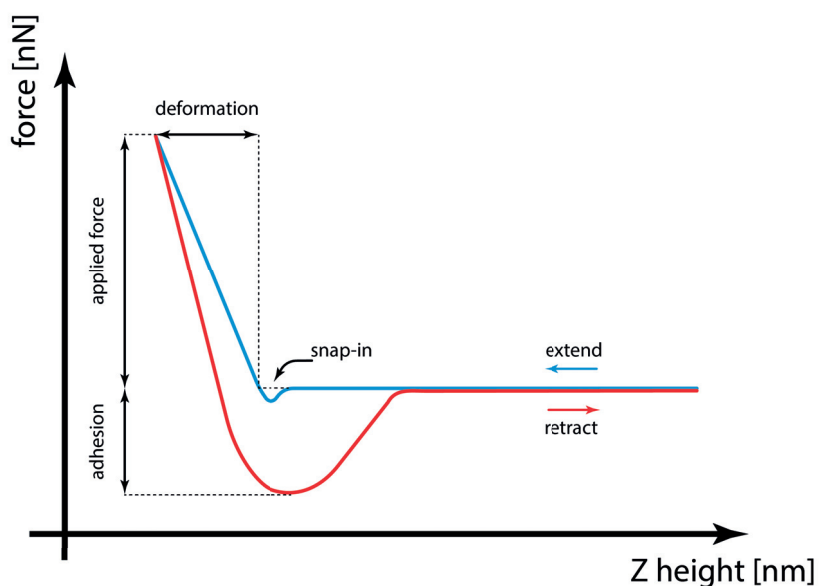
Figure 1.2 – Schematic force curve of an AFM indentation during the cantilever tip and sample interaction allowing the extraction of material properties.

From the indentation of the cantilever tip into the sample, the elastic modulus of the sample can be extracted [18]. To have an accurate measurement, the cantilever has to be correctly calibrated [19, 20, 21]. The calculation of the elastic modulus depends on the tip-sample interaction and is different for hard versus soft samples. The mathematical model established by Hertz [22] was further developed in order to include the adhesion forces [23, 24, 25]. When the indentation depth of the cantilever tip into the sample is higher than the cantilever tip diameter itself, which is typically the case for soft samples, the model proposed by Sneddon gives a more accurate estimation of the elastic modulus [26]. Nevertheless, when the sample is covered with a brush-like layer, which is typically the case for bacteria with envelope structures such as lipopolysaccharides and pili, the brush model allows a more accurate description of the elastic properties [27, 28, 29].

1.3 AFM imaging of bacteria in aqueous solutions

AFM analysis of living samples bares various difficulties. On one side, the living sample has to be robustly immobilized on the substrate, and on the other hand, the living sample has to be kept alive. Moreover, living samples such as eukaryotic cells, bacteria, and other unicellular microorganisms can exhibit mechanisms of locomotion. While the mechanics and biophysics of microbial locomotions have been intensively studied [30, 31], the

routine analysis of dynamic processes on the bacterial envelope at the nanometer scale still remains a challenge.

Many bacteria have dimensions in the range of hundreds of nanometers to a few micrometers. This length scale is difficult to address with optical microscopy, and resolving details on the surface of living cells is nearly unattainable with optical or electron microscopy methods. In contrast, the AFM is inherently well-suited for nanoscale characterization of living cells. The analysis of the bacterial surface with nanometer precision was achieved on a routinely basis over two decades ago with electron microscopy techniques [32]. The main drawback was that bacteria had to be prepared through special protocols, where the imaged bacteria were dead, thus the analysis of dynamic changes on the bacterial envelope was not possible.

As described in section 1.1, experiments with the AFM in liquid medium were done shortly after the invention of the AFM itself, allowing the study of live microorganisms with nanometer precision. Pioneering AFM images of mammalian cells in physiological buffers [33] and the isolated bacterial envelope in liquid [34, 35] showed the great potential of AFM analysis in liquid for microbiology [12]. More recent findings elucidate the mechanical properties of type IV pili, found to play a key role in bacterial attachment to biotic and abiotic surfaces [36]. Furthermore, the peptidoglycan architecture of *Bacillus subtilis* bacteria was determined to be a coiled-coil model [37], and observations on genetically identical *Escherichia coli* bacteria showed that the reaction is very different at the nanoscale when treated with the same antibiotic [13]. The results obtained with AFM complement findings by traditional methods and expand our knowledge of biological systems [38, 39].

Nevertheless, the broad use of AFM in microbiology has in part been limited by difficult sample preparation. Particularly for the observation of living bacteria under physiological conditions, the immobilization of bacteria on the surface is challenging [40, 41]. Various immobilization techniques were developed over the years and can be classified in two distinct categories: chemical substrate modification [42] or physical immobilization of bacteria [43].

1.3.1 Immobilization by chemical surface modification

For the chemical treatment of the substrate, typically a mica or glass surface, a coating with poly-*L*-lysin is commonly used alongside with polyethylenimine (PEI) or gelatin. The substrate surface is functionalized with positive charges, leading to the immobilization of the negatively charged bacterial envelope [44]. Covalent binding of the bacterial envelope

to the substrate can be achieved by functionalizing a surface with amine groups, carboxyl groups, or glutaraldehyde [45]. Nevertheless, substrate modification methods often perform poorly in physiological buffers or compromise the bacterial viability [45, 46]. Bacteria often fail to adhere strongly enough to the substrate [47] and higher forces applied by the AFM tip can detach a bacterium [48], as depicted in figure 1.3.

(a) Bacterial immobilization by chemical treatment of the substrate.

(b) Physical immobilization of bacteria using a millipore filter.
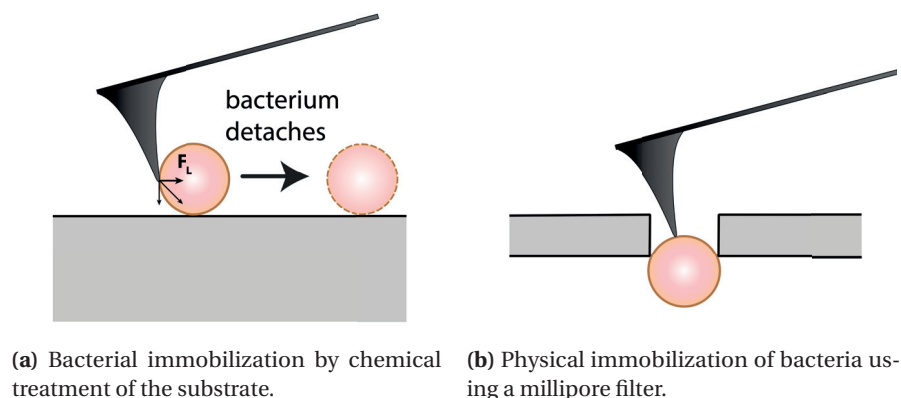
Figure 1.3 – Schematics of different bacterial immobilization techniques.

Bacterial immobilization protocols for AFM using chemical surface modification are numerous [49, 50], but the robustness of the immobilization depends on the targeted bacterial strain, as the following example illustrates. Specific gram positive (*Staphylococcus aureus*) as well as gram negative (*Escherichia coli*) bacteria showed superior attachment to gelatin coated substrates compared to poly-L-lysin substrate coatings [51]. However, the same gelatin substrate coating did not allow adequate immobilization of *Synechococcus leopoliensis*, a different gram negative bacterial species [52], even though the same immobilization protocol was followed [53].

Therefore, standard immobilization protocols with chemical substrate modification often have to be modified [54] or new protocols have to be developed [55]. The optimal coating depends strongly on the bacterial species and strain, as well as the surrounding liquid imaging medium. Furthermore, the bacterial envelope properties are altered when the bacterium is attached to a chemically modified surface, which can additionally trigger bacterial responses and compromise the analysis of the bacterial viability [45, 46, 56, 57].

1.3.2 Physical immobilization

Physical immobilization of bacteria is considered the most reliable method [58]. Pioneering results were achieved in millipore filters, enabling the study of yeast cells [43] and

coccoid bacteria [59]. These passive physical immobilization methods are very suitable for round shaped microorganisms, but cannot be reliably used to immobilize microbes of other shapes such as rod-shaped or filamentous bacteria.

The physical immobilization leaves the bacterial envelope chemically intact and allows a reliable and robust immobilization. Proven techniques using filter pores were further improved [60] and new physical immobilization methods were developed. Pits patterned in a substrate allow bacterial immobilization after bacteria settle into the traps through evaporation of the liquid medium [61], or bacteria need to be centrifuged into poly-dimethylsiloxane (PDMS) channels [62].

A reversible trapping at well-defined positions is favorable for the repeatability of the experiment, without the need for tedious sample exchange and preparation. Moreover, correlative AFM/optical microscopy imaging is of particular interest, to correlate surface topography with specific intracellular components, thereby making use of the many fluorescence probes available in microbiology.

Compared to bacterial immobilization by chemical modification of the substrate surface, where a glass cover slip can act as an ideal substrate for correlative AFM/optical microscopy imaging, the substrate for physical immobilization of bacteria has to be carefully chosen in order to allow simultaneous AFM and optical microscopy. A strong, robust immobilization for correlative AFM/optical microscopy is still lacking, which is in particular compatible with AFM imaging under physiological conditions and independent of the bacterial species.

1.4   Bacterial traps: concept and design

In order to obtain an aqueous medium independent bacterial immobilization and combine the benefits of current immobilization techniques for correlative microscopy, we propose a microfluidic device with active immobilization. Bacteria are physically immobilized in V-shaped traps, where the lateral forces of the AFM tip during scanning are counteracted by the slanted walls, as depicted in figure 1.4.

To guide bacteria towards the traps, we propose pressure-driven flow, allowing trapping and releasing of bacteria on demand. To be fully compatible with optical microscopy, the device must be transparent from the bottom-side. The microfluidic device would thereby allow fluorescence microscopy from the bottom-side and AFM imaging in liquid from the top-side. Our proposed physical immobilization method is visualized in figure 1.5
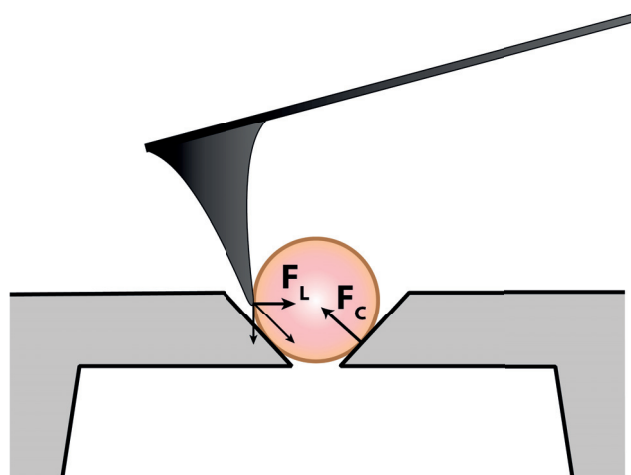
Figure 1.4 – Schematic of the proposed physical immobilization method.

Our idea is to fabricated the assembly compounds of the microfluidic device from chemically inert materials, considering that microfluidic devices made from PDMS may influence cell behavior; uncrosslinked oligomers can interact with microorganisms, and hydrophobic molecules from the medium can be absorbed into the PDMS, which could lead to experimental artifacts [63].

Moreover, our proposed physical immobilization method should be independent of the envelope composition of rod-shaped bacteria, the surrounding liquid medium, and the bacterial sample preparation. Ideally, AFM analysis could be conducted immediately after placing a drop of the bacterial suspension on top of the assembled microfluidic chip. This would allow a versatile application across a multitude of bacterial species and liquid media.

1.5 Thesis overview

After a brief introduction to AFM at the beginning of this chapter, we discussed in section 1.3 the difficulties of bacterial analysis with the AFM in aqueous media and the state of the art in bacterial immobilization methods. Our approach for a reliable AFM analysis of bacteria under physiological conditions is a microfluidic device using physical immobilization, described schematically in section 1.4.

In chapter 2, we will first explain the microfabrication of the bacterial traps. We will
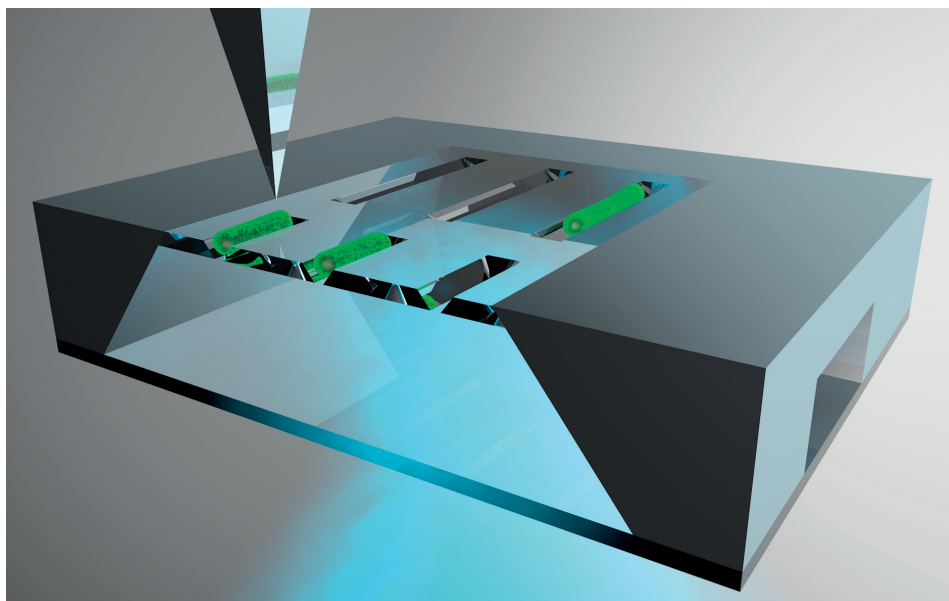
Figure 1.5 – Visualization of the microfluidic physical immobilization method using simultaneous AFM and fluorescence microscopy.

discuss two different technological approaches with an in depth insight into the critical aspects of the cleanroom microfabrication. Section 2.2.1 describes the materials and methods of bacterial traps used for most of the experiments in the laboratory, whereas section 2.3.1 describes a novel microfabrication approach based on thermal scanning probe lithography, enabling various fabrication and experimental possibilities as discussed in detail in section 2.5.

In chapter 3 thereafter, we will discuss the experimental results obtained with the fabricated bacterial traps. Our proposed bacterial immobilization approach enabled not only a species independent topographic and nanomechanical analysis of bacteria, but as well allowed simultaneous fluorescence analysis. Using the LIVE/DEAD BacLight fluorescent stain, we opened the door to a detailed analysis of the killing behavior of specific antibiotics and their effects on the bacterial envelope with correlative observation of the bacterial viability. Furthermore, the AFM analysis as well as fluorescent observations of different bacterial strains were conducted in the laboratory with various aqueous media including the physiological buffer medium for each strain. During the experimental work done with the bacterial traps in the scope of this thesis, we have used bacteria of the following species: *Escherichia coli*, *Bacillus subtilis*, *Caulobacter crescentus*, *Streptococcus pneumoniae*, and *Acidiphilium cryptum*.

We demonstrate in chapter 4 the application of the AFM on two additional, entirely

different classes of samples. In section 4.2, we investigated the mechanical properties of silicon nanowires, elucidating the bending of the nanowires under different loads in QNM mode and further investigating their stiffness and point of fracture due to the forces applied by the AFM tip. In section 4.3, we analyzed two different types of hydrogels, which can be referred to as soft materials as compared to nanowires, and in addition discussed their elastic moduli.

Chapter 5 details a novel fabrication method for multi-layer AFM cantilevers consisting of a polymer core sandwiched between two hard layers. We show the improvement of the fabrication yield and discuss the integration of hard tips onto the multi-layer cantilevers. The thesis is summed up by chapter 6 containing the conclusion and outlook of the future generation of bacterial traps.

This thesis contains partially verbatim text and images that were published in a peer reviewed journal [64].

2 Microfabrication and assembly of the bacterial traps

2.1 Introduction

Many bacteria have dimensions in the range of hundreds of nanometers to a few micrometers. The silicon-based microfabrication technology is therefore most suitable to fabricate the bacterial traps. We rely on standard, established cleanroom microfabrication tools and technology such a electron beam (e-beam) lithography, photolithography, dry and wet etching, but use as well micro- and nanofabrication methods in a novel context, such as thermal scanning probe lithography (t-SPL).

The cleanroom microfabrication was done entirely in our microfabrication facility CMi, whereas t-SPL was done in collaboration with in the laboratory of Prof. Jürgen Brugger together with Yuliya Lisunova. The implementation of the fabricated bacterial traps into a microfluidic assembly was done by taking into account design rules in order to maintain compatibility with our laboratory AFM/optical microscope setups.

In this chapter we first explain in detail two different microfabrication approaches in sections 2.2 and 2.3 and describe the design of the microfluidic device embedding the bacterial traps in section 2.4. We discuss in detail the advantages and drawbacks of the two presented microfabrication approaches in section 2.5. The fluid flow characterization described in section 2.2.2 was done for bacterial traps made by the silicon on insulator (SOI) wafer based approach, but can be extended to the t-SPL technology approach for bacterial traps with same dimensions.

2.2 Microfabrication based on SOI wafers

We rely on the nanometer resolution of e-beam lithography to define the shape of the bacterial traps and use lower resolution microfabrication techniques, such as standard photolithography and xurography, for the microfluidic parts, including channels and connection ports [65, 66]. We have developed a cleanroom process flow based on e-beam lithography, involving SOI wafer technology, and have optimized the process flow throughout multiple iterations as explained in section 2.2.1 hereafter. We discuss the final process flow along with initial fabrication results and highlight critical points of the microfabrication. The detailed process flow used in our microfabrication facility CMi is given in appendix A.

2.2.1 Process flow based on SOI wafers

For the fabrication of the slanted walls of the bacterial traps, we rely on the anisotropic etch properties of potassium hydroxide (KOH) on monocrystalline silicon. Through the KOH wet etching of (1 0 0) silicon, we obtain a slanted edge with an angle of 54.7° for the etched pattern, which translates directly into the shape of the bacterial traps.

In order to connect the bacteria in aqueous medium on the top side of the microfluidic chip with the microfluidic channel underneath, the bacterial traps need to be open a the bottom. A SOI wafer is advantageous in multiple points, assuming the thickness of the silicon device layer on the top side of the wafer has the required value. On one hand, the silicon device layer thickness translates directly into the depth of the bacterial trap. We used SOI wafers with a silicon device layer thickness of 340 nm, which is just under the radius of the rod-shaped bacteria *E. coli* and *B. subtilis*. From the microfabrication point of view on the other hand, the oxide layer of the SOI wafer is an important advantage, because KOH etching of the device silicon layer is significantly reduced by reaching the oxide layer, and the oxide layer can be removed with hydrofluoric acid (HF), which does not affect the silicon [67].

The main steps of the cleanroom process flow are depicted in figure 2.1. We used silicon nitride (SiN) as the etch mask for KOH etching and first deposited a 100 nm thick SiN layer through low pressure chemical vapor deposition (LPCVD) in a furnace (c.E2000, Centrotherm) at temperatures ranging between 820° C and 850° C (figure 2.1a). The positive e-beam resist ZEP520A (Zeon Chemicals) with a thickness of 125 nm was used as a mask for e-beam lithography on the top-side of the SOI wafer (figure 2.1b), and standard positive photoresist (AZ 1512, Microchemicals) with a thickness of 1.7 μm was used for

(a) Step 1: LPCVD of SiN on a SOI wafer.

(b) Step 2: E-beam lithography on the top side and consecutive dry etching.

(c) Step 3: Photolithography on the back side of the wafer.

(d) Step 4: First KOH wet etching.

(e) Step 5: Top side protection with a protective polymer coating.

(f) Step 6: Second KOH wet etching.

silicon   silicon nitride   silicon dioxide

protective polymer   lithography resist

(g) Step 7: Chip by chip HF etching.
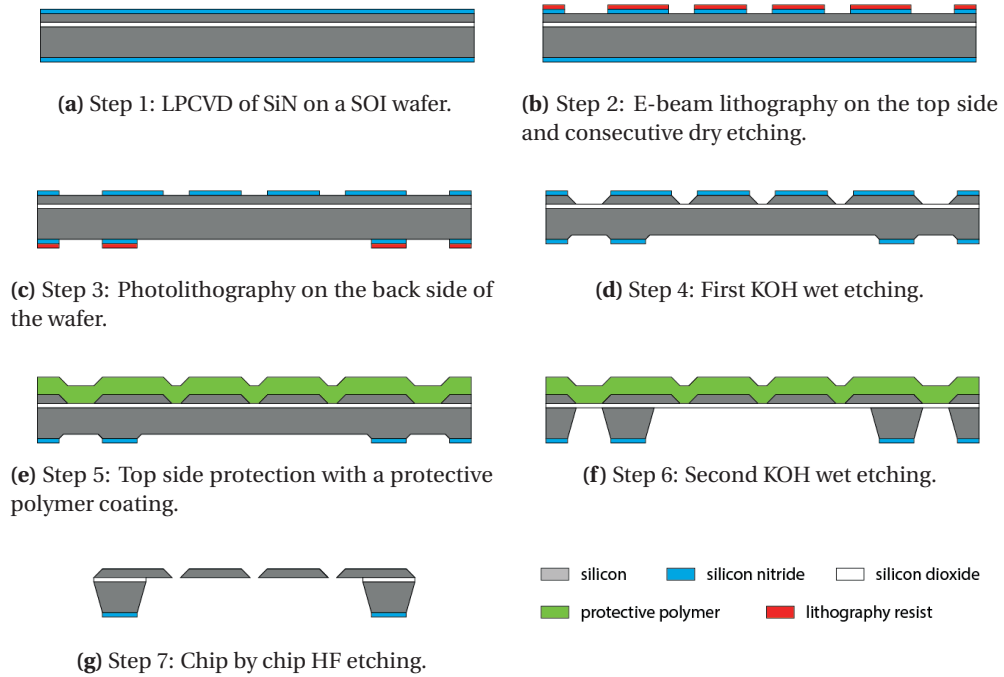
Figure 2.1 – The main microfabrication steps of the SOI process flow.

the back side patterning of the SiN layer (figure 2.1c). SiN etching was done by reactive ion etching (RIE) using a He (175 sccm), H_2 (30 sccm), and C_4F_8 (10 sccm) based plasma mixture (LPX, SPTS Technologies) with a total etch time of 40 s. The top-side anisotropic etching of silicon was done in 40% KOH solution for 3 min at 60° C (figure 2.1d), until the silicon dioxide (SiO_2) layer was reached.

Initial designs of the top-side mask contained a SiN pattern as shown in figure 2.2a. This design was chosen in order to compensate for an eventual misalignment of the e-beam pattern in regard to the crystalline silicon axis of the SOI device silicon layer. The removal of the SiN hard mask after KOH etching by RIE was problematic, since the fluorocarbon plasma etched the underlying silicon layer, even though a process with high selectivity of 1:9 (Si:SiN etch rate) was applied. The SiN pattern was transferred into the silicon layer and the slanted walls of the bacterial trap were overetched, as shown in figure 2.2b. Both images of figure 2.2 show the SiO_2 layer underneath the SOI device silicon layer in the center of the bacterial traps.

In order to not damage and overetch the silicon structures by the dry etching of SiN, we left the SiN layer intact. By alignment the SOI wafer flat to the e-beam lithography wafer holder using an optical microscope, we did not observe a misalignment of the patterns
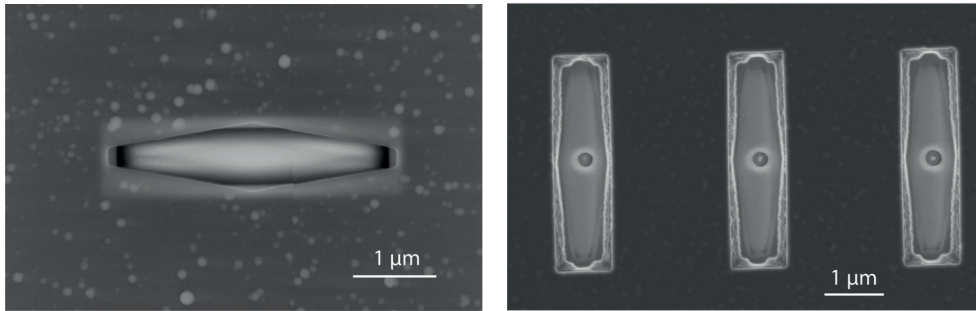
(a) SEM image after KOH etching with the SiN hard mask containing a misalignment compensation design.

(b) SEM image after KOH etching followed by a RIE dry etching of the SiN hard mask.

Figure 2.2 – SEM images after KOH etching of the bacterial traps with (a) and without (b) a SiN hard mask. The center of the bacterial traps shows the underlying SiO$_2$ layer of the SOI wafer.

written by e-beam lithography with the crystalline axis of the SOI device silicon layer. The top-side features of the wafer were protected from the second KOH wet etching using a 6 μm thick top-side protective polymer layer (ProTEK B3, Brewer Science) as shown in figure 2.1e. In the final version of the process flow, the ProTEK layer was spin-coated on top of the SiN after the first KOH etch step.

In detail, after an oxygen plasma surface activation for 30 s at 200 W, we first deposited the ProTEK Primer by spin-coating with a rotation of 1500 rpm for 60 s and an acceleration of 1000 rpm s^{-1}. The primer was baked at 205° C for 60 s on a hotplate. Thereafter, the ProTEK layer was dispensed directly from the beaker due to its viscosity and was spin-coated with a rotation of 1500 rpm for 60 s and an acceleration of 1000 rpm s^{-1}. We used two consecutive baking steps on two different hotplates, where the first baking step was done at 120° C for 120 s and the second baking step was done at 205° C for 60 s.

The KOH etching on the back side of the wafer was done for approximately 6 h in 23% KOH solution at 90° C (figure 2.1f). The etching was stopped when the membrane containing the bacterial traps was visible, indicating a through-wafer etch. The top-side protective and supporting polymer layer stayed intact during the back side KOH etching.

In addition to protecting the top silicon layer against KOH etching, the protective polymer layer served as a mechanical support for the microfluidic chips. Therefore, no silicon support bridges were required to hold the chips after the KOH wafer etch through. Thus, we were able to adapted the shape of the microfluidic chips to have a square design. In order to obtain a square shape after KOH etching of a silicon wafer with a crystalline plane (1 0 0), etch compensation structures on all convex corners are needed [68]. This is due to
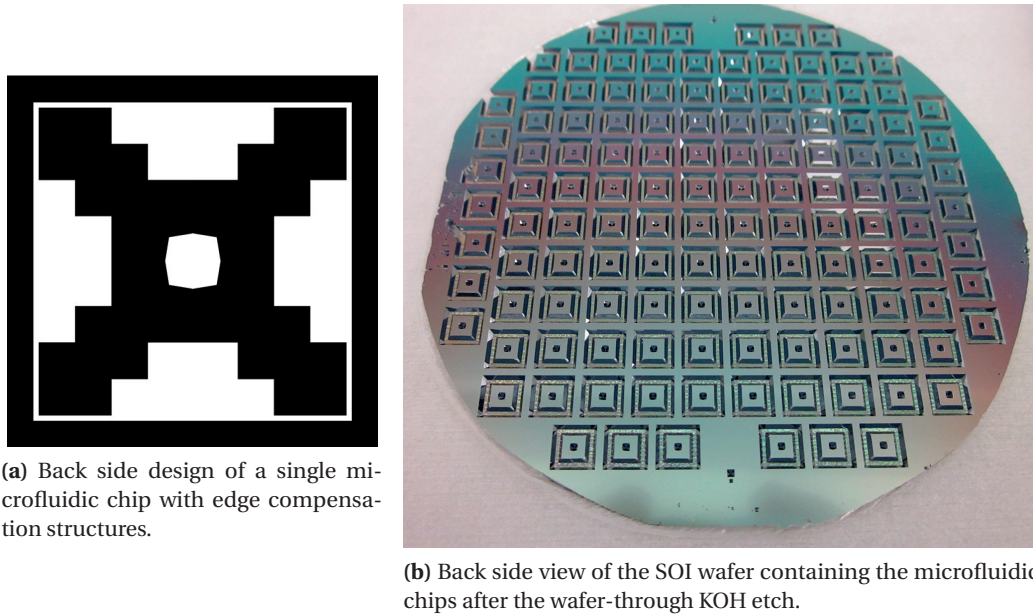
(a) Back side design of a single microfluidic chip with edge compensation structures.

(b) Back side view of the SOI wafer containing the microfluidic chips after the wafer-through KOH etch.

Figure 2.3 – Back side design of a single microfluidic chips with edge compensation structures for an 740 μm thick SOI wafer and the result after wafer-through KOH etching on the full wafer scale.

the fact that different crystalline silicon directions have different etch rates [69]. The etch rate ratio of the equivalent directions $\langle 1\,0\,0\rangle$ and $\langle 1\,1\,0\rangle$ is one to two orders of magnitude higher in respect to the $\langle 1\,1\,1\rangle$ direction, as reported in the literature [70, 71, 72].

The design was done with the CleWin layout editor (PhoeniX Software) and is shown for a single chip in figure 2.3a. We simulated the design thereafter with the Anisotropic Crystalline Etch Simulation (ACES) [73] prior to microfabrication and we found that the results were coherent with the simulation after the wafer-through etching.

All chip patterns for the back side photolithography of the wafer contained corner compensation structures for a 740 μm thick SOI wafer. We first measured the thickness of the wafer and adapted the design of the corner compensation structures to the thickness of the bulk silicon of the SOI wafer. The pattern of the central square hole was adapted in order to compensate at the concave corners for an eventual misalignment during back side photolithography, which could results after KOH etching in a membrane with larger dimensions than foreseen, thus making the membrane more fragile. The four-inch wafer containing 126 chips with bacterial traps is depicted from the back side in figure 2.3b.

The etching of the SiO_2 layer after KOH wafer-through etching was done in 50% HF on a chip-by-chip level for 3 min with light agitation of the chip. The ProTEK layer, which stayed intact during the over 6 h long etch in KOH at 90° C, pealed off during the etching

(a) Bright-field optical microscope image of the top side of a microfluidic chip. The arrows indicate the placement of the bacterial traps.

(b) Close-up SEM image of a single bacterial trap showing the slanted silicon walls.

(c) SEM image of a bacterial trap array.

(d) SEM image of an array with a long bacterial traps variant.
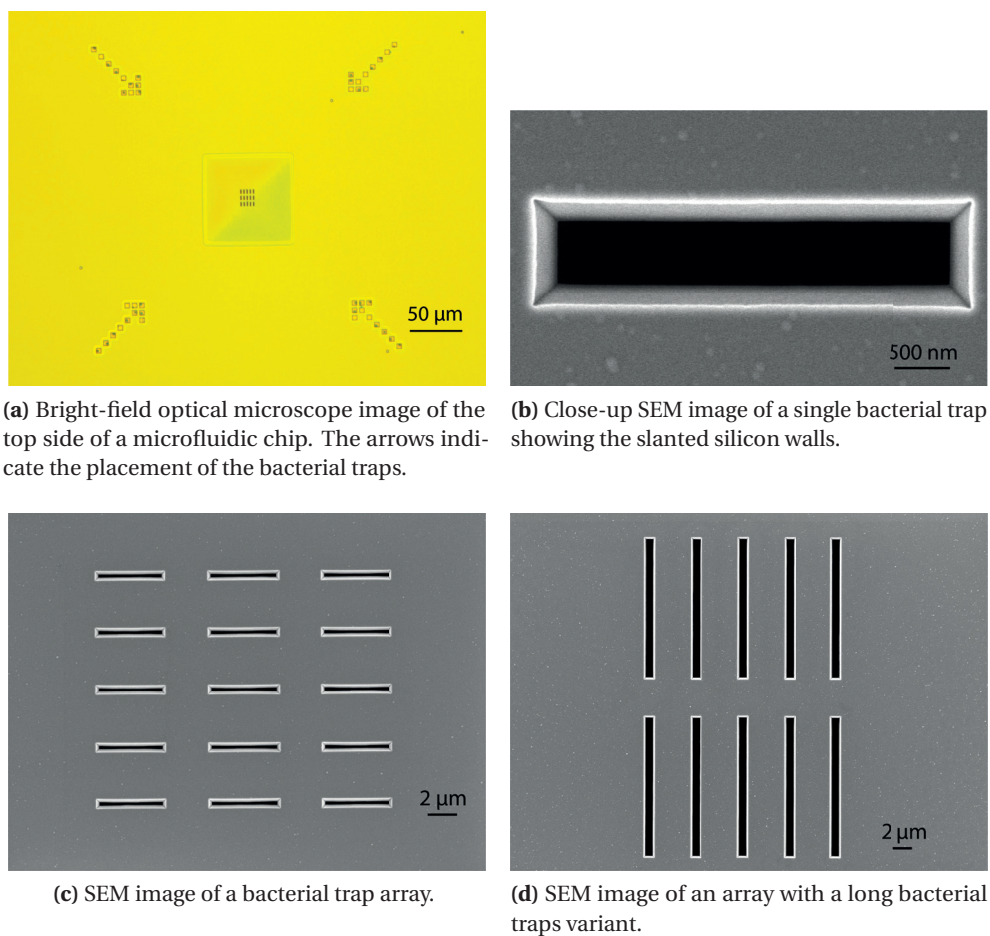
Figure 2.4 – Top side view of the microfluidic chip and SEM images of bacterial traps.

of the silicon dioxide layer in 50% HF. HF is known to peal off photoresist, when a high concentrations (higher than 1:3 volume ratio with water) are used [74] and we found that 50% HF peals off as well the protective ProTEK polymer layer. Therefore, no further cleaning with oxygen plasma was necessary to remove the ProTEK layer. The microfluidic chip at the end of the process flow is depicted in figure 2.1g.

A bright-field optical microscope image is shown in figure 2.4a showing the bacterial traps on the membrane. The arrows in the corners are patterned in order to make the characterization with the SEM during the microfabrication process straightforward, as well as for optical searching during AFM imaging of immobilized bacteria. Figure 2.4b shows a SEM image of a single bacterial trap at the end of the process flow highlighting the slanted walls and the bottom opening of the trap, whereas figures 2.4c and 2.4d depict arrays of bacterial traps with different dimensions.

2.2.2 Fluid characterization

In order to understand the microfluidic conditions around the bacterial traps during immobilization, we used finite element analysis (FEA), to first simulate the flow around the traps, as shown in figure 2.5. The maximum velocity for water passing through the bacterial traps was 75 mm s^{-1} for an applied pressure across the membrane of -20 mbar, as used during our experiments discussed throughout chapter 3. This translates to a volume flow ranging between $18.0 \cdot 10^{-4}$ and $45.6 \cdot 10^{-4}$ μl min^{-1} for the trap array designs used during the experiments described in section 3.2.
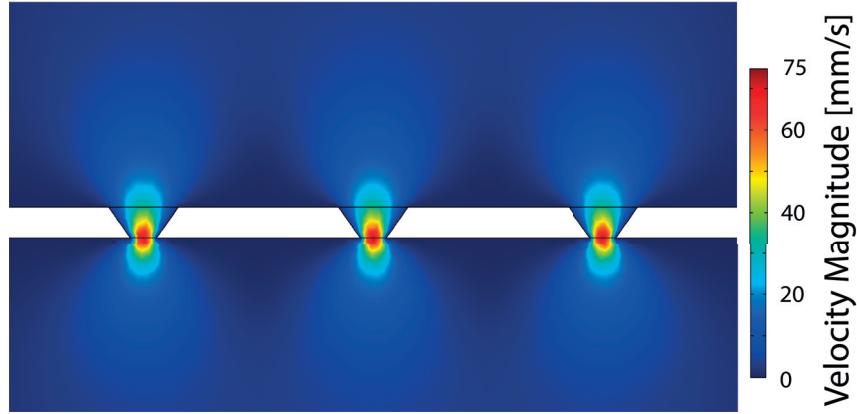
Figure 2.5 – Simulation of the flow velocity around the traps in a cross section of the membrane. The applied pulling pressure below the membrane is -20 mbar, to match experimental conditions.

Our estimation of the force acting on a trapped bacterium due to the applied pressure difference is approximately 6 nN, which is in the order of magnitude for lateral AFM forces exerted on a bacterium during scanning [48]. The force approximation is based on a bacterium modeled as a cylinder with a diameter D and a length L. The force applied on an infinitesimal surface is $\delta \vec{F} = \Delta P \cdot \mathrm{d}A \cdot \vec{n}$ where ΔP is the difference of pressure between the two sides of the surface, $\mathrm{d}A$ is an infinitesimal surface and $\vec{n}$ is a unit vector normal to the surface. After integration on the whole surface of the bacterium we get equation 2.1.

$$\vec{F} = \iint_{\Sigma} \Delta P \cdot \vec{n} \cdot \mathrm{d}A = (P_1 - P_2) \, D \cdot L \cdot \vec{u}_z \tag{2.1}$$

where Σ is the bacterial surface, P_1 is the pressure underneath the traps, P_2 the atmospheric pressure and $\vec{u}_z$ a vertical unit vector. For a bacterium with $D = 900$ nm, $L = 3.5$ μm and an applied pressure of $|P_1 - P_2| = 20$ mbar, we obtain a force $F = 6.3$ nN that is acting on the bacterium.

It is important to note that this calculation is only intended as an approximation to show the order of magnitude of the resulting forces on a trapped bacterium. The actual forces acting on bacteria can deviate significantly, for instance, when the exposed area of the bacterium to the bottom part of the trap is smaller or when the bacterium only partially populates the trap, allowing fluid to pass through.

The pressure difference across the membrane is only necessary for the trapping process and can be completely switched off during AFM analysis. A bacterium does not need to be kept immobilized by the applied pressure difference, since the slanted walls of the bacterial traps counteract the lateral forces exerted by the AFM tip during scanning, which is an empowering feature of the proposed immobilization technique.

We used COMSOL Multiphysics 4.4 for the FEA of the fluid flow through the bacterial traps. The interface between the solid (silicon) and the liquid (water) part of the model was defined through a no-slip boundary condition. At the opening below the membrane, defined as the outlet, and initial pressure of -20 mbar was set, as used during the experiments. The liquid above the membrane had open boundary conditions, whereas the liquid below the membrane was confined through the silicon walls of the 3D model. For the volume flow analysis we integrated the velocity field in the direction of fluid motion, over the surface of the traps from COMSOL, taking into account the fluid flow as function of the no-slip boundary condition.

2.3 Microfabrication using thermal scanning probe lithography

Thermal scanning probe lithography (t-SPL) [75] enables 3D nanopatterning in a thin film resist with a vertical resolution down to 1 nm [76]. This feature, coupled to the recent advances in direct pattern transfer using dry etching [77], allows fabrication of complex geometries of controlled dimension into the target material such as silicon, SiN, and SiO_2. Hence, t-SPL enables rapid prototyping on the nanoscale.

We employed the t-SPL technique to fabricate bacterial traps in SiO_2 allowing the immobilization of bacteria for AFM imaging in liquid, regardless of the bacterial shape or size. We developed a process flow allowing the fabrication of microfluidic compatible SiO_2 membranes containing 3D structures with a predefined geometrical shape and slope profile. The developed process was demonstrated on SiO_2 nanostructures as well as with low stress silicon nitride and stoichiometric silicon nitride (Si_3N_4).

This work was achieved together with my collaborator Yuliya Lisunova from the Microsystems Laboratory LMIS1. In particular the t-SPL patterning of the resist with the

commercial tool NanoFrazor from SwissLitho and the consecutive pattern transfer into the subjacent layer by RIE was done together with Yuliya's developed etching parameters [77]. The detailed process flow used in our microfabrication facility CMi is given in appendix B.

2.3.1 Process flow based on t-SPL

To fabricate the bacterial traps, we followed the lithography and etch process steps schematically illustrated in figure 2.6. We started with a four-inch, double sided polished silicon wafer with a 500 nm SiO_2 layer on both sides. Using standard photolithography, we patterned the top and back side SiO_2 layer of the wafer. The back side patterns contain the outlines of the microfluidic chips with convex corner compensation structures for KOH etching [68], as depicted in the aforementioned figure 2.3a.

Aligned to the back side, we patterned the top side SiO_2 layer using photolithography with marks defining the area destined for the bacterial traps. The placement of the t-SPL patterns is crucial, since the bacterial traps obtained at the end of the process flow are situated on a square membrane with dimensions of roughly 50 μm, and the location of the membrane is defined by the back side pattern.

(a) Step 1: Photolithography on the top side and back side with consecutive dry etching of SiO_2.

(b) Step 2: Thermal scanning probe lithography on the top side of the wafer.

(c) Step 3: Pattern transfer through dry etching.

(d) Step 4: Top side protection with a protective polymer coating and consecutive KOH wet etching.

(e) Step 5: Protective polymer removal through oxygen plasma.

	silicon		silicon dioxide
	protective polymer		PPA resist

Figure 2.6 – The main microfabrication steps of the t-SPL process flow.

The patterned SiO_2 layer was removed after every photolithography step on each wafer side using RIE with a He (175 sccm), H_2 (30 sccm), and C_4F_8 (10 sccm) based plasma mixture (LPX, SPTS Technologies) with a total etch time of 2 min 30 s as shown in fig-
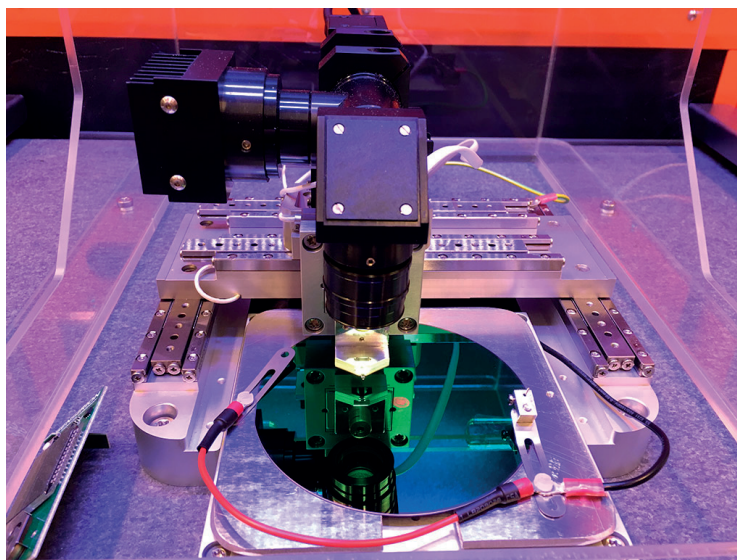
Figure 2.7 – Wafer-scale patterning of the PPA resist by t-SPL using the instrument NanoFrazor developed by SwissLitho.

ure 2.6a. After thorough cleaning of the wafer, 4% of polyphthalaldehyde (PPA) dissolved in cyclohexanone (≥99.5%, Sigma Aldrich) was spin coated on the top side of the wafer to a thickness of 115 nm. The wafer was prebaked on a hotplate at a temperature 90° C for 3 min, which allowed the residual solvents to evaporate. The final PPA film thickness of 100 nm was measured by a surface profilometer (Dektak XT).

T-SPL PPA patterning (figure 2.6b) and topography imaging, were carried out with the commercially available instrument NanoFrazor Explore (SwissLitho) outside of the cleanroom, as depicted in figure 2.7. We applied a heater temperature of 800° C at a force pulse durations of 10 μs. The force load was optimized to the desired pattern depth. The patterns were written at scan speeds of 1-3 mm s^{-1} and a pixel size of 20 nm. The 3D patterns of the bacterial traps were written in the prepatterned targeted area on the top side of the wafer. In order to achieve the correct pattern depth in the PPA layer, we first optimized the t-SPL writing parameters, such as writer voltage and write pulse duration, in the proximity of the targeted bacterial traps pattern area.

Figure 2.8 depicts patterns of a bacterial traps showing slanted walls obtained in the PPA resist for the longitudinal trapping of rod-shaped bacteria as well as round traps destined for coccoid bacteria or trapping of rod-shaped bacteria by the poles, as performed experimentally in our laboratory describes in section 3.4.1.

Initially we spin coated the PPA resist on a silicon wafer with a 500 nm thick low-stress
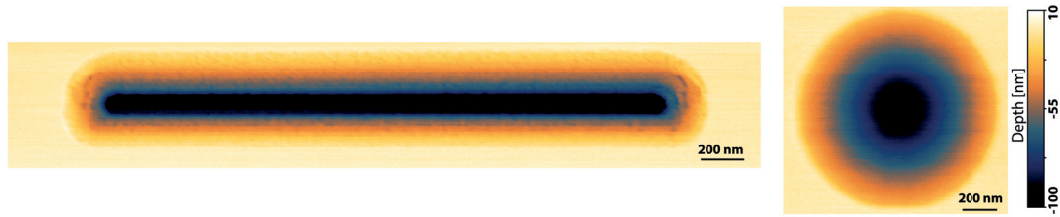
Figure 2.8 – Patterning of the PPA resist on SiO$_2$ by t-SPL of a bacterial trap for longitudinal trapping of rod-shaped bacteria (left) and round shaped traps (right). Both patterns have a maximal depth of 100 nm with a defined, sloped edge.

silicon nitride layer. The t-SPL patterning was possible as shown in figure 2.9, but the high surface roughness of the underlying SiN layer was directly transferred into the PPA patterns. This high surface roughness, as well visible in the SEM image of figure 2.2a, is a knows issue of the LPCVD of low-stress silicon nitride inside the Centrotherm c.E2000 furnace of our microfabrication facility, at the point when the experiments were done. For this reason, we decided to use SiO$_2$ since the surface roughness values (arithmetical mean deviation of all points on the topography map) were 7.1 Å instead of 40.6 Å as for low-stress silicon nitride. Even though stoichiometric silicon nitride showed a surface roughness value of 5.2 Å, the 500 nm thick Si$_3$N$_4$ layer was not suitable as a KOH etch mask for wafer-through etching. We observed a crack formation in the Si$_3$N$_4$ layer on the whole wafer that exposed the underlying silicon, which was as well attacked during the KOH etch at 60° C.

The transfer of the bacterial trap patterns into the subjacent SiO$_2$ layer was done using a He (175 sccm), H$_2$ (18 sccm), and C$_4$F$_8$ (15 sccm) based plasma mixture (LPX, SPTS Technologies) with an etch selectivity between the PPA resist and the SiO$_2$ layer of 1:5.4 [77]. In order to adjust the thickness of the PPA layer according to the etch selectivity ratio, we first thinned down the PPA layer with oxygen plasma, resulting in a PPA thickness of 93 ± 3 nm prior to RIE etching. Thus, the consecutive RIE etching of 1min 45s resulted in a complete pattern transfer into the SiO$_2$ layer. Therefore, through the RIE process, we obtained a transfer of the 100 nm PPA resist layer into the 500 nm silicon dioxide layer, as shown in figure 2.6c.

The surface topography of the transferred pattern was analyzed with the AFM (Bruker Dimension, Fast scan head) as shown in figure 2.10a. The depth profile of a bacterial trap pattern before and after the pattern transfer is shown in figure 2.10b. The profiles were taken from the t-SPL pattern in figure 2.8 (left), compared and manually overlaid with the depth profile of the AFM image in figure 2.10a.

For the consecutive KOH wet etching, we protected the top side of the wafer using ProTEK
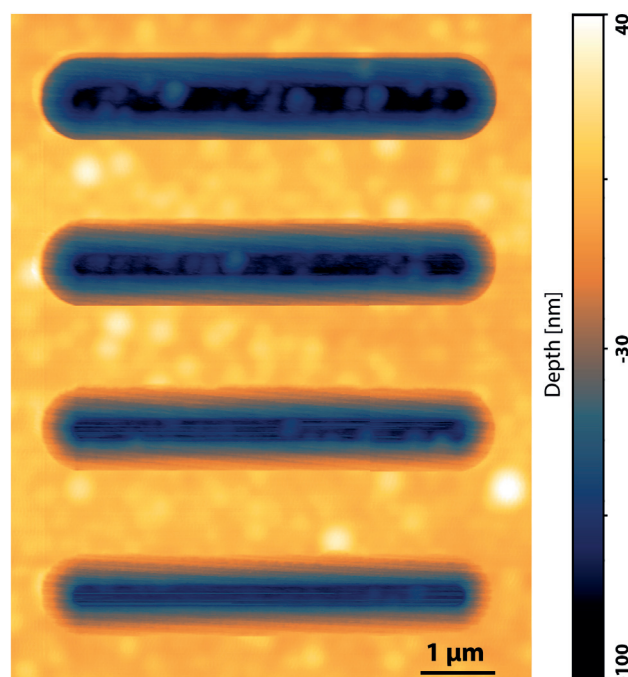
Figure 2.9 – Patterning of the PPA resist on low-stress silicon nitride by t-SPL of a bacterial trap for longitudinal trapping of rod-shaped bacteria. All patterns have a maximal depth of 100 nm with a defined, sloped edge. The patterns were written using different NanoFrazor heater temperatures and force pulse durations, in order to determine the correct t-SPL patterning parameters.

(B3, Brewer Science) with the same parameters as discussed in section 2.2.1. The SiO_2 that is thermally grown in water vapor, also referred to as *wet oxide*, can be considered as a very poor KOH etch mask and is also being etched in the KOH bath [67]. Therefore we modified the KOH wet etch parameters in order to obtain a wafer-through etch before the 500 nm thick SiO_2 mask on the back side of the wafer was fully etched away.

For the used 380 μm thick wafer we used a 20% KOH solution and etched at 35° C for roughly 77 h in a bath with continuous stirring. During this time period only ~350 nm of SiO_2 would etch, which is less than the used SiO_2 layer thickness of 500 nm, while the 380 μm of silicon would be etched through [78]. During the microfabrication, we observed that the SiO_2 mask remained intact after the long KOH etching.

In order to remove the native oxide and define the starting point of etching, we used an identical KOH bath at 60° C and placed the wafer in the bath until the H_2 gas bubbles were visible. Immediately thereafter we placed the wafer in the 35° C KOH bath until the wafer-through etch was done (figure 2.6d). Finally, the protective polymer layer was removed with O_2 plasma on a chip-by-chip basis as shown in figure 2.6e. The SEM images of round and long bacterial traps on the SiO_2 membrane at the end of the process flow are
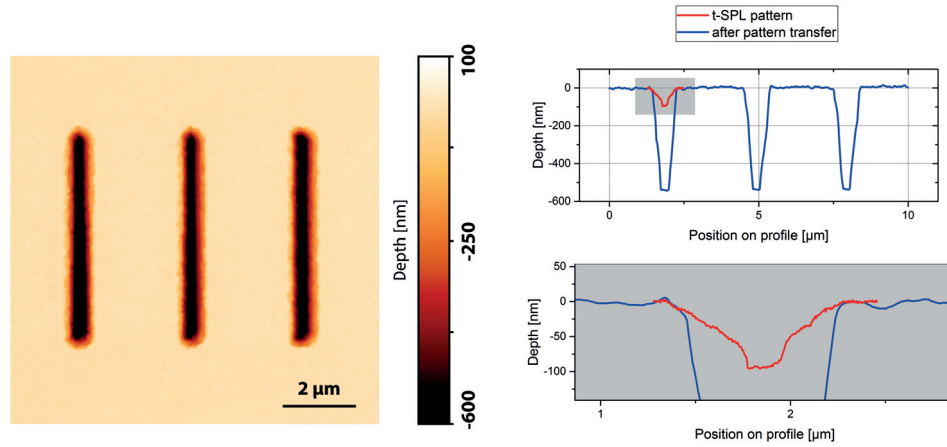
(a) AFM image of the transferred t-SPL pattern into SiO_2.

(b) Depth profiles of the t-SPL pattern overlaid with the transferred pattern into SiO_2. The gray area shows a close-up view of the marked area.

Figure 2.10 – AFM analysis of the t-SPL pattern after the pattern transfer into SiO_2 showing a maximal depth of the pattern of 500 nm. The profile of the pattern written by t-SPL into PPA is overlaid with the AFM profile of the transferred pattern for the comparison of the depth profiles before and after pattern transfer into the SiO_2 layer.

depicted in figure 2.11. The obtained bacterial traps correspond to the patterns shown in figure 2.8. The spacing between individual bacterial traps in the array of figure 2.11b was performed in order to evaluate different t-SPL design parameters.
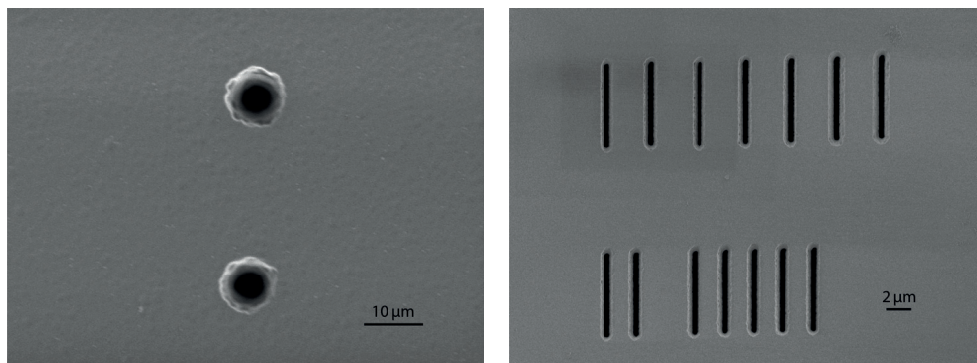
(a) SEM of round t-SPL patterns at the end of the process flow.

(b) SEM of the long t-SPL patterns variant at the end of the process flow.

Figure 2.11 – SEM image of t-SPL patterns at the end of the process flow, transfered into the SiO_2 membrane.

23

2.3.2 Heat transfer analysis of t-SPL

Although patterning of PPA on full wafer scale was repeatedly feasible, we encountered difficulties of PPA patterning on pre-fabricated silicon nitride membranes. In both cases, we spin-coated a PPA film on the substrate with a final thickness of 100 nm, whereas the substrate consisted of a 500 nm thick low-stress SiN layer. Although the final micro-fabrication process flow is based on SiO_2 as discussed in section 2.3.1, the first approach using t-SPL was done on a SiN layer. We switched to SiO_2 due to the high surface roughness of low-stress silicon nitride and the failure of 500 nm thick stoichiometric silicon nitride (Si_3N_4) as a KOH etch mask. The study in this section was originally done for a 500 nm thick low-stress SiN layer, but can be extended to the used SiO_2 layer, since the specific heat of low-stress SiN and SiO_2 are in the same order of magnitude [79, 80] and their thermal conductivity is at least an order of magnitude higher than for polymers [81].

During the t-SPL patterning, in the case of a thick silicon layer underneath the patterning spot as shown in figure 2.12a, the bulk silicon acted as an excellent thermal conduction layer. When the SiN layer was suspended, forming a membrane as shown in figure 2.12b, the silicon nitride layer became the predominant component for the heat dissipation originating from the t-SPL tip. The temperature of the membrane around the patterning spot rose within the t-SPL contact pulse time of 10 μs to values above the decomposition temperature of PPA [82, 83, 84], as illustrated in figure 2.13. Exceeding the second decomposition temperature maximum of PPA at 194° C resulted in imminent burning of the resist on the membrane, as we've experienced during our experiments.

(a) SiN with bulk silicon underneath.   (b) SiN as a membrane.
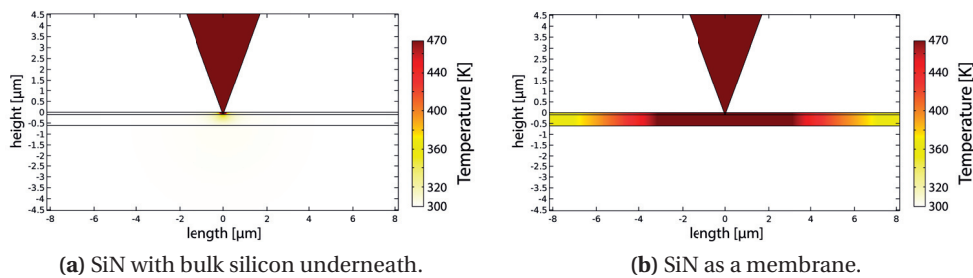
Figure 2.12 – Heat transfer analysis during t-SPL. Both figures show the state at 10 μs after indentation of the tip for pattern writing.

For the heat transfer simulation in COMSOL we modeled a contact area of 10 nm between the heated cantilever tip and the substrate. The tip had a half-cone angle of 20 deg and a temperature of 800° C, corresponding to average values used during our experiments. We used standard values for all material properties as given by COMSOL or found in literature [80, 83]. The simulated results in figure 2.12 depict the temperature state at 10 μs with

a tip indented 90 nm into the PPA, a depth that we've repeatedly used during the t-SPL patterning.
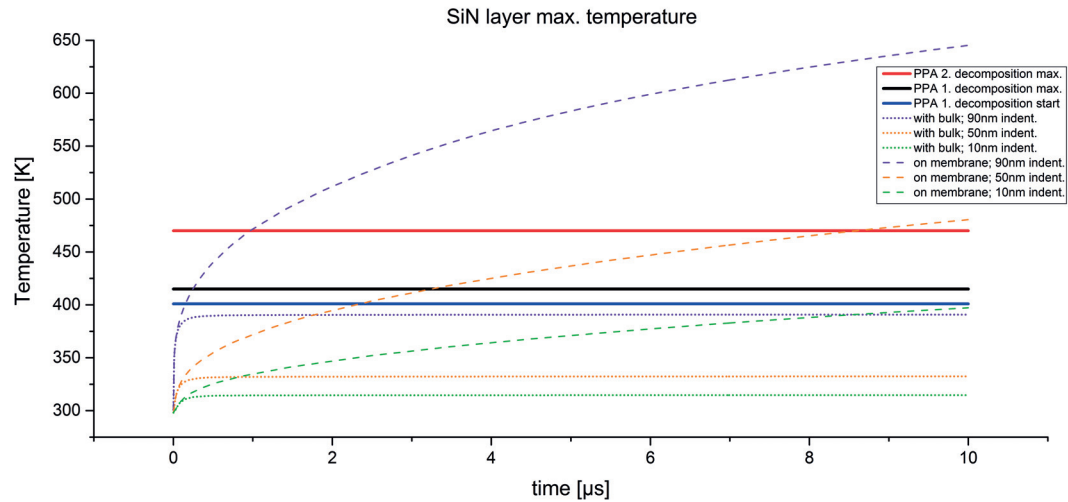
Figure 2.13 – SiN layer temperature versus PPA decomposition temperature for three different indentation depth. While the SiN with bulk silicon remains under the PPA decomposition temperature, the SiN membrane temperature rises above the allowed maximal PPA decomposition temperature within the 10 μs contact time during t-SPL patterning.

The heat transfer between the tip and the substrate can occur through radiation or conduction. The effects of radiation of a heated tip in proximity of the surface are negligible versus the effects of conduction [85, 86]. Moreover, the thermal conductivity of air and nitrogen gas, as used during our t-SPL patterning experiments, are significantly smaller at room temperature than the thermal conductivity of polymers or the underlying layer of silicon nitride [80, 87, 88]. We therefore consider only the effects of heat conduction through direct contact for the COMSOL simulations shown in figure 2.12.

Detailed heating behavior at the tip-sample interface including heat transfer by phonon scattering [83, 89, 90] and quantized effects at the nanoscale [91] were not considered for this heat transfer simulation. The discussed FEA simulation gives an estimation of the heat transfer effects during t-SPL patterning and correlates with our observations made during t-SPL patterning on SiN membranes as well as on layers of SiN layer with bulk silicon underneath. Therefore, we suggest to use t-SPL for patterning on layers that have a subjacent layer with good thermal conductivity, such as bulk silicon, even though pre-patterning using standard photolithography needs to be done for advanced chip designs.

2.4   Assembly and implementation into laboratory setup

2.4.1   Assembly of the microfluidic device

During the development of the bacterial traps, we significantly modified the assembly of the fluidic device. The first approach consisted of an assembly with only two parts: a SOI part containing bacterial traps on the top side and a microfluidic channel with connection holes on the back side, and a glass part that was assembled with the SOI part through anodic bonding. One main drawback of this approach was that after the assembly, the parts were irreversibly bonded together due to the anodic bonding, which presented a major challenge in respect of cleaning the device after an experiment with bacteria. Another drawback was that we could fabricate only 14 devices out of one SOI wafer as compared to 126 devices per SOI wafer of the final generation, as shown in figure 2.14.
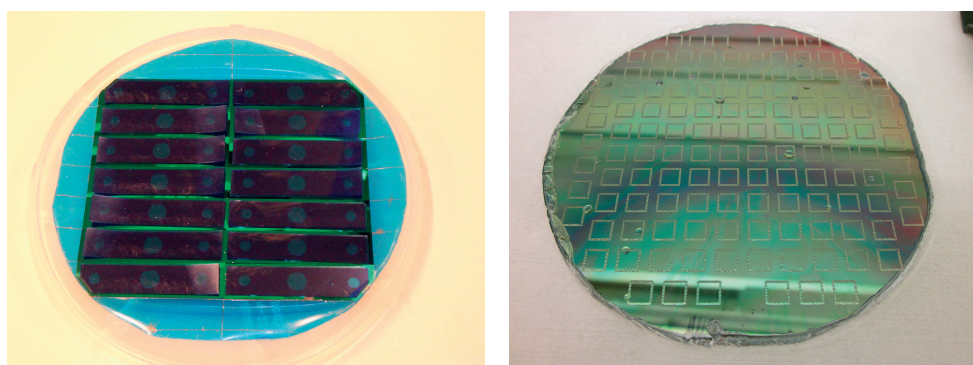
(a) First generation of SOI wafer devices. The blue tape was used in order to protect the back as well as the front side of the wafer during wafer dicing.

(b) Final generation of SOI wafer devices. There are 126 device underneath the ProTEK layer on the top-side of the SOI wafer.

Figure 2.14 – Comparison between the first (left) and final (right) generation of devices obtained per SOI wafer.

The yield of the anodic bonding was around 50% as experienced during the microfabrication, which by taking into account the initial cost of an SOI wafer and the microfabrication processing cost, resulted in a significant investment for a single assembled microfluidic device. The cost per experiment is even more pronounced given the poor reusability of this first generation assembly approach. We have therefore modified the whole assembly, baring in mind the factors reusability and devices per wafer, due to the design constraints given by the AFM head and our laboratory experiment setup described in section 2.4.3.

The final generation of the assembly of the fluidic device is schematically depicted in figure 2.15. In order to obtain more devices per wafer, we fabricated the bacterial traps on

a microfluidic chip with dimensions of 4 by 4 mm. This microfluidic chip is assembled into a silicon holder containing a square hole in the center and an inlet and outlet hole spaced 15 mm from the center. The holes were obtained by a wafer etch-through, whereas the pattern was written using standard photolithography.
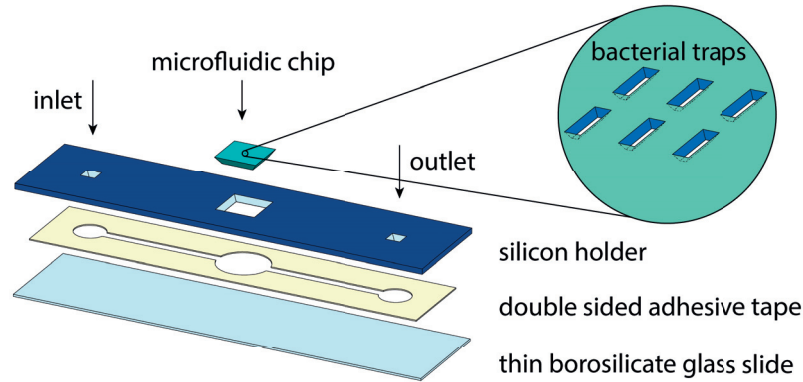
Figure 2.15 – Schematics of the parts and layers involved in the assembly of the microfluidic chip.

Dimensions of the microfluidic chip were chosen to maximize the number of devices per wafer on one side, and still have an acceptable handling possibilities in the cleanroom. In particular during the last processing step, which is HF etching on a chip by chip level, the microfluidic chips need to be handled with tweezers under full chemical protection. Therefore, the design was strongly influenced by practical cleanroom handling possibilities. The chips-per-wafer amount is given by the minimal dimensions of the chip and the dimensions of the convex corner compensation structures on the back side patter of the SOI wafer.

Instead of anodic bonding, we used a double sided adhesive tape (FAD 100S, FLEXcon) with a thickness of 100 μm to bind the glass slide to the silicon holder. The glass slide was diced out of a 200 μm thick borosilicate wafer (MEMPax, Schott) in the dimensions 40 by 10 mm, identical to the dimensions of the silicon holder. The double sided adhesive tape had 1 mm smaller dimensions on all sides for practical purposes, since the assembly is done manually by hand in our laboratory. For the patterning of the fluidic channel into the double sided adhesive tape, connecting the inlet of the silicon holder, with the microfluidic chip and the outlet, we used the xurography technique [92]. Xurograpy uses a small blade in oder to pattern a thin film, which can be transferred to a substrate. We used a cutting plotter (Craft ROBO Pro, Graphtec) to pattern the fluidic channel onto the double sided adhesive tape, since the critical dimensions of the fabricated features are one to two orders of magnitude higher than the resolution of the cutting plotter.

Furthermore, by using an adhesive tape as the binding element between the glass slide and the silicon holder, the assembly can be dismantled by soaking the microfluidic device in acetone overnight. The parts can be thoroughly cleaned and reused for a consecutive experiment. This is one main advantage as compared to the first generation device using the anodic bonding technique.

The microfluidic chip is placed in the central square hole of the silicon holder and a water resistant adhesive (2 Ton Epoxy, Devcon) is applied on the edges in order to seal the chip. The microfluidic chip assembly is depicted in figure 2.16a, whereas the first generation of the microfluidic chip with the monolithic design is shows in figure 2.16b for comparison.

(a) Assembly of the microfluidic chip shown on a standard microscope glass slide.

(b) Microfluidic chip with the first generation monolithic design.
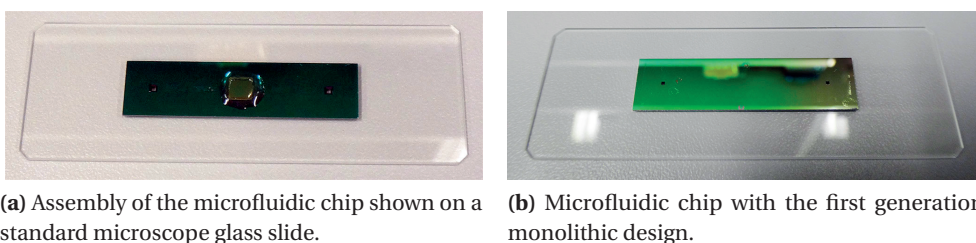
Figure 2.16 – Microfluidic chip assembly done with the fabricated parts on a standard microscope glass slide, in comparison with the first generation of the bacterial traps with a monolithic design.

Referring to the aforementioned clean room process flow of the SOI wafer discussed in section 2.2.1, the microfluidic chip is by far the most expensive part of the assembly. Nevertheless, the assembly design can be improved further. Instead of the glass slides with custom dimensions, which need to be diced out of a thin borosilicate wafer with low autofluorescence values, we can simply modify the design to use standardized microscope cover glasses (e.g. 22 by 22 mm cover slips) that have a thickness of 170 μm and were already optimized for fluorescence microscopy. For this purpose, the design of the custom aluminum mount discussed in section 2.4.3 would need to be adjusted in order to be compatible with the AFM cantilever holder.

2.4.2 Reusability of the microfluidic device

We developed the microfluidic chip assembly to allow a high reusability. After every experiment, we soaked the microfluidic chip assembly in acetone overnight, in order to dissolve the double sided sticky tape and detach the borosilicate glass slide from the silicon holder. Moreover, the acetone weakened the bond between the silicon holder and the epoxy glue around the microfluidic chip. All parts were thoroughly rinsed with milli-Q water and cleaned with a piranha solution (H_2SO_4:H_2O_2 in volume ratio of 3:1) at 100° C

for 15 min. Then, all parts were rinsed twice in milli-Q water and blow-dried with nitrogen before reassembly.

We have found that oxygen plasma is as well suitable for the cleaning of the disassembled parts of the microfluidic chip. We used oxygen plasma at 1000 W for 15 min to 30 min in order to clean the microfluidic chip and checked the openness of the bacterial traps with a SEM. Best cleaning results were achieved by combining both, piranha cleaning followed by oxygen plasma cleaning. We are able to have an immobilization of bacteria with the microfluidic chip during every conducted experiment, assuming the correct dimensions of the bacterial traps in respect to the diameter of the bacteria are chosen.

Overall, we have performed over 200 independent AFM immobilization experiments by re-using the microfluidic chips on different AFM setups discussed in section 2.4.3. Between 90 and 100 experiments were conducted in order to optimize various device parameters such as bacterial trap design, microfluidic chip assembly and design, applied pressure values, used AFM cantilever, cleaning techniques, as well as AFM imaging parameters together with correlated fluorescence microscopy. The reusability of the microfluidic chips allows a significant reduction of the overall costs per experiment, since the fabrication of new microfluidic chips from an SOI wafer is coupled with high initial cost per wafer as explained in more detail in section 2.5.

2.4.3   Implementation into laboratory setup

The microfluidic chip assembly described in section 2.4.1 is embedded in a custom aluminum mount that contains fluid connections. The final assembly of the microfluidic device with all involved parts is depicted schematically figure 2.17.

The microfluidic connections were made using standardized Luer lock connectors. We assembled two hypodermic needles with a female Luer lock on the aluminum mount as depicted in figure 2.18a, allowing an easy to use connection with the attached pressure controller (AF1 Dual, Elveflow). The pressure difference across the bacterial traps was created by clogging the outlet (left or right needle in figure 2.18a) and controlling the pressure on the inlet (complementary needle) with the pressure controller.

In order to be compatible with any physiological conditions of analyzed bacteria, such as aqueous solution containing sulfuric acid as shown in section 3.4 , we made two distinct versions of the top part holder for the microfluidic chip assembly. The top part, which is in direct contact with the aqueous solution, exists therefore in aluminum as well as a polymeric material showing excellent resistance to sulfuric acid as depicted in figure 2.18b.
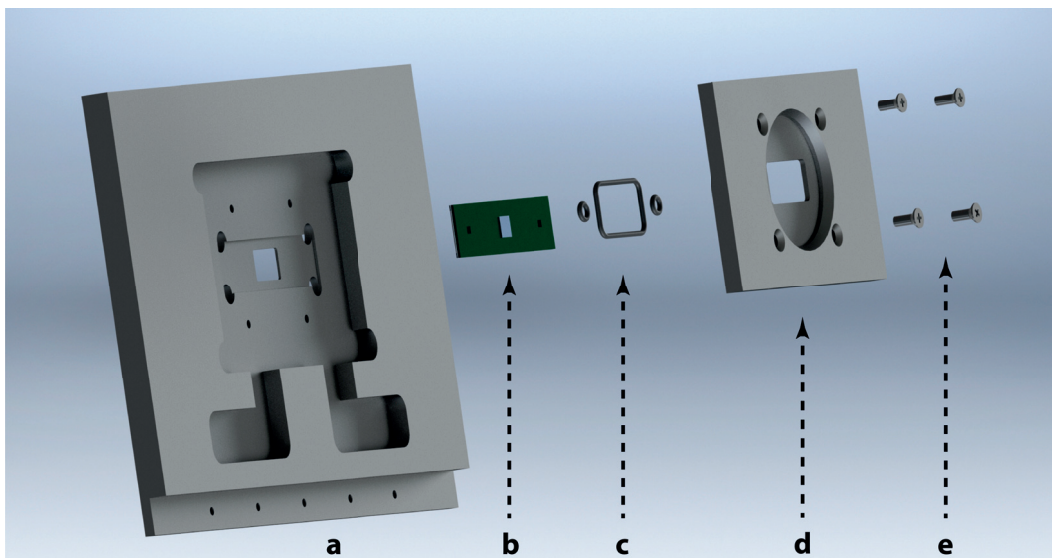
Figure 2.17 – Schematics of the parts involved in the aluminum mount placed between the AFM and the inverted optical microscope. The assembly consists of the bottom aluminum mount (a), microfluidic chip assembly (b), nitrile gaskets (c), top aluminum mount (d), and M2 screws (e).

The top part made of the polymeric material Verowhite (Stratasys) was 3D printed using the 3D printer Connex500 (Objet).

The aluminum mount was placed into a custom-built frame, between an inverted optical microscope (IX73, Olympus) and an AFM head (Dimension FastScan, Bruker) on a vibration isolation table. For optical microscopy we used a 60x air microscope objec-
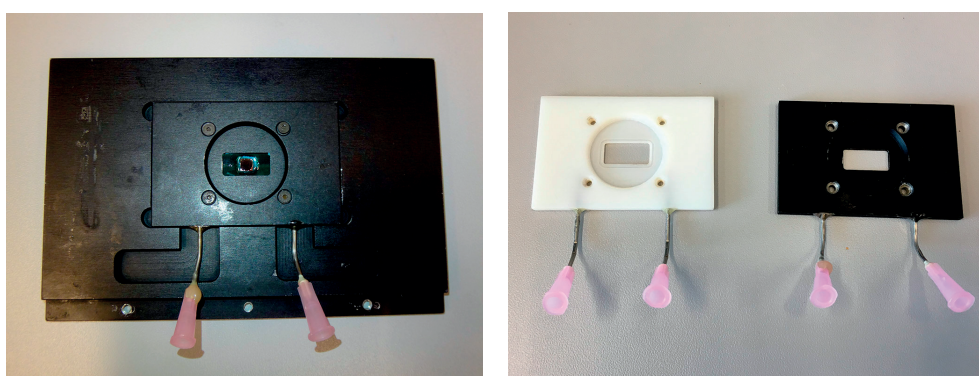
(a) Aluminum mount with an assembled microfluidic device as used throughout the experiments.

(b) Top part of the aluminum mount fabricated out of aluminum (right) and by 3D printing of a polymer (left).

Figure 2.18 – Aluminum mount as used throughout experiments together with top parts of different materials.

tive (LUCPLFLN, Olympus). The custom-built frame was designed and constructed by my colleague Pascal Odermatt [17]. Our laboratory setup is shown in figure 2.19 and the schematic of the experiment setup is depicted in figure 2.20. For the experiments discussed in chapter 3, we also used a second custom-built setup consisting of a Dimension Icon (Bruker) AFM head and an inverted optical microscope IX81 (Olympus) on top of a vibration isolation table (AVI-200-XL, Table Stable). The fluorescence excitation source originated from a mercury arc lamp (X-Cite 120, Excelitas Technologies) and the fluorescence images were recorded with an iXon3 (Andor) camera.
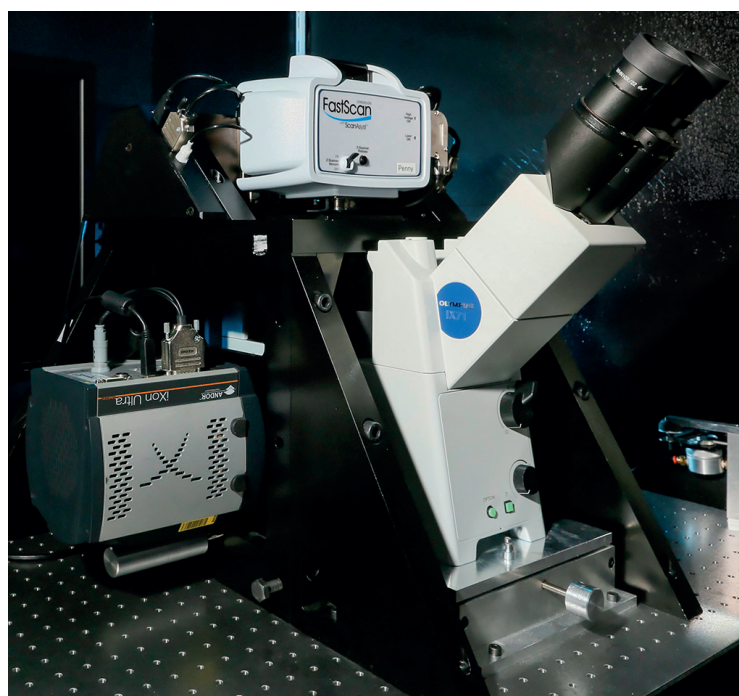
Figure 2.19 – Laboratory setup consisting of an AFM head on top of an inverted optical microscope on a custom built frame in our laboratory.

Due to the confined space between the two microscopes, the aluminum mount of the microfluidic chip assembly needed to be as thin as possible, providing fluidic connections as well as sufficient space to encompass the approached AFM head. We designed the aluminum mount to be compatible with Bruker's *Dimension Icon* head as well as the *Dimension FastScan* head.

In oder to use the AFM and fluorescence microscopy simultaneously, certain precautions needed to be taken. The wavelength of the AFM laser, responsible for the readout of the cantilever deflection, is situated in the emission spectrum of particular fluorophores, thus interfering with the fluorescent signal of the stained sample. To have an unaltered readout, the AFM laser needs to be switched off during the acquisition of the fluorescent image.
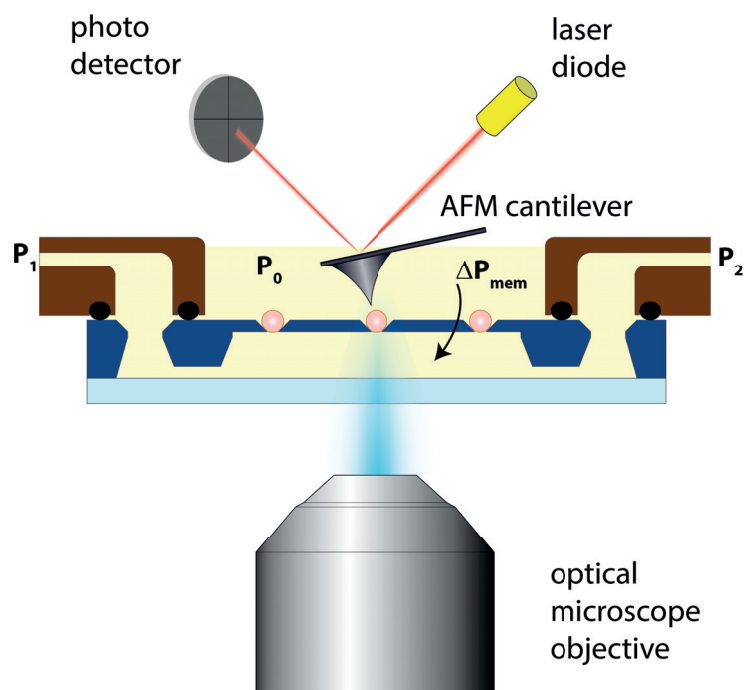
Figure 2.20 – Schematic of the laboratory experiment setup, placing the assembled microfluidic chip embedded in a custom holder between an AFM and inverted optical microscope.

For this purpose, my colleague Mélanie Hannebelle built a custom LabVIEW program to manually control the AFM laser, which was else not possible with the proprietary Bruker NanoScope software during AFM image acquisition. In order not to damage the AFM cantilever tip during the experiment, we changed the AFM mode to *ramp mode* prior to manually switching off the AFM laser and the consecutive fluorescence image acquisition. The thickness of the microfluidic chip assembly allows the use of 60x and 100x long working distance objectives for fluorescence microscopy.

2.5 Process flow discussion and conclusion

We first developed and optimized the process flow based on the SOI wafer technology. A major improvement was the use of the protective polymer layer ProTEK. Prior to using ProTEK, we relied on SiN to passivate the top side of the wafer containing the etched bacterial traps (figure 2.1d of the process flow). This was connected with a longer waiting period for the LPCVD of the SiN layer, usually a few days within our microfabrication facility CMi, whereas the ProTEK can easily be spin coated within 30 min.

Another major advantage of the ProTEK layer is its easy removal as compared to a SiN passivation layer. The ProTEK layer can simply be removed by either using a piranha solution or oxygen plasma, whereas we observed the best cleaning results by combining both techniques. A SiN passivation layer has to be removed by RIE and the used fluorocarbon gases will affect the protected silicon, despite the user selectable etch selectivity between SiN and silicon. Using wet chemistry based on HF would not affect the silicon, but the SiO_2 layer of the SOI wafer will be etched at a higher rate. The optimal wet etch to remove the SiN layer is hot phosphoric acid, requiring specific equipment, which we did not have at our local microfabrication facility at the time of development [67, 93].

The adhesion properties of the fully cured ProTEK layer presented a significant advantage, since the structures stayed attached to the polymer layer after wafer etch through with KOH. Therefore, we did not require dicing in order to obtain devices with precise dimensions for the microfluidic chips. Furthermore, we were able to improve the overall output from 14 to 126 devices per four-inch wafer with a > 99 % yield through the miniaturization of the microfluidic chips design.

Nevertheless, the SOI wafer technology presented a considerable drawback in the design of the bacterial traps. Due to the crystalline axes of silicon and the anisotropic etch properties of KOH, the shape of the bacterial trap is rectangular with a 54.74° inclined edges. The bottom opening of the bacterial trap is thus directly related to the width of the bacterial trap at the top, and the thickness of the silicon device layer of the SOI wafer. Furthermore, the design is very sensitive to a misalignment of the pattern to the (1 0 0) silicon crystalline axis [72]. A misalignment would result in a wider opening at the top and the bottom of the trap, which would have a direct influence on the bacterial immobilization. A wider opening at the bottom would allow bacteria to squeeze through when a higher pressure difference across the bacterial traps is applied, compromising the bacterial immobilization.

The silicon device layer of the SOI wafer translates directly into the depth of the fabricated bacterial trap. Our microfabrication facility CMi provided SOI wafers with a 340 nm thick device layer, which were suitable for the immobilization of the rod-shaped bacteria *E. coli* having a diameter around 900 nm. The initial cost of a SOI wafer is over a tenfold higher than the cost of a standard silicon wafer. To obtain a SOI wafer with a predefined silicon device thickness is possible, but is involved with higher costs. Companies providing SOI wafers such as Soitec, Shin-Etsu Handotai (SEH), and SUMCO, generally sell wafers only in large quantities and dimensions above 100 mm (four-inch). The wafers additionally need to be laser cut and re-worked, before we could use them in our microfabrication facility CMi that contains cleanroom equipment mainly for four-inch wafers.

(a) SEM image of bacterial traps obtained with the SOI process flow.

(b) SEM image of bacterial traps obtained with the t-SPL process flow.
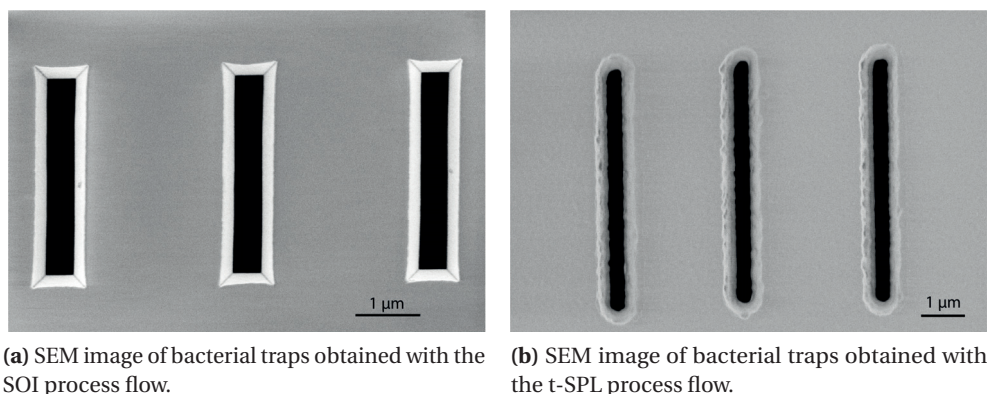
Figure 2.21 – Comparison of the SOI and t-SPL process flow results.

The process flow based on t-SPL is a proven alternative and the overall production costs are significantly reduced since no SOI wafers are involved, which are at least a tenfold more expensive than standard silicon wafers. Moreover, by using the t-SPL technology for the fabrication of bacterial traps, we define the depth of the bacterial trap by simply choosing the thickness of the LPCVD layer on top of a standard four-inch silicon wafer. This is an advantage of the t-SPL technology in comparison to the SOI wafer based technology, since it involves a significant cost reduction of the starting wafer. Furthermore, LPCVD can be done within our microfabrication facility with the wanted thickness, directly translating into the membrane thickness and bacterial trap depth, which reduces the overall production time compared to ordering and re-working SOI wafers in order to modify the bacterial traps dimensions.

Figure 2.21 compares bacterial traps at the end of the fabrication process using SOI wafer technology (figure 2.21a) and t-SPL technology (figure 2.21b). Bacterial traps obtained with t-SPL exhibit a shape tailored to the shape of rod-shaped bacteria. The design is not restricted by the crystalline silicon axis, as compared to the SOI wafer technology. Moreover, the slope of the pattern edge as well as the bottom opening of the bacterial traps can be chosen in order to optimally suit the bacterial shape.

Even though we were able to pattern directly on a four-inch wafer using t-SPL, the speed of patterning was significantly lower than by using e-beam lithography on SOI wafers. E-beam lithography is a proven technique and the patterning was rapid and straightforward. Patterning of 3D structures in PPA with t-SPL was challenging, but the benefit of *nanotailored* bacterial traps in SiO_2 strongly suggest that the t-SPL technique is advantageous for custom-made bacterial traps, in particular for bacteria such as the crescent-shaped bacterium *Caulobacter crescentus* discussed in section 3.3.2.

3 Applications of the bacterial traps to microbiology

3.1 Introduction

The *Escherichia coli* bacterium is the laboratory workhorse in microbiology, making it one of the most thoroughly studied microorganisms and model bacterium for rod-shaped bacteria [94]. In our laboratory as well, we used the *E. coli* bacterium in order to evaluate the immobilization properties of our bacterial traps and optimize various parameters regarding the bacterial traps dimensions and microfluidics. After successful proof of concept results with the model rod-shaped bacterium detailed in section 3.2, we applied our bacterial traps with different bacterial species. In particular, we focused on bacteria that were tried to be analyzed with the AFM in our laboratory, but the applied chemical modification of the substrate did not provide a sufficient immobilization.

Amongst bacterial species, the difference in bacterial envelope properties is large, directly affecting the immobilization on a substrate surface as discussed in section 1.3.1. The same substrate surface can act as a robust immobilization for one bacterial species and failing for another species. Moreover, within a species the bacterial envelope properties can change, in particular due to a mutation in the genome. We have evaluated our bacterial traps with different bacterial species and strains of *hard-to-immobilize* bacteria, discussing the results in section 3.3.

Furthermore, we demonstrate the technological potential with the AFM analysis of extremophiles, bacteria that grow and divide under low pH values, and by imaging bacterial poles of rod-shaped bacteria in section 3.4. Medium independent bacterial analysis combined with simultaneous AFM and fluorescence microscopy allowed to expand on previous studies of the antimicrobial peptide (AMP) CM15 on *E. coli* [13] by applying AMPs in physiological buffer medium and correlating AFM with fluorescence microscopy

results, discussed with more detail in section 3.5.

We conducted all experiments with bacteria in our laboratory using custom built experiment setups allowing simultaneous atomic force and fluorescence microscopy, as described in section 2.4.3. The presented results hereafter were taken using two different AFM heads, namely Bruker's *Dimension FastScan* and *Dimension Icon* head together with the proprietary software NanoScope in the versions 8.15 as well as 9.1.

3.2 AFM analysis of bacteria under physiological conditions

3.2.1 AFM imaging in liquid of physically immobilized bacteria

For the initial proof of concept experiments we used *E. coli* strains DH5α, BL21, and K-12 and we analyzed the bacteria in milli-Q water as well as in lysogeny broth (LB) medium. By applying a pressure difference as low as 20 mbar across the bacterial traps, we were able to guide the bacteria towards the traps and physically immobilize them in the bacterial traps. Figure 3.1 shows a 3D representation of a trapped *E. coli* bacterium in LB medium, where the height is represented in 3D overlaid with the phase signal taken in AFM tapping mode with a resolution of 1024 by 1024 pixels at 2 Hz. The experiment was done using a ScanAsyst-Fluid cantilever on the Dimension Icon AFM head.
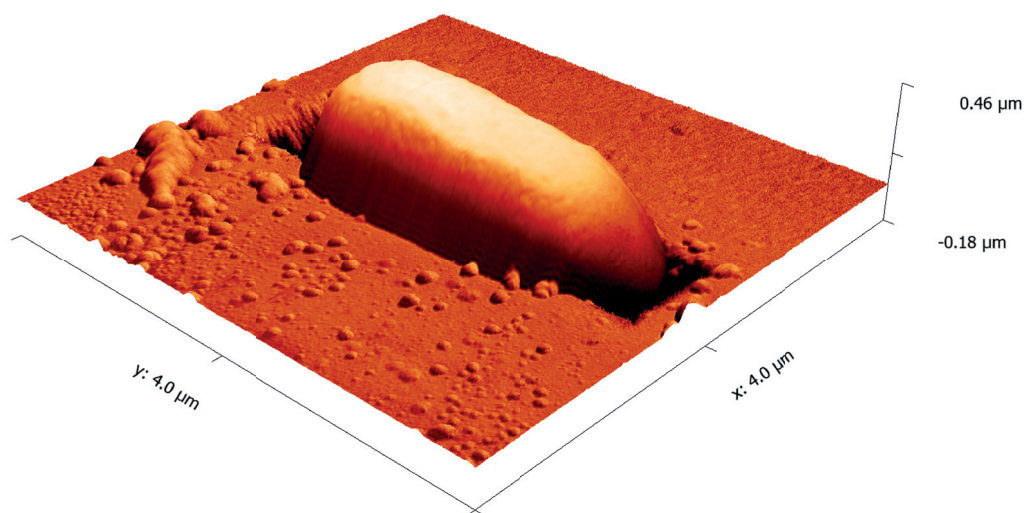
Figure 3.1 – Immobilized *E. coli* bacterium in lysogeny broth medium.

E. coli bacteria grow and divide in the LB physiological medium with a doubling time of 20 to 25 min at 37° C [95, 96]. The bacteria have a lower growth rate at room temperature, still the division has to be observable, if the viability of the bacteria is intact. Therefore, a strong

suggestion for an intact bacterial viability when a bacterium is physically immobilized in the fabricated trap, is to see the division in LB medium during an AFM analysis.

Figure 3.2 shows the division of an *E. coli* K-12 bacterium in LB at room temperature, where we focused on the division site. The bacterium was analyzed in QNM mode and the elastic modulus is depicted next to the height image for the selected time points. The applied force on the bacterium was 300 pN and the AFM images were taken at 2 Hz with a resolution of 256 by 256 pixels on a 1 μm scan size with the Dimension FastScan AFM head using a ScanAsyst-Fluid cantilever. The AFM height images show a range of 200 nm between the darkest (lowest) and brightest (highest) data point and the elastic modulus images depict points of higher value (higher stiffness) with brighter color.

We can observe the formation of the septum at the division site, marked by a red arrow in figure 3.2f, involving a local change in the elastic modulus of the bacterium. While the elastic modulus over the bacterium was several hundreds of kilopascal, consistent with reports in the literature [97, 98], we observed an increase of a factor of two for the elastic modulus over the septum. In the described experiment we found the elastic modulus of ~400 kPa on the bulk of the bacterial envelope and ~750 kPa over the septum, although the absolute values have to be interpreted with care, since the exact quantitative values depend on the correct AFM cantilever calibration (cantilever stiffness and tip radius) as well as the applied model for the calculation of the elastic modulus [99].

In figure 3.2o one daughter cell of the divided bacterium is out of the scope of the imaged area. During our experiment we have observed that imaging a bacterium in the pole region resulted in a displacement of the bacterium inside the traps along the longitudinal axis of the trap (vertically for all images in figure 3.2). Therefore, after physical separation in the division cycle of the bacterium, the applied forced exerted by the AFM cantilever on the bacterial pole were displacing the bacterium outwards of the imaged area.

3.2.2   Sample preparation protocol

The preparation of the bacterial suspension for AFM imaging is trivial as compared to the protocols explained in detail in section 1.3. For every experiment, we grew bacteria overnight from a single colony in LB growth medium at 37° C. Thereafter we regrew 10 μl in fresh LB for 3 h. Prior to an experiment, we diluted the regrown solution 10'000 times in filtered LB, whereas the LB was filtered with a 200 nm millipore filter in order to remove larger particles.

We did not apply any pelleting, washing, or vortexing steps, commonly found in sample

(a) 0s; Height   **(b)** 0s; Modulus   **(c)** +4min 22s; Height   **(d)** +4min 22s; Modulus

(e) +7min 34s; Height   **(f)** +7min 34s; Modulus   **(g)** +12min 3s; Height   **(h)** +12min 3s; Modulus

(i) +18min 35s; Height   **(j)** +18min 35s; Modulus   **(k)** +22min 57s; Height   **(l)** +22min 57s; Modulus

(m) +27min 19s; Height   **(n)** +27min 19s; Modulus   **(o)** +32min 45s; Height   **(p)** +32min 45s; Modulus
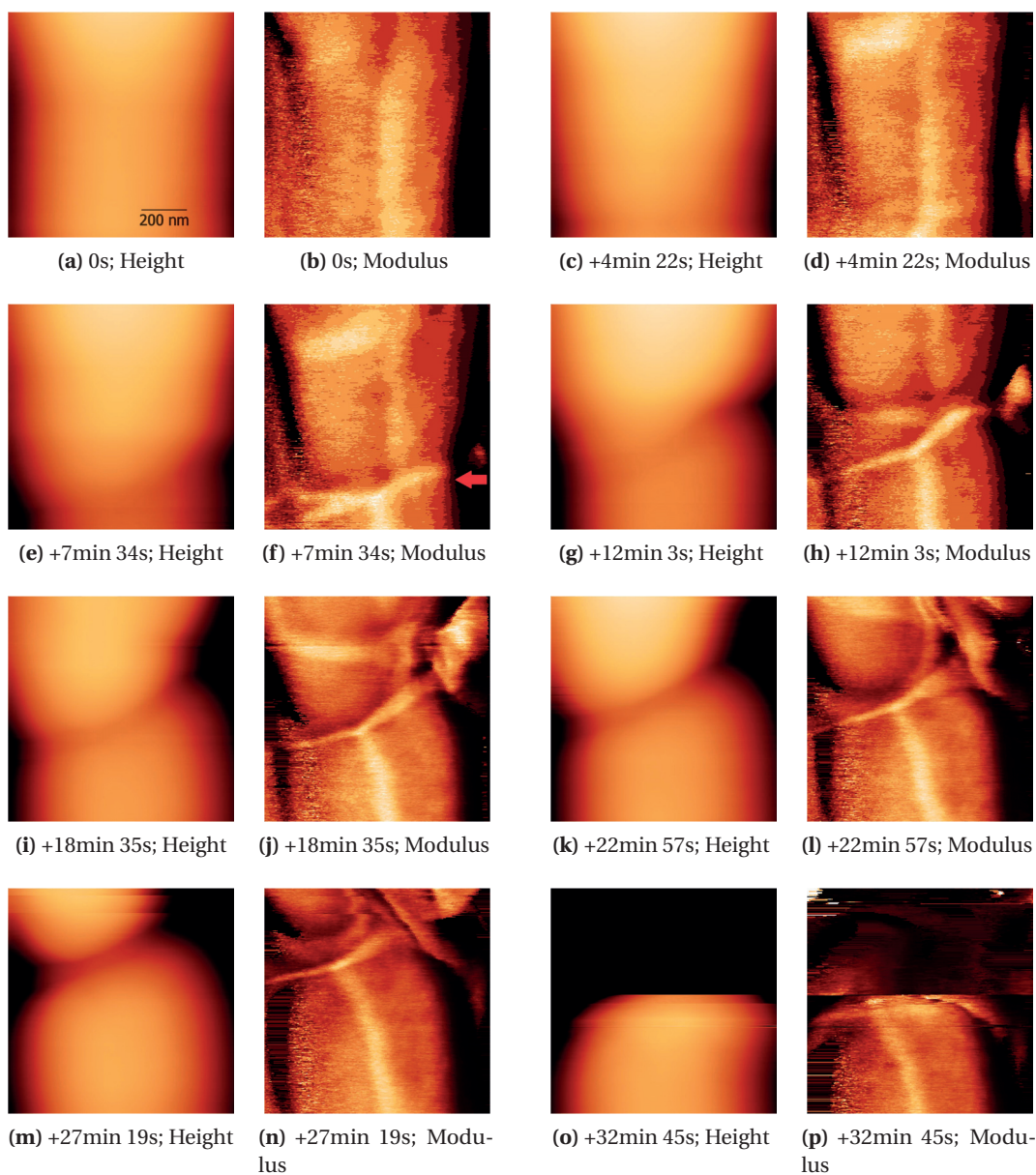
Figure 3.2 – AFM height and modulus images of the division of an *E. coli* bacterium in LB. The AFM height images show a range of 200 nm between the darkest (lowest) and brightest (highest) data point and the elastic modulus images depict points of higher value (higher elastic modulus) with brighter color. The scan speed was 2 Hz with a resolution of 256 by 256 pixels on a 1 μm scan size with an force set point of 300 pN.

preparation protocols. This is a major advantage compared to standard bacterial immobilization protocols [45], since the bacteria can be analyzed by AFM immediately after the incubation.

Prior to every experiment, we flushed the microfluidic channel underneath the bacterial traps with 200 nm filtered LB in order to check the microfluidic chip assembly for leakage. Moreover, we could remove any residual air bubbles underneath the bacterial membrane prior to the start of an experiment, which would otherwise perturb the fluorescence microscopy. The sample preparation time, measured from taking the culture out of the incubator until engaging with the AFM head, takes roughly 5 min to 15 min, as experienced on a routinely basis.

3.2.3 Trapping and releasing

Bacteria can be trapped and released during the AFM analysis, as shown in figure 3.3. By simply inverting the pressure difference across the bacterial traps, bacteria are trapped, expulsed, and re-trapped. During the trapping and releasing process, we acquired AFM images in tapping mode at 10 lines s^{-1} with a resolution of 1024 by 256 pixels on the Dimension FastScan AFM head using a FastScan-DX cantilever. The experiment was done in LB medium with *E. coli* DH5α bacteria.
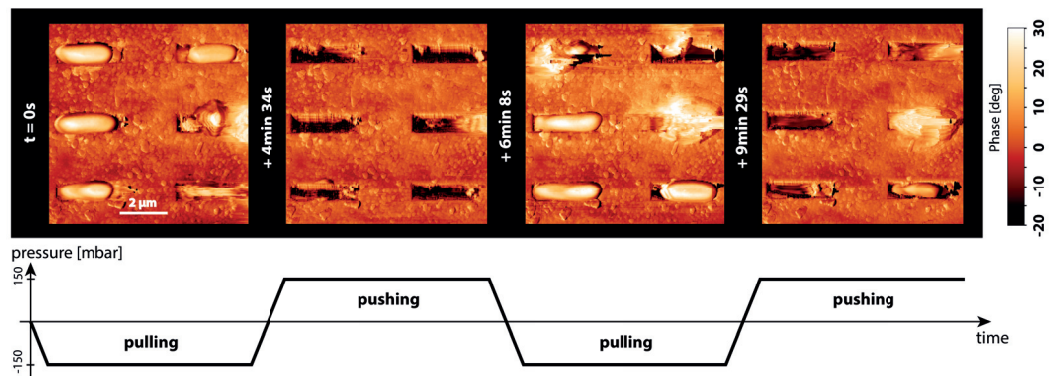
Figure 3.3 – Trapping and releasing of *E. coli* bacteria on demand during AFM imaging in LB.

For the experiment in figure 3.3, we started by imaging the bacterial traps with the AFM in LB that did not contain bacteria. While scanning, we added 200 μl of the bacterial suspension that was 10'000 diluted compared to the overnight culture. Thereafter we applied a pressure between 150 mbar and -150 mbar across the bacterial traps in order to trap and release the bacteria. The trapping and releasing process was observable within a frame, when the pressure was switched during AFM imaging. The image sequence in figure 3.3 shows frames where a negative or positive pressure was maintained during the frame data acquisition time.

3.2.4   Bacterial trapping reliability

One main drawback that we've encountered during our experiments was that particles larger or in the size of the targeted bacteria are trapped as well, as shown by the two rightmost sub-figures in figure 3.3, and thus perturbing the experiment. We can push away any undesirable particles from the traps by simply inverting the pressure difference and restart the immobilization of bacteria. Possible contaminants at the surface and in proximity of the bacterial traps can also be eliminated by pipetting the fluid around the traps on the top-side of the microfluidic chip.

Furthermore, applying higher scanning forces with the AFM tip, anything not fully immobilized in the traps is swept away. Particles smaller than the bottom opening of the bacterial traps will simply pass through the bottom opening. Eventual clogging of the traps may be solved by selective delivery of bacteria towards the traps or by using a fluidic filter to distinguish between bacteria and particles of certain size, as described by previous studies [100, 101]. However, bacteria can also squeeze through the traps, if the pressure difference across the membrane is at least an order of magnitude higher than for the described experiments.

3.3   Bacterial species independent AFM analysis

The AFM experiments in section 3.2 were all conducted on gram-negative *E. coli* bacteria. Nevertheless, our developed physical immobilization method is suitable for AFM analysis independent of the bacterial species. Hereafter we present experiments with different gram-negative and -positive bacteria immobilized by our developed bacterial traps.

3.3.1   Bacillus subtilis

Figure 3.4 shows the bacterial envelope of the gram-negative *E. coli* bacterium versus the gram-positive *Bacillus subtilis* bacterium. While the used *E. coli* bacteria were non-motile, the *B. subtilis* PY79 strain [102] exhibited motility. We found that the width of the *B. subtilis* bacterium was roughly in the same range as the used *E. coli* bacteria and therefore the fabricated bacterial traps were ideal for the physical immobilization.

The intact envelope of the *E. coli* bacterium shows a smooth surface in figure 3.4 (left), while the surface of the *B. subtilis* bacterium elucidates the structure of the peptidoglycan architecture as shown in figure 3.4 (right). The architectural model of the peptidoglycan of *B. subtilis* was proposed to be a coiled-coil structure [37]. The bacteria in figure 3.4
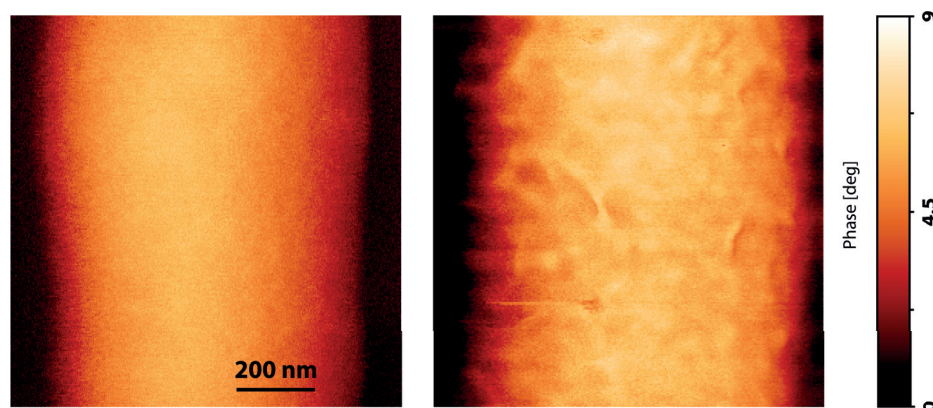
Figure 3.4 – Envelope of a gram-negative *E. coli* (left) and a gram-positive *B. subtilis* bacterium (right).

were imaged in LB by AFM tapping mode with a scan size of 1 μm and scan speed of 10 Hz with a resolution of 1024 by 256 pixels (left) and 4 Hz with a resolution of 256 by 256 pixels (right) on a Dimension Icon AFM head using a ScanAsyst-Fluid cantilever.

3.3.2 Caulobacter crescentus

The morphological diversity of bacteria is vast and the shapes range from round, rod-shaped, oval, spiral, and curved bacteria [103, 104]. An example of a bacterium with a curved morphological shape is the *Caulobacter crescentus* bacterium. *C. crescentus* is used as a model bacterium to study the generation and maintenance of the crescent shape during growth and division [105]. Recent super-resolution optical microscopy findings highlight the crescent morphology of *C. crescentus* and identify relations between cytoskeletal elements and cell shape [106, 107].

AFM inherently allows the study of nanomechanical properties and analysis at the division site of the bacterium could provide detailed insight of the division process at the septum of the bacterium. Although pioneering results of AFM imaging in aqueous medium of *C. crescentus* were accomplished, the immobilization of the bacterium appeared to be very challenging, impacting the interpretation of the results [108].

Here, we showcase the immobilization of the *C. crescentus* bacterium with our developed technique in physiological buffer medium peptone yeast extract (PYE). The experiments were done together with my collaborators Aster Vanhecke and Ambroise Lambert on the AFM setup in our laboratory with the Bruker Dimension FastScan head. Figure 3.5 depicts two immobilized *C. crescentus* bacteria inside a trap, where the AFM height image is represented in 3D in order to elucidate the crescent morphological shape of the bacteria.

The image was taken in PYE medium in QNM mode at 2 Hz with a resolution of 256 by 256 pixels and a force set-point of 1 nN on a Dimension FastScan AFM head using an AC40 cantilever.
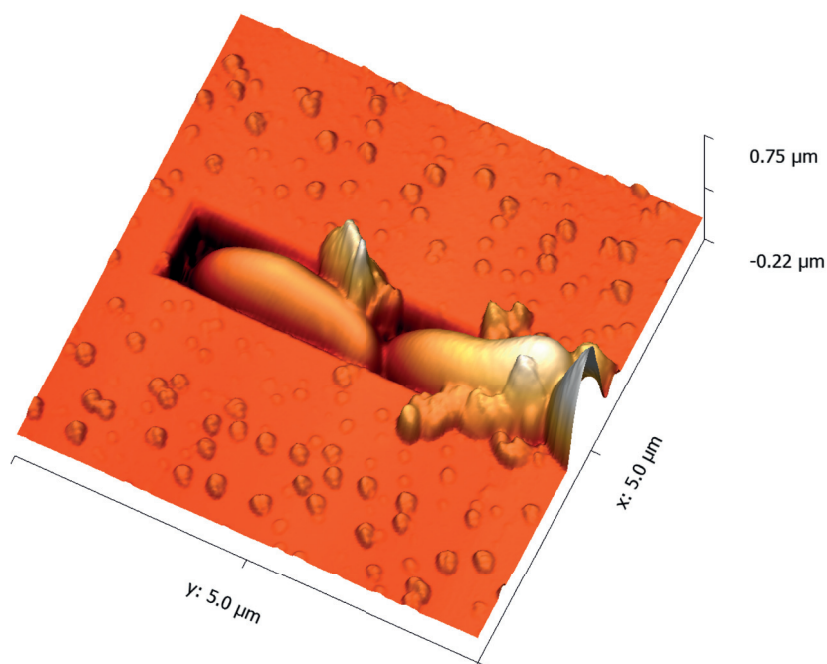
Figure 3.5 – *C. crescentus* analyzed in physiological buffer medium. The AFM height is represented in 3D showing the crescent shape of the bacterium. The image was taken in QNM mode at 2 Hz with a resolution of 256 by 256 pixels and a force set-point of 1 nN.

Although the AFM imaging in PYE medium was possible, we observed contamination by smaller particles at the edges and around the traps. This might be due to the unfiltered PYE medium used during this experiment. The aqueous medium M2G would be more suitable as an alternative physiological medium providing less contamination during the experiment.

Furthermore, the rectangular bacterial trap size was suboptimal for the crescent shape of the *C. crescentus* bacterium. The ideal solution would be the fabrication method described in section 2.3. The t-SPL fabrication method allows a shape-independent fabrication of bacterial traps. Thus, crescent bacterial traps can be fabricated, nanotailored for the immobilization of the curved morphological shape of *C. crescentus*.

3.3.3 Streptococcus pneumoniae

The *Streptococcus pneumoniae* bacterium is an oval-shaped, pathogenic bacterium, which has developed a broad-spectrum resistance against common antibiotics such as β-lactam antibiotics [109]. For the development of new antimicrobial agents, the division site of bacteria is often targeted. At the division site, new material such as peptidoglycan is synthesized and the inhibition of material synthesis or disruption of partially synthesized bacterial envelope material can be a point of vulnerability [110].

The division of *S. pneumoniae* occurs differently than in rod-shaped bacteria such as *E. coli* or *B. subtilis*. Experiments indicate that the Min-protein system and nucleoid occlusion system, which is governing the division in *E. coli* or *B. subtilis* [111, 112], is not present in *S. pneumoniae* bacteria [113]. Recent discoveries suggest that the protein MapZ is involved in the division plane selection of *S. pneumoniae* [114], which controls the binding of the protein FtsZ that is responsible for the initiation of the bacterial division assembly in most bacteria [115].

Therefore, the investigation of the division site of the ovococcal *S. pneumoniae* is of particular interest. Immobilization of *S. pneumoniae* for AFM analysis can be done by our developed bacterial traps and the results of successful analysis of a dividing *S. pneumoniae* bacterium is depicted in figure 3.6, where the red arrow indicated the division site. The AFM height is represented in 3D and overlaid by the stiffness map, where a darker area represents a data-point of lower stiffness.
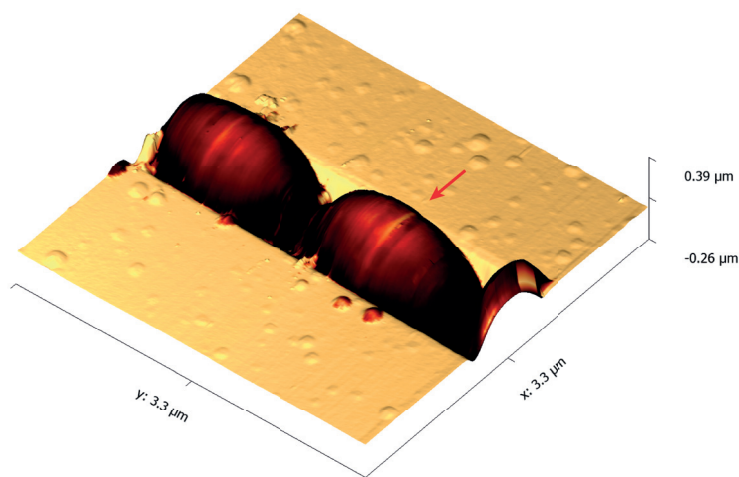
Figure 3.6 – *S. pneumoniae* analyzed in physiological buffer medium. The AFM height is represented in 3D and the elastic properties are overlaid. A brighter value represents a data-point with higher stiffness. The image was taken in QNM mode at 0.4 Hz with a resolution of 512 by 256 pixels and a force set-point of 2 nN.

The experiment was conducted together with my colleagues Renske van Raaphorst and Alexander Eskandarian. For the experiment we used the AFM setup in our laboratory with the Bruker Dimension Icon AFM head. The *S. pneumoniae* bacterium depicted in figure 3.6 was imaged in the physiological aqueous medium C+Y in QNM mode at 0.4 Hz with a resolution of 512 by 256 pixels and a force set-point of 2 nN. We used a non-capsular wild-type *S. pneumoniae* bacterium that is virtually non-pathogenic, in oder to be compatible for the analysis in our laboratory.

3.4   Imaging of extremophiles at low pH

Our physical immobilization method allows AFM analysis of bacteria independent of the aqueous medium. The used materials for the fabrication of the bacterial traps are inert, unless specific chemical compounds are used [67], and therefore we are able to study extremophiles that grow at low pH values and in the presence of acids. The bacterium *Acidiphilium cryptum* is a rod-shaped, gram-negative bacterium having physiological conditions at a pH=3 in the presence of sulfuric acid and is sensitive to many organic compounds [116]. We followed the cultivation protocol according to the *DSMZ - Deutsche Sammlung von Mikroorganismen und Zellkulturen* (DSM No.: 9467; medium 670 with strain-specific modifications) [117].

In order to be compatible with the physiological conditions of the studied bacterium, we used the 3D printed top part that is made out of a polymeric material and showing excellent resistance to sulfuric acid, as described in section 2.4.3.

The 3D AFM height image of an *A. cryptum* bacterium is depicted in figure 3.7. The bacterium was imaged in physiological buffer medium with a pH=3.06 in QNM mode. The applied force on the bacterium was 3 nN and the bacterium was imaged with a speed of 9.8 Hz and a resolution of 512 by 512 pixels with a scan range of 1.5 μm. We can observe the smooth surface of the bacterial envelope, characteristic to gram-negative bacteria discussed in the aforementioned results.

In the microfluidic channel underneath the bacterial traps we used milli-Q water, since the physiological buffer medium containing sulfuric acid could have a reaction with the double sided adhesive tape that is in direct contact with the aqueous medium.

For the study of *A. cryptum* we used a custom AFM cantilever holder for Bruker's *Dimension Icon* AFM head, which did not contain any metallic structures that are in contact with the aqueous medium. Therefore, the cantilever was attached to the holder by applying wax between the cantilever body and the holder.
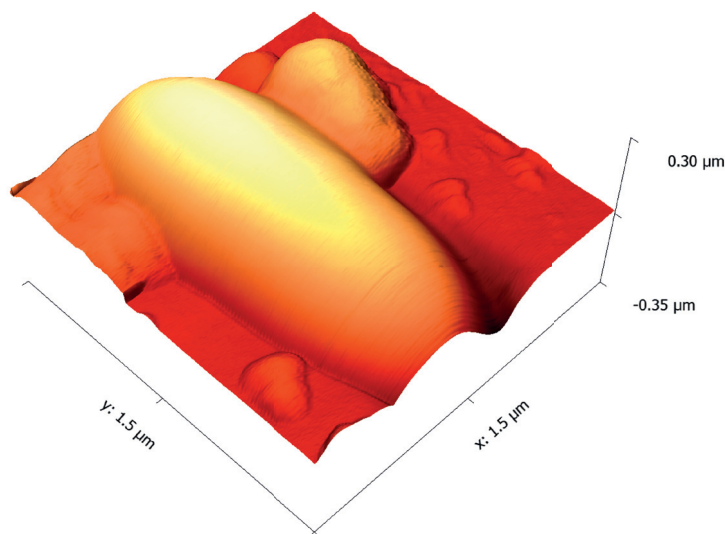
Figure 3.7 – Immobilized *A. cryptum* bacterium in physiological buffer medium with a pH=3 containing sulfuric acid. The AFM height is represented in 3D. The bacterium was imaged in QNM mode with 9.8 Hz with a resolution of 512 by 512 pixels and the applied force was 3 nN.

3.4.1 Trapping by the poles

The *A. cryptum* bacterium is known to be motile, where the motility is given by polar flagella [116]. In order to study the pole of a bacterium, we used the bacterial traps fabricated with the t-SPL manufacturing method discussed in section 2.3. This allowed us to have round traps, suitable for the physical immobilization of rod-shaped bacteria by the poles, where the longitudinal axis of the rod is perpendicular to the membrane containing the bacterial traps. Figure 3.8 shows an overview image of *A. cryptum* bacteria trapped by the poles and a close-up image of a single bacterium.

As compared to the experiments conducted on the longitudinally immobilized bacterium in figure 3.7, the material surrounding the bacteria trapped by the poles is SiO_2 instead of silicon, however all experimental conditions are the the same. The images in figure 3.8 were taken in QNM with a force set point of 3 nN (left) and 10 nN (right) and a scan rate of 1 Hz (left) and 2 Hz (right) with a resolution of 512 by 512 pixels.

We can observe a perturbation in the image when the AFM cantilever tip is scanning the apex of the bacterial poles. We suggest that this perturbation is due to the freely moving pilus (or pili) on the bacterial poles. The perturbation occurs in the direction of the cantilever tip movement and is visible in figure 3.8 (left) towards the left since the cantilever moved from the right side of the image to the left in the *retrace* action. Analog for figure 3.8 (right), the *trace* movement of the cantilever tip from the left to the right side
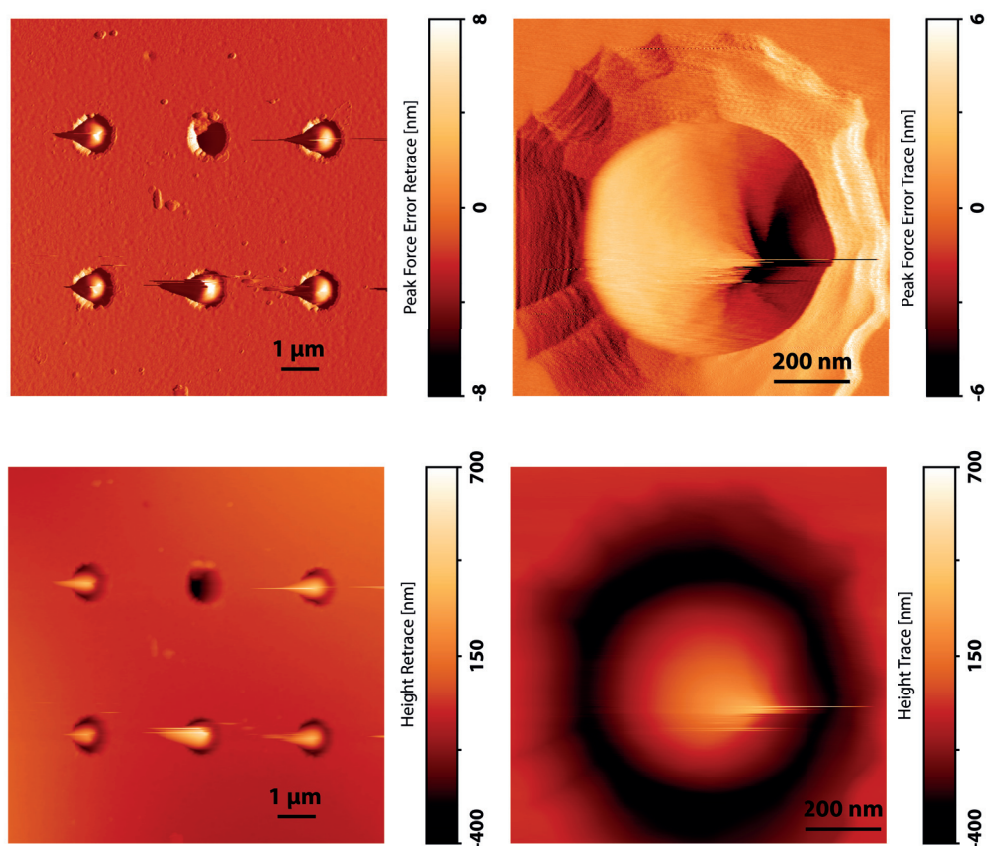
Figure 3.8 – *A. cryptum* bacteria immobilized by the poles in physiological buffer medium at pH=3. The images were taken in QNM with a force set point of 3 nN (left) and 10 nN (right) and a scan rate of 1 Hz (left) and 2 Hz (right) with a resolution of 512 by 512 pixels (left and right). The peak force error signal (top row) in retrace (left) and trace (right) is shown as well as the corresponding AFM height image (bottom row).

of the image, the perturbation on the pole is visible only after the apex towards the right side of the image. We observed this perturbation on the apex regardless of the AFM scan angle, indicating strongly a physically present structure such as one or multiple pili at the apex of the poles.

In order to confirm the finding, we dried the trapped bacteria in air, by first rinsing the physiological buffer three times with milli-Q water. The drying allowed the attachment of the structure on the pole apex to the surrounding substrate. The images in air indicate the presence of at least one pilus per bacterium, as indicated by the red arrows in figure 3.9. The images were taken in QNM with a force set point of 10 nN and a scan rate of 1 Hz with a resolution of 512 by 512 pixels.
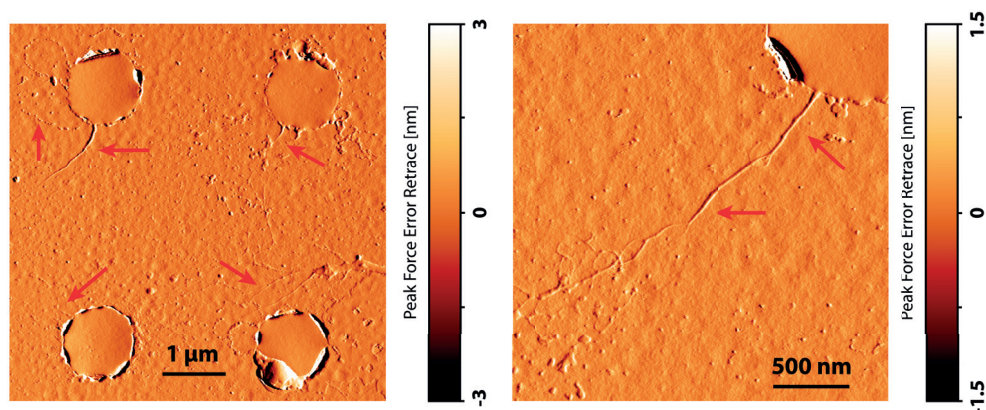
Figure 3.9 – *A. cryptum* bacteria immobilized by the poles and dried overnight. The images are taken in air to confirm the presence of pili on the poles of the bacteria. Both images were taken in QNM with a force set point of 10 nN and a scan rate of 1 Hz with a resolution of 512 by 512 pixels.

3.5 Killing dynamics of antimicrobial peptides

AFM imaging of bacteria has become a powerful tool for studying the interaction of antimicrobial agents with bacteria [118, 119]. Pioneering results have shown that the β-lactam antibiotic cefodizime caused morphological changes of the *E. coli* envelope and can lead to lysis, depending on the concentration [120]. *Staphylococcus aureus* bacteria exposed to the peptidoglycan cleaving enzyme lysostaphin show as well a roughening of the bacterial surface and differences in the nanomechanical properties of the bacterial envelope [121].

The AMP CM15 is known to exhibit a pore forming mechanism on the bacterial envelope [122], which can lead to bacterial lysis [123]. Observations by Fantner *et al.* using CM15 on *E. coli* elucidated the dynamics of bacterial death on the nanoscale [13]. In this study described hereafter, we investigate the action of CM15 on *E. coli* under physiological condition, and by using simultaneous AFM and fluorescence microscopy, allowing the monitoring of the bacterial viability through live/dead fluorescence stains.

3.5.1 Antimicrobial peptides as potent antibiotics

An AMP is an effective defensive agent of animals and plants against a wide range of microorganisms [124, 125]. AMPs are a class of antibiotics exhibiting a broad-spectrum capability against bacteria and are bactericidal [126]. However, AMPs are as well used by many pathogenic bacteria and are an essential element of their virulence [127].

The resistance of bacteria to antibiotics, as a result of chromosomal mutations or exchange

of genetic material e.g. through plasmids [128], has lead to a crisis due to the excessive clinical use of antibiotics during the last decades [129]. Although the bacterial antibiotic resistance is a natural evolutionary phenomenon [130], the severity of the antibiotic crisis is being tackled on an international level through private and public collaborations [131].

AMPs remained a potent weapon against bacteria through the evolution, since they have the possibility to not only inhibit metabolic pathways inside a living microorganism, but create pores in the microbial envelope in order to kill the microorganism [132]. The AMP insertion into the bacterial envelope is modeled by different pore formation mechanisms [133, 134] and the pore formation leading to lysis is bactericidal even for multidrug-resistant bacteria [127, 135].

3.5.2 Medium dependent action of antimicrobial peptides

Analog to the experiments done by Fantner *et al.* [13], we exposed *E. coli* bacteria to the antimicrobial peptide CM15 at minimum inhibitory concentration (MIC) in milli-Q water. The result is depicted in figure 3.10, where the bacterial envelope changes from a smooth (left, before CM15 injection) to a rough (right, after CM15 injection) surface morphology. This roughening happened imminently after the injection of the AMP. The images were taken in tapping mode at 2 Hz with a resolution of 256 by 256 pixel with a scan size of 1 μm.
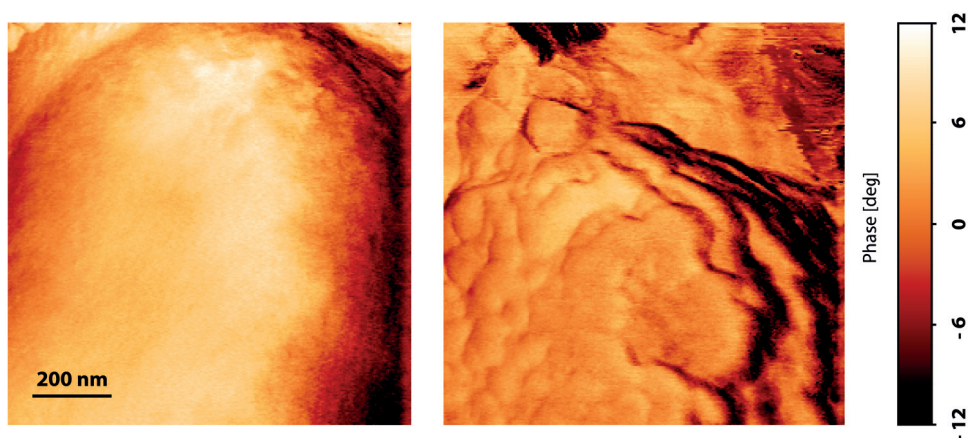
Figure 3.10 – Killing of an *E. coli* bacterium with CM15 in milli-Q water at MIC. The time between the two images was 9 min.

When the same experiment is performed in the LB physiological buffer medium, the roughening of the bacterial envelope showed different dynamics as compared to milli-Q water. After we injected CM15 at MIC, only a minimal increase in surface roughness

was observed. The bacterial envelope acquired its initial smooth surface within minutes after the AMP injection. After the injection of five times the MIC the bacterium showed pronounced surface features that persisted until the end of the experiment. Figure 3.11 depicts the experimental results. The bacterium was analyzed in AFM tapping mode at 2 Hz with a resolution of 256 by 256 pixel on a scan size of 1 μm. The surface roughness is indicated by R_a and is the arithmetical mean deviation of all points on the height map of the bacterial surface. The R_a values were taken on the surface of the bacterium in the corresponding AFM height image, where the AFM phase image is shown with a magnified area in figure 3.11b for a better contrast.

The shown observations could indicate the presence of a bacterial envelope repair mechanism that is present and active under physiological conditions. It has been shown that osmoprotectants present in LB growth medium give the bacterium protection against the killing mediated by CM15 [136]. Our obtained results support the CM15 cytotoxicity against *E. coli* and the reported findings regarding the influence of osmoprotectants on bacterial killing.
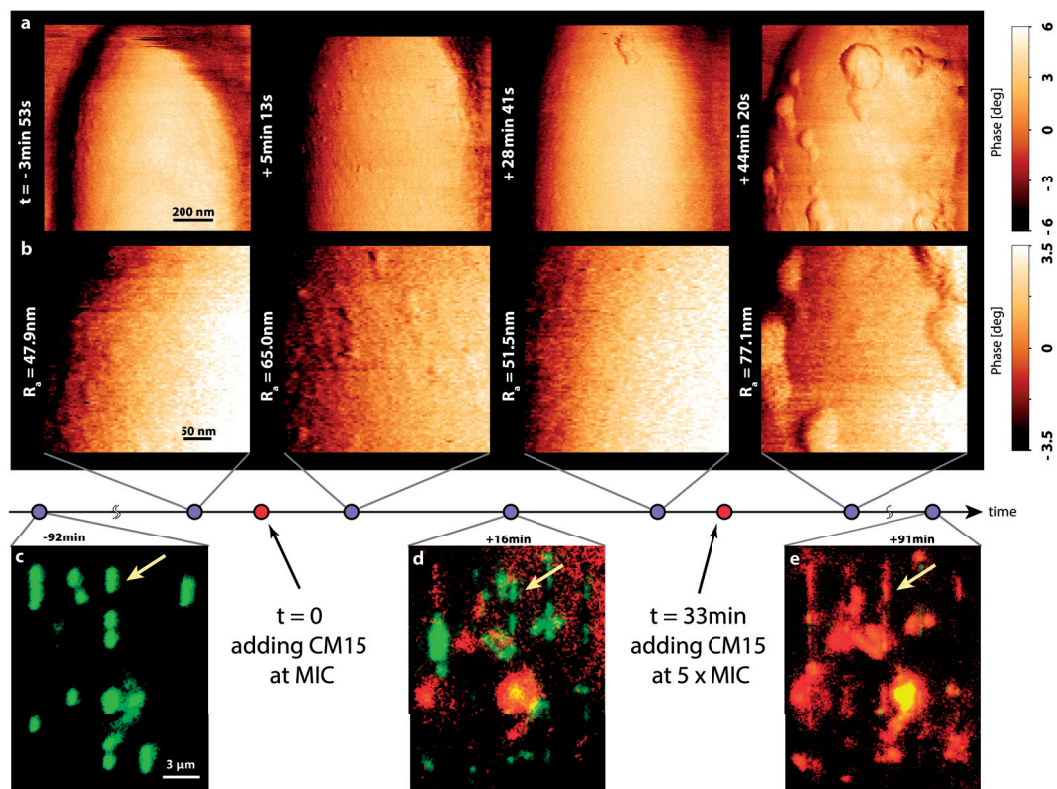
Figure 3.11 – Killing mechanics of the antimicrobial peptide CM15 on *E. coli* bacteria using correlative AFM and fluorescent microscopy.

3.5.3 Correlated fluorescence and atomic force microscopy

With the developed microfluidic chip, we have the possibility to conduct atomic force and fluorescence microscopy simultaneously. By using bacterial viability stains, we were thus able to monitor the alive and dead state of bacteria correlative to the AFM analysis.

For our experiments we used the LIVE/DEAD BacLight bacterial viability kit (Thermo Fisher Scientific) consisting of the nucleic acid stains SYTO 9 and propidium iodide (PI). A bacterium in the alive state is visible in the green fluorescence channel due to the SYTO 9 stain, whereas a dead bacterium appears in the red fluorescence channel due to the PI stain.

As we can see in the aforementioned experiment, at the beginning of the experiment all bacteria are visible only in the green fluorescence channel shown in figure 3.11c. At the end of the experiment, after the bacteria have been killed by the AMP, all bacteria are visible in the red fluorescence channel, as depicted in figure 3.11e. This correlative information confirms additionally our experimental results and the cytotoxicity of CM15.

The interesting additional information that we can obtain through the correlative fluorescence microscopy is shown in figure 3.11d. After the killing attempt with CM15 at MIC and the initial, minimal increase of surface roughness, the analyzed *E. coli* bacterium is still visible in the green fluorescence channel, suggesting its alive state. At this time point, the PI fluorophore did not penetrate through the bacterial membrane, which suggests an uncompromised bacterial envelope [137]. Although care must be exerted when the SYTO 9 and particularly the PI stains are used [138, 139], the data strongly suggests that all bacteria are dead after the injection of CM15 at five times the MIC and the appearance of the pronounced surface features on the bacterial envelope as shown in figure 3.11e.

3.6 Conclusion on AFM imaging of bacteria in liquid

Our microfluidic chip assembly compounds are fabricated from chemically inert materials. In contrast, microfluidic devices made from PDMS may influence cell behavior, since uncrosslinked oligomers can interact with microorganisms, and hydrophobic molecules from the medium can be absorbed into the PDMS, which could lead to experimental artifacts [63]. Moreover, PDMS reacts with sulfuric acid [140], and thus extremophiles such as the bacterium *A. cryptum* that grows under the presence of sulfuric acid, are only possible to be analyzed in chemically inert compounds, such as our developed bacterial traps.

As discussed in this chapter, our proposed physical immobilization method is independent of the envelope composition of bacteria, the surrounding aqueous medium, and the bacterial sample preparation. We were thus able to demonstrate the immobilization and AFM analysis of different bacterial species such as gram-positive and -negative, motile and non-motile, and rod-shaped, ovococcal, and crescent bacteria. AFM analysis can be conducted immediately after placing a drop of the bacterial suspension on top of the assembled microfluidic chip. This allows a versatile application across a multitude of bacterial species and liquid media.

The developed round bacterial traps used for the bacterial immobilization described in section 3.4.1, can as well be used for coccoid bacteria. Compared to physical immobilization techniques with millipore filters allowing serendipitous immobilization of bacteria [59], our approach allows the precise immobilization of bacteria in the area of investigation and a custom-tailored design of the bacterial trap to the needed size of the bacterium. Nevertheless, we demonstrated the AFM analysis of bacterial poles of rod-shaped bacteria. This is of particular interest for the analysis of bacterial growth, since specific bacterial species such as the *Mycobacterium smegmatis* synthesize new envelope material at the poles [141] as compared to bacterial species with different growth mechanism [103]. Further analysis of the poles could therefore provide more insight on the dynamics of polar material synthesis using our bacterial traps.

4 Nanomechanical measurements using atomic force microscopy

4.1 Introduction

Thus far, we described the use of the AFM on living samples and presented our solution how to overcome the difficulties. The AFM is inherently suitable for the analysis of material properties of samples regardless of their nature e.g. living or solid matter, soft or hard [99]. With the AFM, we are able to investigate microscopic mechanical properties of samples, which can differ by orders of magnitude compared to their macroscopic properties as shown in this chapter.

Using the knowledge obtained during AFM measurements conducted in our laboratory, we present here nanomechanical measurements on samples fabricated by colleagues and collaborators, where the intrinsic properties of the samples were a priori unknown. In section 4.2 we discuss the fracture point of a suspended silicon nanowire (SiNW), where we applied a novel approach in order to obtain the results. We focus in section 4.3 on various types of hydrogels and the determination of their elastic modulus highlighting the difference between microscopic and macroscopic material properties.

4.2 Mechanical characterization of silicon nanowires

The fabrication of nanowires can be achieved by either a bottom-up or a top-down approach. The characteristics of the bottom-up approach is the highly anisotropic growth of nanocrystals [142, 143]. The main growth techniques include the vapor-liquid-solid technique using gold-silicon droplets as catalysts to grown silicon nanowires [144], laser assisted growth [145], and thermal evaporation [146].

SiNWs can be used as electrical components, since their piezoresistance effect differs strongly from bulk silicon [147], and as resonators for mass detection in the subzeptogram range [148]. Furthermore, nanowires have been used as strain sensors [149] and SiNW integrated in a field effect transistors (FET) have been used as biosensors for highly sensitive antigen detection in the femtomolar range [150].

Nevertheless, the integration of nanowires into microelectromechanical system (MEMS) is challenging with the bottom-up nanowire fabrication approach, due to the inadequate control over the orientation and number of nanowires [151]. The top-down approach for nanowire fabrication is more suitable compared to the bottom-up approach for bulk fabrication and integration into MEMS on the wafer scale [152], by maintaining the compatibility for complementary metal oxide semiconductor (CMOS) fabrication [153].

The microfabrication process named single-crystal reactive ething and metallization (SCREAM), exhibits excellent integration properties of SiNW into MEMS devices [154]. The SiNW arrays obtained with this process were fabricated by my collaborator Zuhal Tasdemir in our microfabrication facility CMi [155, 156]. The determination and analysis of the SiNW mechanical properties was done together by Zuhal Tasdemir and myself.

Our goal was to determine the point of fracture of a SiNW. For this reason, a nanomechanical three-point bending test was performed with an AFM, where the cantilever tip was placed on the middle of the SiNW. First, the AFM was engaged onto the triangularly shaped anchor of a SiNW. Figures 4.1 and 4.2 depict SEM images of the SiNWs, confined by the triangular anchors.
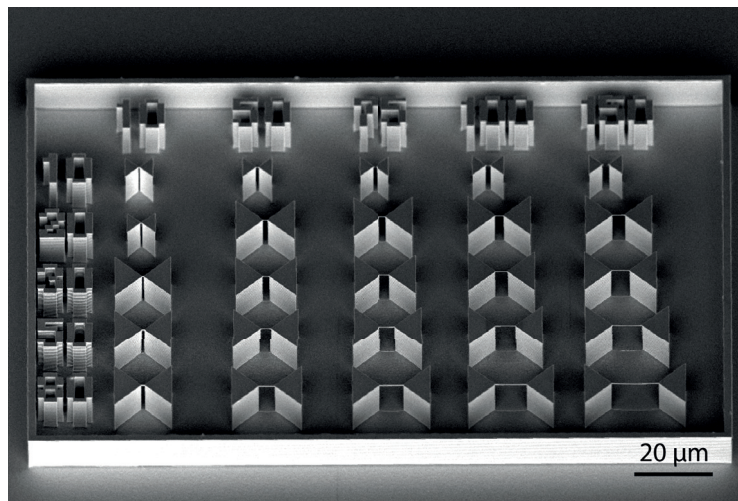
Figure 4.1 – SEM image of an array of SiNWs with different thicknesses and lengths fabricated by the SCREAM process.
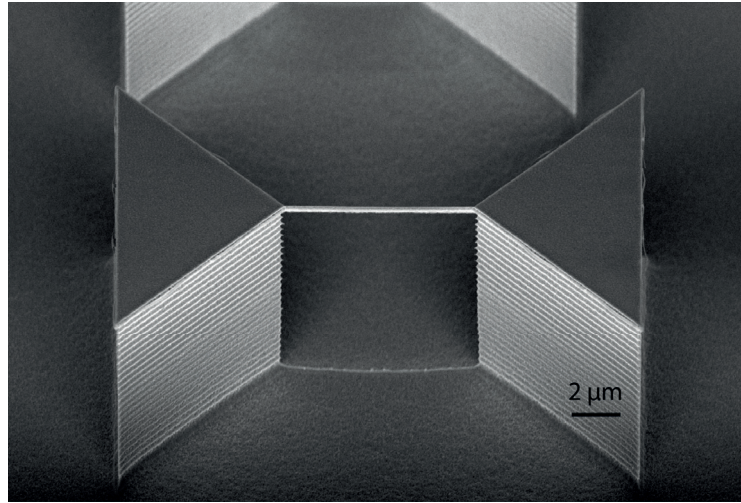
Figure 4.2 – SEM image of a single SiNW confined by the anchors.

The scan direction of the AFM cantilever was accurately aligned according to longitudinal axis of the SiNW. In order to place the cantilever tip precisely in the center of the SiNW for the bending analysis, the SiNW was first scanned in QNM mode.

The bending of the SiNW was observed by scanning over the SiNW along the longitudinal axis. Raising the imaging force set-point influences directly the bending of the SiNW. Figure 4.3 depicts the bending behavior as a function of the applied scanning force of a 12 μm long and 80 nm wide SiNW. The interpretation of the whole image is that the apparent, *bent* SiNW is an assembly of states as a function of the applied force, since each data point represents the extracted height from a force curve. This is not to be mistaken with an image of a doubly-clamped, bent beam with an applied force at the center of the beam.

Thereafter, the center of the SiNW is roughly chosen and consecutive zooming in on the point of maximum deflection defined the point for the bending analysis. Thereafter, the AFM mode was switched to *ramp mode*, where single force curves were taken. The set-point force was gradually augmented for every force curve, until the breaking of the SiNW. Figures 4.4 and 4.5 show force curves during the bending analysis experiment on top of a SiNW with a width of 30 nm and a length of 1.5 μm. The used AFM cantilever was a FastScan-A and the experiment was performed on a Bruker FastScan AFM in the cleanroom of our microfabrication facility CMi. After the breaking of the nanowire with the AFM cantilever tip, we confirmed with the SEM that the point of fracture was in the center of the SiNW.
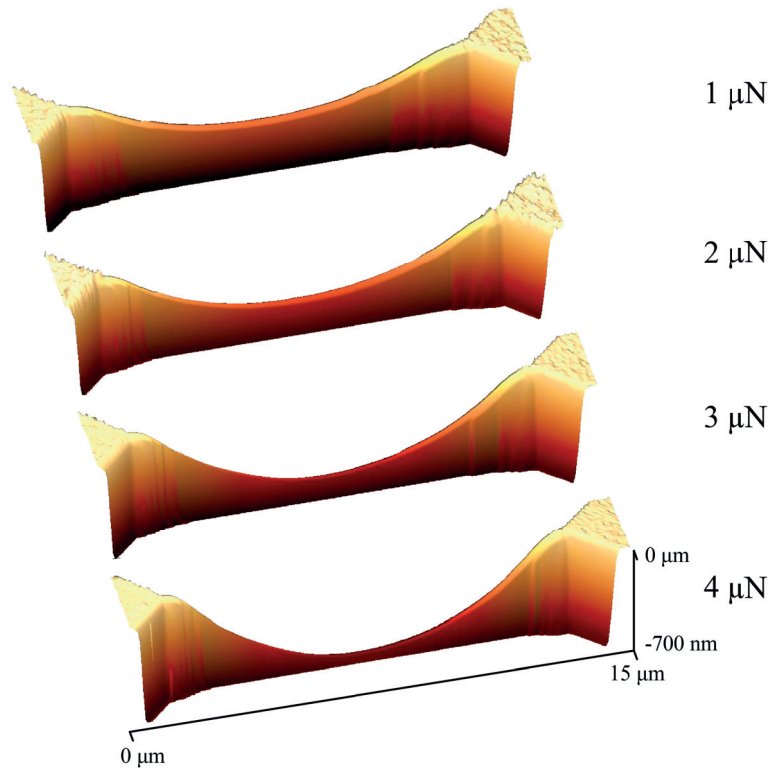
Figure 4.3 – A series of 3D AFM images of a 12 μm long and 80 nm wide SiNW taken in QNM mode. Each image is constructed as a superposition of multiple loading steps at a constant force, where the point of the application of load is scanned along the entire length of the SiNW.

Figure 4.4 shows the elastic behavior of the SiNW, where the force curves with different force set-points overlap. The inset of figure 4.4 shows the load curve with a 500 nN force set-point (light blue) overlapping completely with the load curve leading to fracture at 10.4 μN (dark blue). Moreover, the unload curve for the 500 nN force set-point curve (red) is depicted, whereas the unload curve after SiNW fracture was a straight line at 0 μN, and is not shown for the purpose of clarity.

The deflection of the AFM cantilever is presented as well in the data of the height sensor shown in figure 4.4. After subtraction of the AFM cantilever deflection effects, we obtained the force curves depicted in figure 4.5, where all force curves are shown with a vertical offset on the graph. All force curves were manually overlaid at the snap-in of every force curve.

In order to compare between data taken on different days with different FastScan-A cantilevers, we re-calibrated all cantilevers on a sapphire disk. We used the thermal tune method for the cantilever calibration [19], taking into account the correction factors for
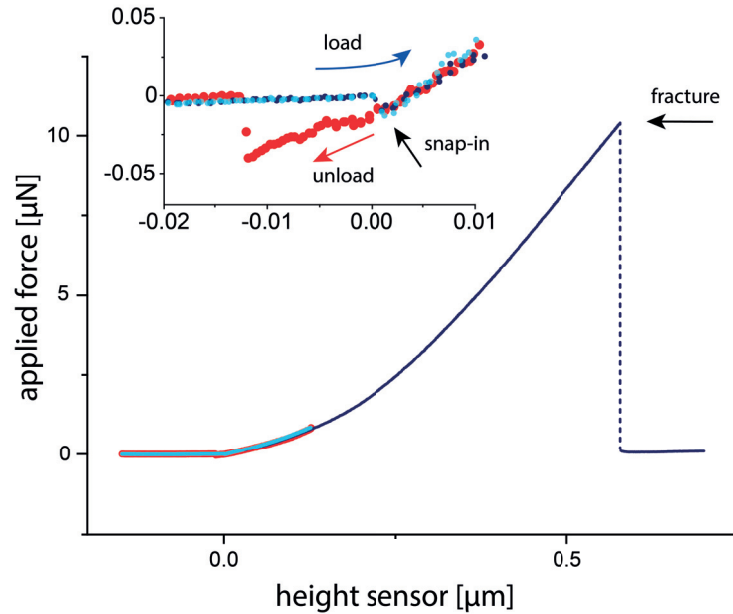
Figure 4.4 – Force curve on a single nanowire from the three-point bending analysis with the AFM cantilever tip showing loading (light blue) and unloading (red). When a high force (dark blue) is applied, the nanowire fractures.

short cantilevers and the cantilever tilt during data acquisition [157, 158, 159]. Thereafter, we re-adjusted all force curves using Bruker's NanoScope Analysis software. The force curves presented in figures 4.4 and 4.5 contain the re-calculated datasets.

The data of four different SiNWs with a width of 30 nm and a length of 1.5 μm had a fracture point between 9 μN and 11 μN and indicated an average stiffness of at least a four-fold higher than compared to values for bulk (110) silicon with an elastic modulus of 169 GPa [160]. Albeit the elastic modulus of crystalline silicon is direction dependent, we suggest that the increased SiNW flexural stiffness is partially due to the tensile stress that developed due to surface stresses on the double-clamped SiNW [161]. At the nanoscale, effects of surface stress and non-local elasticity [162], as well as intrinsic effects [163] have a significant influence on the mechanical properties of the SiNW [164].

Although mechanical analysis with the AFM tip on nanowires were conducted prior to our study, the nanowires were grown by the bottom-up fabrication approach and pinned down to the substrate. Furthermore, the bending tests with the AFM tip on the nanowires was done laterally [165, 166, 167], where the lateral force involves lateral bending as well as the torsional spring constant of the nanowire. Pioneering experiments applying a downward force with the AFM tip were done on nanowires, where the silicon substrate
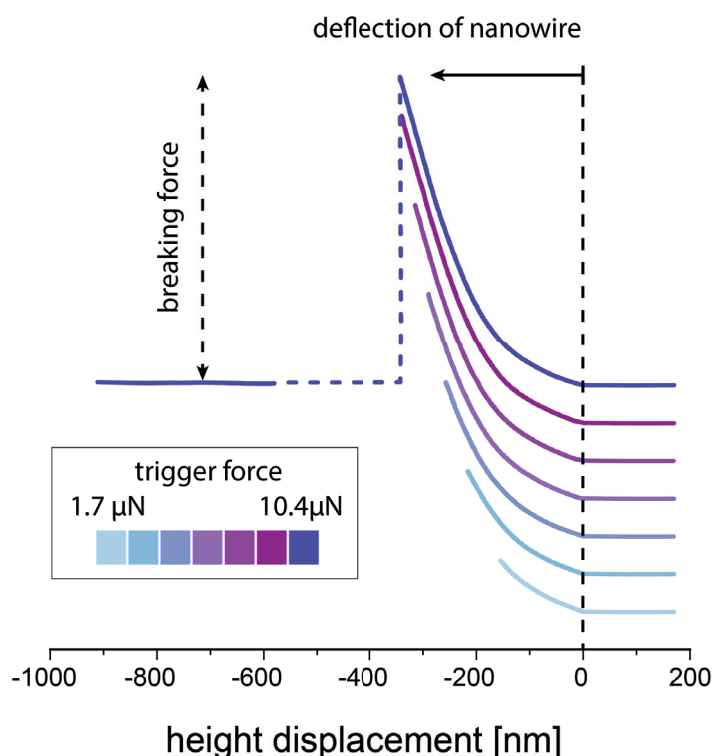
Figure 4.5 – Individual force curves of a single experiment vertically displaced. The maximal force exerted is shown by the color code, whereas the vertical direction represents force units. The force set-point was raised until the nanowire fractured.

underneath the nanowire was undercut after nanowire deposition [168] or the nanowire was less then 20 nm distant from the substrate [169]. Our approach allows the probing of suspended nanowires tens of micrometers distant from the substrate, whereas only the bending mode of the cantilever is tested due to the applied downward force of the AFM cantilever tip.

4.3 Mechanical characterization of hydrogels

Hydrogels are polymer scaffolds filled with an aqueous solution used for tissue engineering [170, 171], drug delivery apparatus [172], and 3D scaffolds for ordered cell growth [173], among other functionalities. Their bulk macroscopic elastic modulus generally differs from the local microscopic elastic modulus, whereas the local modulus is difficult to determine. The AFM inherently allows nanoindentation and is suitable for the determination of local microscopic elastic moduli of hydrogels. AFM analysis of hydrogels is done in an aqueous environment and the hydrogels need to be immobilized onto the substrate,

making the sample preparation a challenging part of the experiments.

Hereafter we discuss different types of hydrogels based on alginate, carboxymethyl-cellulose (CMC), polyethylene glycol (PEG), and polydimethylsiloxane (PDMS), whereas my part in the projects involved the AFM analysis of the samples. The work on hydrogels made from alginate and CMC was done in collaboration with Thomas Braschler and Amélie Béduer [174], and the AFM experiments based on PEG-PDMS hydrogels were done on samples made by Shinji Kondo [175].

4.3.1 Hydrogels as scaffolds for neuronal growth

The engineered hydrogels in this study present a realistic 3D microenvironment to neurons, in particular as an attachment site and ordered growth of the neuronal networks [176]. The hydrogel scaffold allows a high compressibility of up to 90% of the initial size, by conserving the viability of the neuronal network [177]. Thus, the high compressibility of the hydrogel allows an injection of the *in vitro* grown neuronal network into the brain by a syringe needle allowing minimal invasiveness without additional tissue damage [178, 179]. This allows large-scale brain tissue reconstruction by a preorganized neural tissue network. Furthermore, the hydrogels were autoclavable allowing sterility for surgical compatibility. The hydrogels used in this study are based on alginate or CMC, and are obtained by the cryotropic gelation process [174, 177].

In order to quantify the local mechanical properties of the hydrogel scaffold, we used AFM-based nanoindentation. Pioneering results were obtained by placing the AFM cantilever tip on a hydrogel strut, with the help of optical microscopy for the precise placement [180]. Although the local elastic properties of the scaffold in an aqueous solution could be obtained, AFM imaging and determination of local mechanical properties of a scaffold area remained challenging, since the pores in the hydrogel are an order of magnitude larger than the struts, which could damage the cantilever tips during the AFM tip-sample interaction.

We synthesized the hydrogel on borosilicate glass slides, where the hydrogel scaffold was covalently attached during the cryotropic gelation process and the bulk was brushed off by a water jet. Thus, we obtained a hydrogel height on the glass slides ranging between 100 nm and 1 μm. We were therefore able to analyze the hydrogel walls with the AFM on the full scan range, without damaging the AFM cantilever tip by the hydrogel pores. The AFM images of the hydrogels based on alginate and CMC taken in milli-Q water with QNM mode are depicted in figure 4.6.
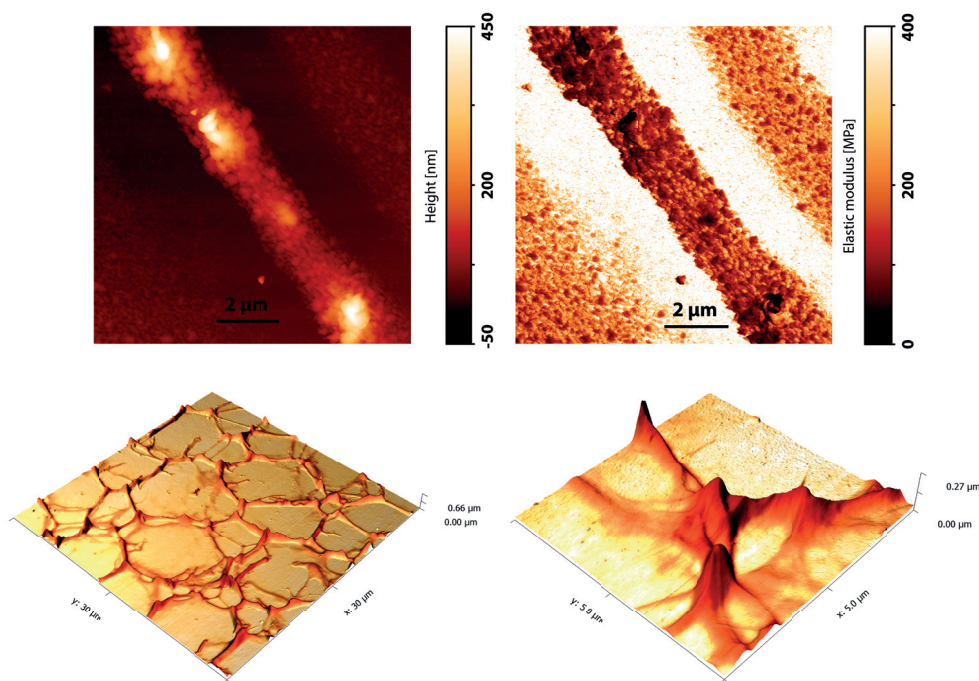
Figure 4.6 – AFM images of the height and elastic modulus of hydrogels based on alginate (top row) and CMC (bottom row). The AFM images of the hydrogel based on CMC (bottom row) represent the height data in 3D and are overlaid with the elastic properties map. A brighter color stands for a higher value.

The AFM images of the hydrogel based on alginate show the height (figure 4.6 top left) and elastic modulus (figure 4.6 top right) of the same area. The image was taken with a scan speed of 0.7 Hz and a resolution of 512 by 512 pixels on scan range of 10 μm and a set-point force of 20 nN. The AFM images of the hydrogel based on CMC (figure 4.6 bottom row) were taken in QNM mode with a scan speed of 0.5 Hz with a resolution of 1024 by 1024 pixels on a scan range of 30 μm (bottom left) and 1 Hz with a resolution of 512 by 512 pixels on a scan range of 5 μm (bottom right) and a set-point force of 10 nN (both bottom images).

The local elastic properties of the hydrogel were obtained by the QNM imaging mode and were confirmed by the force-volume method using the TAP150A cantilever for the alginate based hydrogels, and ScanAsyst-Fluid cantilever for the CMC based hydrogels. We calibrated the AFM cantilevers using the thermal tune method [19] and we used reference samples of known elastic modulus (PFQNM-SMPKIT-12M, Bruker) in order to determine an eventual correction factor for the obtained quantitative data of the hydrogels. We determined the local elastic modulus of hydrogels based on CMC to be 4.2 ± 1.4 MPa and for the hydrogel based on alginate to be 117 ± 14 MPa. This is in strong contrast with the

macroscopic properties of the hydrogel scaffold, 0.7 ± 0.1 kPa for the CMC based hydrogel, which is over 5 orders of magnitude lower than the microscopic properties.

The obtained macroscopic elastic properties are comparable to the elastic properties of the brain tissue [181]. Matching the elastic properties of the implanted material with the surrounding tissue is important for improved biocompatibility and in order to avoid inflammatory reactions [182]. On the other hand, the high microscopic elactic modulus of the discussed hydrogel is favorable for an ordered, three dimensional growth of the neural network within the hydrogel scaffold.

4.3.2 Hydrogels with mechanical fuse links

Conventional hydrogels generally exhibit brittleness when mechanical load is applied. The polymer strands, which break under load, create local stress concentration that lead to crack propagation. Finally, the hydrogel exhibits a sudden rupture due to the crack propagation. Moreover, conventional hydrogels are in a swollen state, when in aqueous solution, where the polymer strands of the hydrogel are extended, leaving limited possibility for elastic deformation of the bulk hydrogel [183].

Although highly stretchable hydrogels have been developed, allowing reconstruction of the internal damage [184], the reconstruction mechanism are inaccurate under physiological conditions. The goal of the hydrogel development based on PEG and PDMS is to obtain a reliable biomaterial exhibiting constant material properties under repeated stress.

The idea behind the PEG-PDMS hydrogel is to create a mechanical fuse, which bursts under the load exceeding the elastic regime of the bulk hydrogel. Local breaking of the polymer strands that would lead to crack propagation and final rupture would thus be prevented. For the developed hydrogels used in this study, linear-PDMS and linear-PEG polymer strands were crosslinked by a tetra-PEG crosslinker [175, 185, 186]. Hydrogels with different ratios between linear-PDMS and linear-PEG polymer strands were made, whereas *r* signifies the molar ratio and is defined as r = (linear-PDMS)/(linear-PDMS + linear-PEG), as used in figure 4.7.

Our goal was to investigate the linear-PDMS influence on the hydrogel. Although morphological differences between the hydrogels with different PDMS content is visible, the local elastic modulus value is homogeneous for a hydrogels of a specific PDMS content. Nevertheless, the elastic modulus between the hydrogels of different PDMS content raises twofold between r=0.25 and r=0.5 and over a twofold for r=0.75 in respect to r=0.5.
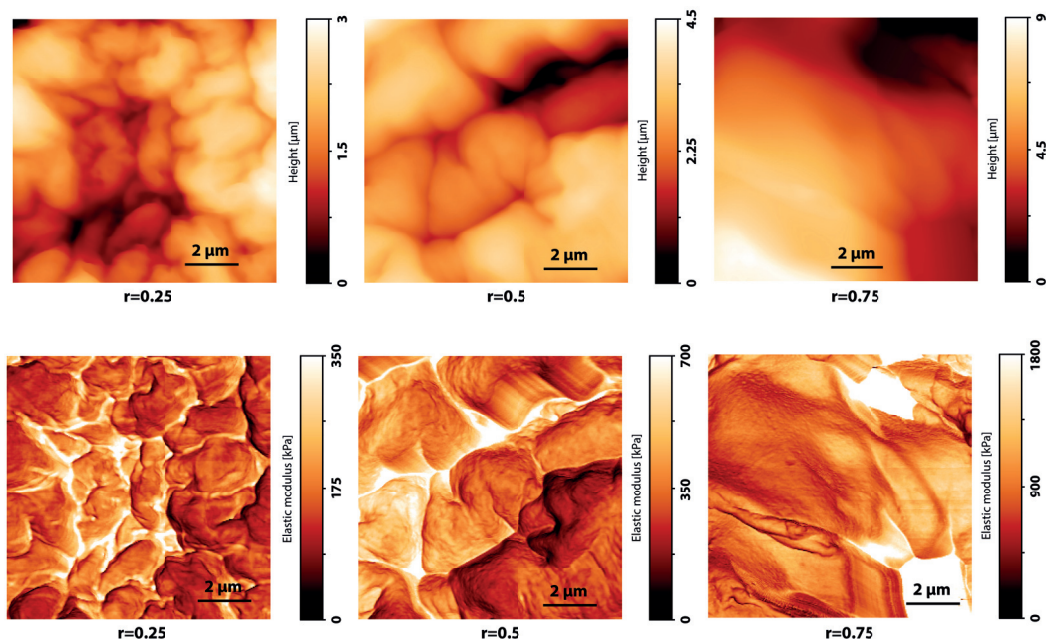
Figure 4.7 – AFM images of the height (top row) and elastic modulus (bottom row) of hydrogels based on PEG-PDMS. The *r* value below each subfigure signifies the molar ratio between PDMS and all linear polymers in the hydrogel. All images were taken in milli-Q water and in QNM mode with a scan speed of 0.2 Hz and a resolution of 256 by 256 pixels on scan range of 10 μm and a set-point force of 4 nN.

The data was taken on three different spots on the same hydrogel with a specific PDMS content. The AFM cantilevers were calibrated on a sapphire disk by using the thermal tune method [19]. Moreover, we used reference samples in order to calibrate for the quantitative elastic modulus values, as described in the aforementioned section 4.3.1. For the data presented in figure 4.7, we obtained for the hydrogel with a PDMS content of r=0.25 and elastic modulus value of 150 ± 57 kPa, for r=0.5 we obtained 332 ± 143 kPa, and for r=0.75 we obtained 854 ± 260 kPa. The data with AFM height values close to the substrate was not included in the elastic modulus calculations. Nevertheless, care must be given for the interpretation of the exact numeric values of the elastic modulus data [99].

The data presented in figure 4.7 shows a microscopically isotropic hydrogel. We did not observe patches of PDMS and PEG on the surface of the samples, which would be differentiated by different local elastic properties. The hydrogel appeared as a consolidated material, having microscopic elastic properties as a function of the PEG-PDMS ratio.

4.4   Discussion and conclusion

In this chapter, we investigated nanomechanical properties of soft and hard samples with the AFM. The applied method for SiNW was not reported prior to our work, to the best of our knowledge. During the analysis of the doubly-clamped SiNW, we had to proceed with extreme caution prior to placing the AFM cantilever tip on top of the SiNW. By precisely adjusting the scan angle with the help of the anchors confining the SiNW and using QNM mode for AFM analysis, we were able to position the AFM cantilever tip in the middle of the SiNW for the consecutive fracture experiments. For the SiNW mid-point, we took the point of maximum deflection of the SiNW as a function of the applied force during QNM imaging, well aware that intrinsic inconsistencies of the SiNW can shift the maximum deflection from the geometric mid-point, thus alter the experiment results.

Furthermore, data was taken on multiple days using different AFM cantilevers. Although a thorough calibration was conducted on every cantilever prior to experiments with SiNWs, we did a full calibration of all used cantilevers withing one session on the same day. This resulted to posterior adjustments of the acquired SiNW data, in order to compare data taken on different days. We strongly suggest to first calibrate all AFM cantilevers to be used before starting the experiments and take the sample data in one session, in order to avoid laborious adjustments after the experiment. We followed this approach strictly during the hydrogel experiments.

Another issue has to be solved for the analysis of hydrogels prior to an experiment and this is the correct choice of the AFM cantilever. In particular, when the stiffness of the sample is unknown such as for various types of hydrogels that we analyzed, first a range of cantilevers with different spring constants has to be tested. We relied on a practical guide for the cantilever selection [187]. Only when the elastic modulus of the sample is covered by the AFM cantilever, a nanomechanical analysis can be conducted. For all hydrogel experiments we relied on Bruker's QNM mode for data acquisition, but we confirmed the obtained absolute values with samples of known material stiffness and as well through the established force-volume AFM mode.

5 Multilayer cantilevers for atomic force microscopy

5.1 Introduction to cantilevers for AFM

The most essential part of an AFM is the mechanical microcantilever. The properties of the cantilever influence the AFM imaging speed (mechanical bandwidth), image resolution (tip radius) and the analysis of specific samples (mechanical stiffness). In this chapter we present our approach to increase the AFM imaging speed by choosing a polymer as the main cantilever material. We discuss the encountered difficulties of the process flow and present a way how to integrate hard tips on the multilayer cantilevers with a polymer core.

The work presented in this chapter is the direct continuation of the work done by my colleague Jonathan Adams [188]. In particular two main aspects were the focus of my work, described hereafter. The first part was the amelioration of the polymer material, directly influencing the mechanical properties of the microcantilever. In particular, the goal was to obtain a higher yield regarding the fabrication of the cantilevers from a four-inch wafer. The second part presents the integration of a hard tip (silicon nitride) into the developed process flow, specifically the improvement of the tip radius and the related fabrication techniques. The fabrication was done together with my laboratory colleagues Nahid Hosseini and Jonathan Adams in our microfabrication facility CMi.

5.1.1 Influence of the quality factor

The tapping mode is one of the most broadly used AFM acquisition modes [189]. Mechanical properties of the microcantilever influence directly the resonance frequency and the quality factor, thus influencing the mechanical bandwidth of the cantilever and the detection speed of the AFM. The mechanical bandwidth can be estimated through f_0/Q,

where f_0 is the first mode resonance frequency and Q the quality factor of the cantilever. Therefore, an increase of the resonance frequency or a decrease of the quality factor will result in a higher mechanical bandwidth.

The mechanical bandwidth of the cantilever can be understood as a measure of maximum rate of topography change [188]. A change in topography results in a change of the amplitude of the cantilever oscillation. Multiple cycles are required until the amplitude reaches a new equilibrium. A higher frequency of the cantilever results in shorter cycles of the oscillation and thus the equilibrium is reached faster. Furthermore, a cantilever with a lower quality factor Q experiences an increased damping and the new amplitude equilibrium is as well reached in a shorter period of time.

AFM imaging in tapping mode in liquid has an important impact on the oscillatory behavior of the cantilever. The quality factor decreases one to two orders of magnitude as compared to imaging in air [190, 191]. The decrease of the resonance frequency is linked to the increased effective mass of the cantilever when in liquid medium. The increase of effective mass, also know as the effect of fluid loading, is linked to the motion of the microcantilever, which drags the aqueous medium around the cantilever throughout every cycle of oscillation [192]. Furthermore, the liquid medium increases the hydrodynamic damping of the cantilever that significantly alters the quality factor [193].

An increase of the resonant frequency can be achieved by decreasing the cantilever dimensions. Cantilevers with a length of ≈ 10 μm, a width of 2 μm and a thickness of ≈ 160 nm resulted in resonance frequencies of up to 650 kHz in water [194]. This enabled extremely high-speed AFM imaging, allowing direct observation of dynamic changes in biologically significant, functioning molecules (e.g. myosin V) in an aqueous medium [14].

The shrinking in size of the cantilever is limited by the AFM detection method. The widely used, optical readout method, where the deflection of the cantilever is read out by a laser beam and a photodiode [195, 196], is limiting the cantilever dimensions due to the diffraction limit of the laser. Although alternative detection methods have been developed [197], a further reduction of the cantilever dimensions may not be suitable for samples with large topography features, thus limiting their application.

5.1.2 Fabrication techniques for cantilevers

Standard AFM cantilevers are usually made out of silicon [198], SiO_2 [199, 200], or SiN [201, 202]. By changing the material to a polymer, we can mimic the hydrodynamic

damping effect in liquid, thus obtaining a low quality factor independent of the medium [188]. Pioneering fabrication results of cantilevers implementing the polymer SU-8 have successfully been achieved using a silicon mold to form the cantilever tip and obtain the cantilever after unmolding [203]. My colleague Adams *et al.* used SU-8 in order to obtain cantilevers with dimensions of commercially available AFM cantilevers, however with a lower quality factor resulting in higher mechanical bandwidth and thus an increased AFM imaging speed.

5.2 Microfabrication of multilayer cantilevers

Through various runs of the process flow and generations of cantilevers, we optimized a multitude of parameters. My contribution in particular was focused on the maximization of the cantilever fabrication yield from a four-inch wafer, the integration of hard tips into the multilayer cantilever as well as the optimization of the cantilever trip radius on the wafer scale.

Hereafter we present the process flow of the multilayer cantilevers in its final form. In subsequent sections we explain the details of specific steps regarding development and particular adjustments of the process flow that had an important impact. The fabrication was entirely done in the cleanroom of the center of micronanotechnology (CMi) at EPFL and the detailed process flow used in the CMi is given in appendix C.

5.2.1 Process flow for multilayer cantilevers

The main steps of the process flow are depicted in figure 5.1. We used a standard four-inch silicon wafer with a thickness of 380 μm and polished on both sides. The first step is to deposit a 20-100 nm thin layer of SiN through LPCVD. Thereafter, we used e-beam lithography to write the top side pattern into the ZEP e-beam resist and RIE to transfer the pattern into the SiN layer.

The top side wafer pattern contained alignment marks, written by a course e-beam, and patterns for the cantilever tip, written by a extremely fine e-beam. The patterns for the tip consisted only of circles, which after KOH wet etching will result in V-shaped pits (figure 5.1a). Ever since the technique was applied to obtain V-shaped pits decades ago [69, 204, 205], we used this technique together with circular patterns to obtain a square V-shaped pit, as depicted in figure 5.2 with a close-up of the lowermost point shown in figure 5.3 imaged by SEM at 10 kV acceleration voltage. In contrast, a square pattern that is slightly misaligned in respect to the crystalline axis of the (1 0 0) silicon wafer, will result

(a) Step 1: Creation of V-shaped pits with KOH using SiN as a hard mask.

(b) Step 2: Oxidation of silicon and SiN deposition.

(c) Step 3:Wafer bonding with BCB.

(d) Step 4: Wafer through KOH etch.

(e) Step 5: Aluminum deposition on both sides of the wafer.

(f) Step 6: Dry etching and aluminum wet etching for cantilever definition.

(g) Step 7: Deposition of the reflective layer.
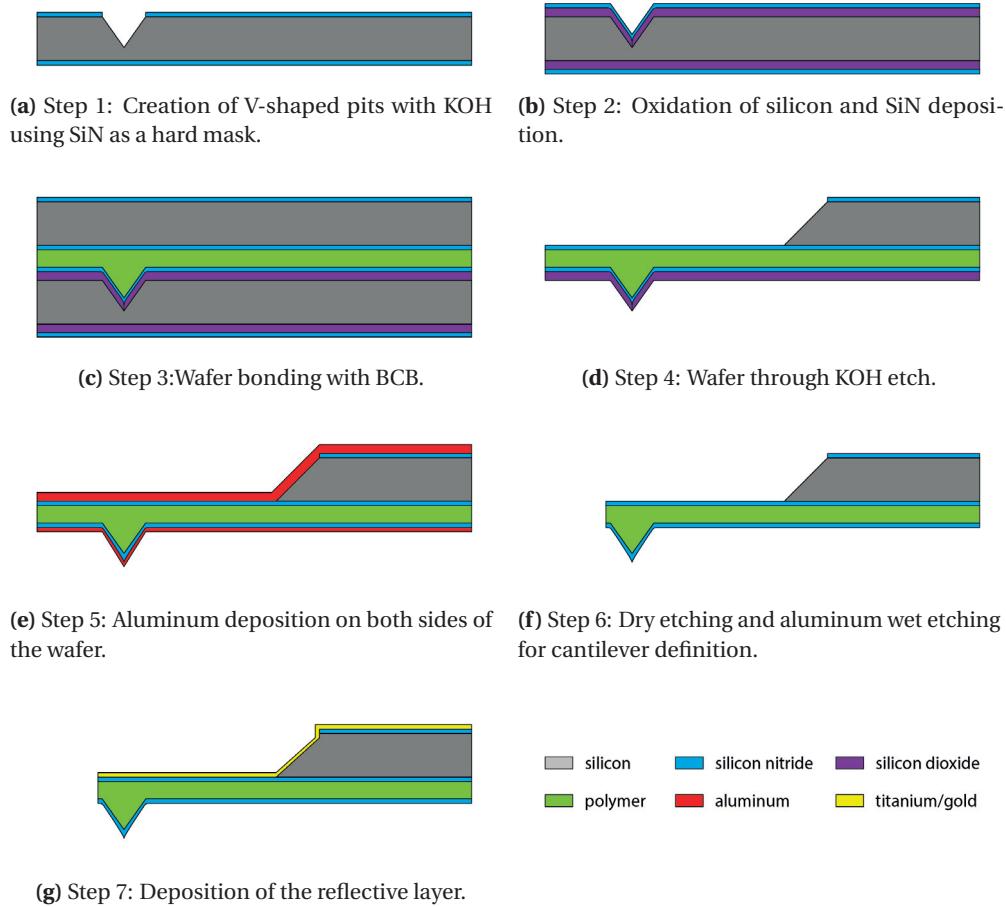
Figure 5.1 – Process flow with the main microfabrication steps of the multilayer cantilevers with hard tip integration.

in a rectangular, rather than the wanted square shape of the V-shaped pit.

After the square V-shaped pit was obtained, we used thermal oxidation to transform the outermost silicon layer into SiO_2. Oxidation of silicon results in a sharpening of the V-shaped pit [206]. The lowermost point of the V-shaped pit translates directly into the cantilever tip and sharpening is directly influencing the tip radius, since we use the V-shaped pit as a mold. Thereafter we deposited low stress SiN through LPCVD (figure 5.1b). The thickness of the deposited SiN layer will be the outermost layer of the multilayer cantilever.

A complementary double-side polished silicon wafer with the same SiN layer thickness is bonded with the wafer containing the cantilever tip (figure 5.1c). The bonding material is a viscoelastic material responsible for the low quality factor of the cantilever. We used
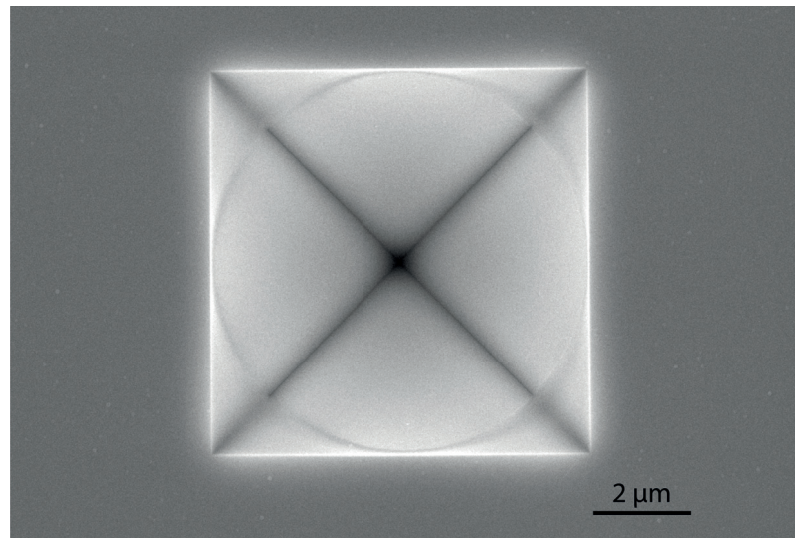
Figure 5.2 – V-shaped pit after KOH etching with a circular SiN etch mask.
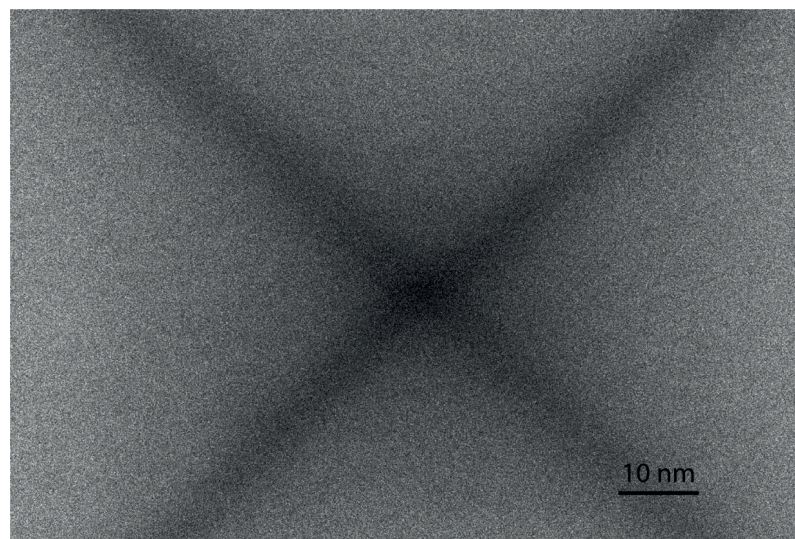
Figure 5.3 – Close-up of the lowermost point of the V-shaped pit.

benzocyclobutene (BCB), with the commercial product named CYCLOTENE 3022 (The Dow Chemical Company) for the wafer bonding. In particular CYCLOTENE 3022-46, which is suitable for a polymer layer thickness of 2-11 μm. BCB can be spin coated on one or both wafers for bonding, depending of the targeting polymer thickness. For the wafer bonding, we used the SB6 bonding machine (Süss Microtech) as shown in figure 5.4. After bonding, the wafer bond is hard cured under a N_2 atmosphere at 250° C for 60 min with an initial ramping to 250° C for 30 min.
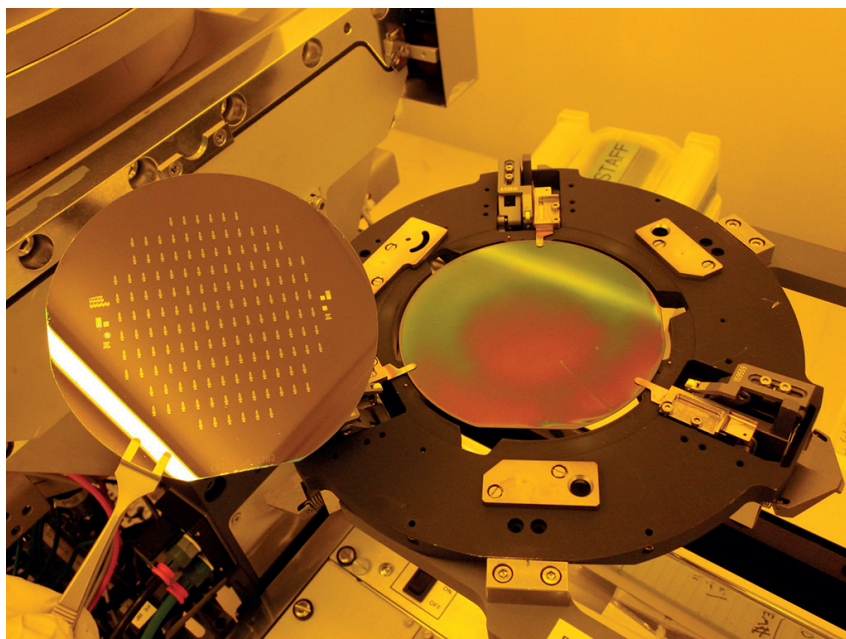
Figure 5.4 – Wafer bonding with BCB. A coated wafer is place in the holder and the complementary wafer (held by tweezers, left) is placed on top of the coated wafer using spacers.

Continuing the process flow, we patterned the bonded wafer through standard photolithography. The side of the wafer bond with the SiN-Si-SiN wafer contained a pattern with cantilever chip bodies and convex corner compensation structures [68]. On the side of the wafer bond with the wafer containing the hard tips, we stripped of the SiO_2 and SiN layers thus exposing the silicon. Thereafter we etched the wafer bond in 40% KOH at 60° C overnight with a total etch time of ~19 h (figure 5.1d). We manually overetched the chip bodies such as the convex corners were overetched, leading to a simple mounting into the existing AFM cantilever chip holders. The BCB layer is covered from both sides with a SiN layer and resists the hour-long etch. Thus no wafer chuck is needed, as shown in figure 5.5, and a higher number of wafers can be processed simultaneously, allowing a higher throughput. The chuck allowed an etching from both sides and was only used in order to protect the interface at the edge from KOH. This method was developed for parylene-C as the cantilever core material and the wafer chuck is not needed when BCB is used as the bonding material.

Although the thermally grown oxide is attacked during the KOH etch, we completely removed the oxide layer using buffered HF. Thereafter, we deposited a 2 μm thick aluminum on the chip body side of the wafer, which is serving as a mechanical support layer. On the cantilever tip side, we deposited a 300 nm thin aluminum layer, which is acting as a hard mask during the consecutive dry etching (figure 5.1e).
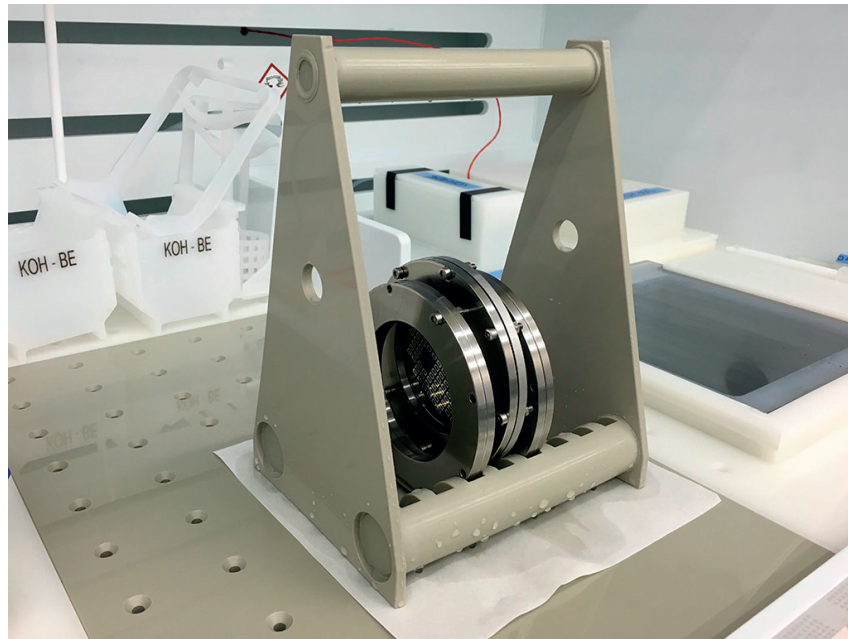
Figure 5.5 – KOH etching of the wafer bond using a chuck. The size of the chuck holder allows etching of only a few wafer bonds simultaneously.

During our experiments, we found that a thick photoresist layer of over 20 μm is not sufficient enough to withstand the BCB dry etch. We therefore chose aluminum as a hard mask, which showed a vertical etch rate of 15 nm min^{-1} as we determined during our experiments. For the patterning of the aluminum on the cantilever tip side of the wafer, we used a 12 μm thick photoresist (AZ 9260, MicroChemicals) in order to cover completely the cantilever tips. Every wafer was analyzed carefully with the SEM, in order to check that the cantilever tip was covered with the photoresist. Only after a successful check, the patterned aluminum was etched with an aluminum etchant consisting of H_3PO_4 (85%) + CH_3COOH (100%) + HNO_3 (70%) in the ration 75:5:3. Since the thick aluminum layer on the chip body side is as well etched during this wet etching, we precisely timed this process step and stopped the etching as soon the aluminum on the cantilever tip side was fully etched.

The thick aluminum layer on the chip body side of the wafer is necessary, since the BCB dry etch defines the cantilever shape and removes the surrounding BCB layer. Without an aluminum layer on the chip body side we would have experienced leakage at the end of the dry etch process, which could compromise the etching process and the loosely attached cantilever chip bodies. The BCB dry etch consisted of three main etching steps, where the first and the last etch step consist of SiN layer removal using CHF_3/SF_6 dry etch chemistry. During the second etch step, we removed the BCB polymer layer using CHF_3

chemistry. The BCB dry etching was performed on the SPTS Advanced Plasma System (LPX, SPTS Technologies) and the detailed etch parameters are highlighted in table 5.1.

etch layer	gas	flow [sccm]
SiN	CHF_3	50
	SF_6	10
BCB	CHF_3	10
	O_2	20

Table 5.1 – Parameters for the BCB dry etching.

After BCB dry etching, we removed the aluminum layers on both sides using the aforementioned wet aluminum etchant (figure 5.1f). At this point, the cantilevers are connected to the silicon wafer only by BCB connection bridges, which necessitates a careful handling. The final step consists of the deposition of a thin reflective layer on the chip body side of the wafer. We first sputtered a 5 nm layer of titanium followed by a 20 nm layer of gold (figure 5.1g) using the DP 650 (Alliance-Concept). The titanium is used in order to have a good adhesion between the gold layer and the SiN layer [67]. The cantilever with the integrated hard tip at the end of the process flow is depicted in figure 5.6 and the close-up of the tip is shown in figure 5.7.
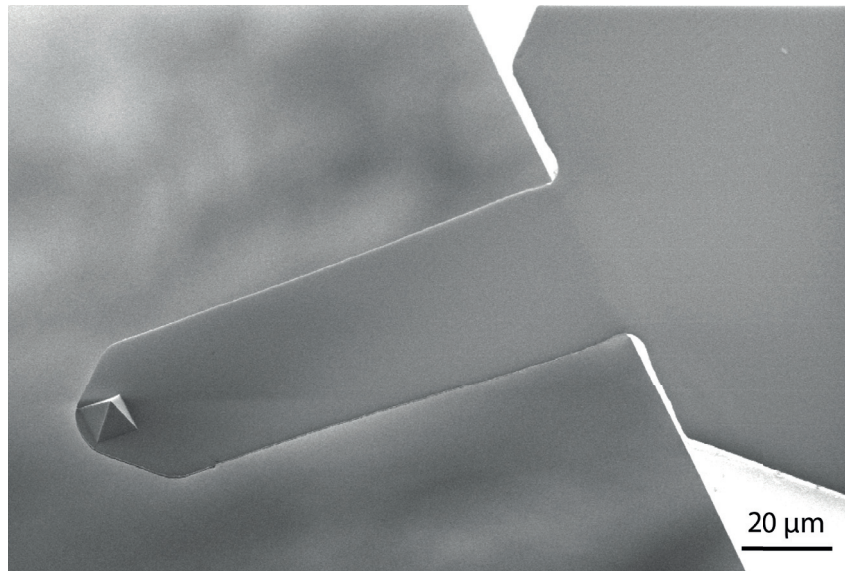
Figure 5.6 – SEM image of the multilayer cantilever with an integrated hard tip.
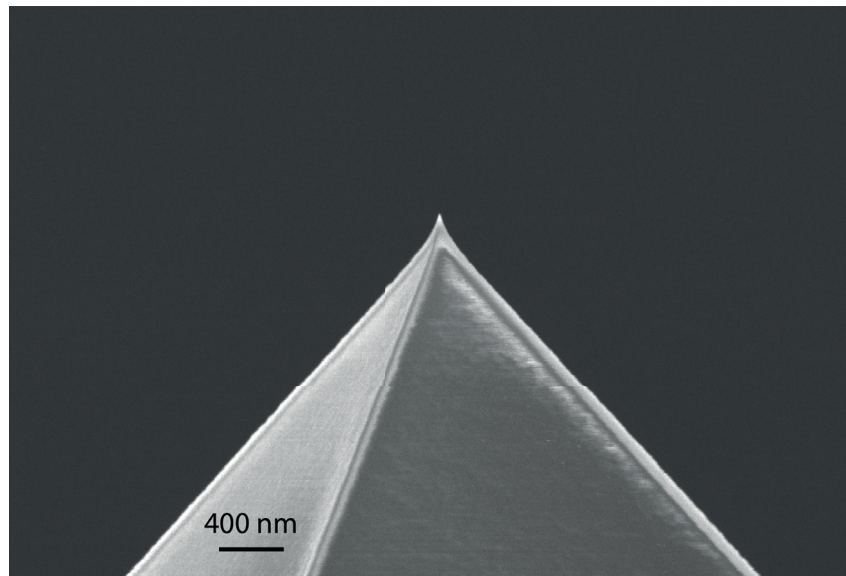
Figure 5.7 – Close-up SEM image of the fabricated hard tip.

5.2.2 Discussion on fabrication yield optimization

My work on this project started with the optimization of the fabrication yield on the wafer scale. Pioneering results using parylene-C as bonding material suffered from a poor quality of the bond. Moreover, in order to make the bonding possible, adjustments had to be undertaken regarding the KOH wet etching and the photolithography of the etched wafer bond. In order to protect the edge of the wafer bond to be attacked during the wafer-through KOH wet etch, a wafer chuck needed to be used. This resulted in a silicon ring at the edge of the wafer bond (figure 5.8a), which presented an additional challenge for the consecutive photolithography step. The photolithography mask needed to be milled outside of the cleanroom in order to accommodate the 380 μm thick wafer ring and thus allow hard contact photolithography.

BCB as bonding material significantly improved the overall fabrication yield. We have developed a bonding recipe that resulted repeatedly in an outcome without any gas pockets on the full wafer scale. Gas pockets will result in loss of cantilevers after the wafer-through KOH etch and the created holes are problematic for vacuum chucks used for spin-coating of photoresist or dry etching. Moreover, we have found that the adhesion of the bond between the BCB polymer and the SiN layer was sufficient to withstand the ~19 h long KOH etching at 60° C without using a chuck, as shown in figure 5.5. This allowed the complete dissolution of the wafer without leaving a ring structure at the edge. The comparison between a wafer bonded with parylene-C versus the BCB polymer after

KOH wafer-through etching is shown in figure 5.8, highlighting the improvement of the process flow. The wafer design used contained a ring structure at the edge of the wafer, which was necessary in order to provide the clamping possibility of the KOH wafer chuck depicted in figure 5.5.
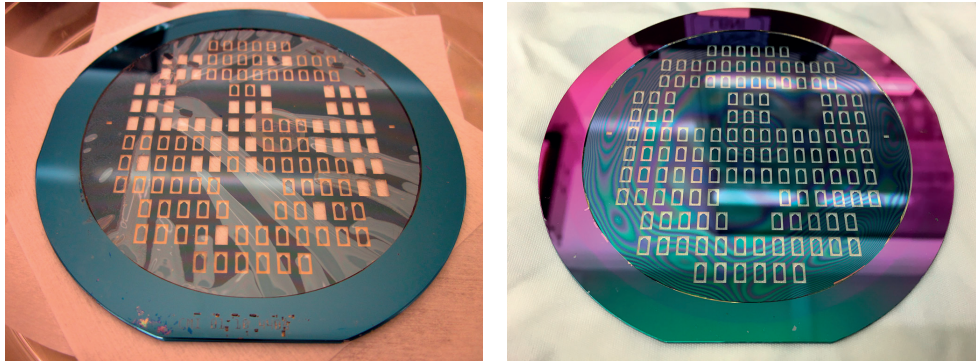
(a) Bonding result using parylene-C after KOH wafer-through etch.

(b) Bonding result using BCB after KOH wafer-through etch.

Figure 5.8 – Bonding results with parylene-C and BCB after wafer through etch.

The lack of the ring structure at the edge of the wafer bond after KOH etching improves the process flow in two ways. On one hand, the ring does not need to be patterned on one side of the wafer bond. The hard mask material on the tip side of the wafer bond can be removed entirely by dry etching, removing one photolithography step. Moreover, the fabrication does not necessitate a wafer chuck, allowing more wafers to be processed at once during the overnight KOH wet etching. On the other hand, the photolithography masks containing the cantilever structure used after the KOH etching, do not necessitate physical modification outside the cleanroom to accommodate the ring structure. Changes can therefore be implemented faster into the cantilever design. In conclusion, BCB as bonding material improved significantly the overall cleanroom processing time for the multilayer cantilever fabrication.

Prior to bonding, we spin-coated the adhesion promoter AP3000 (The Dow Chemical Company) with a rotation of 500 rpm for 10 s and 3000 rpm for 30 s with nitrogen gas flow only after 3000 rpm are were reached. The BCB polymer was spin-coated with a rotation of 700 rpm for 9 s followed by 4000 rpm for 30 s in order to have a final thickness of 4 μm. The first pre-baking step occurred at 80° C for 80 s and the second pre-baking step occurred at 150° C for 20 min on hot plates. The pre-baking steps are mandatory in order to avoid degassing of the solvents during the bonding, which can lead to gas pockets formation [207]. Furthermore, for the separation of the two wafers prior to bonging, we used spacer between the wafer that are automatically removed once the vacuum of 3 mbar is achieved

inside the bonding chamber. Our developed bonding recipe is detailed in table 5.2.

process step	tool action	parameter set point
Step 1	top and bottom plate	30° C
	chamber pressure	1000 mbar (purged)
	tool pressure	0 mbar
Step 2	chamber pressure	3 mbar (pump down)
Step 3	top and bottom plate	160° C (heat)
Step 4	contact with central pin	
Step 5	clamps out	
Step 6	spacers out	
Step 7	tool down	
Step 8	tool pressure	2500 mbar
Step 9		remain for **3 min**
Step 10	tool pressure	0 mbar (tool release)
Step 11	chamber pressure	1000 mbar (purge)
Step 12	tool up	

Table 5.2 – Main steps in the BCB bonding recipe.

The dry etching of the BCB polymer requires fluorine chemistry, such as SF_6, CF_4 or CHF_3 [208, 209]. We have obtained the best experimental results by using a CHF_3/O_2 gas as shown in table 5.1. Moreover, we relied on a aluminum hard mask instead of a photoresist soft mask for the BCB dry etch. We have observed that the photoresist initially covering the cantilever tip is thinned down during the etching, thus exposing the apex of the cantilever tip and the tip is attacked by the CHF_3 etch chemistry. The vertical etch rate of aluminum for the used CHF_3 etch chemistry is only 15 nm min^{-1} and therefore an aluminum layer with a thickness of over 150 nm should be used.

The initial design of the multilayer cantilevers contained a 100 nm thick SiN layer surrounding the BCB polymer. In order to improve the quality factor, we fabricated cantilevers with only a 20 nm thick SiN layer. Although the 20 nm SiN layer can be used as a KOH wet etch mask, the SiN layer will be attacked during the consecutive BHF etch used to remove the thermal oxide layer around the cantilever tip. The etch rate of thermally grown oxide is two orders of magnitude higher than for low stress silicon nitride (100 nm min^{-1} for SiO_2 versus 1.3 nm min^{-1} for SiN) [93]. During the time required to remove the SiO_2 layer under the etch conditions in the CMi cleanroom, the exposed SiN layer is etched for roughly 10 nm. While this change of thickness only represents a 10% change for a 100 nm thick SiN layer, the 20 nm SiN layer is significantly affected by this change.

Moreover, once the thermal oxide is removed, the BHF attacks the apex of the SiN can-

tilever tip in both cases, which can have a negative influence on the tip sharpness. We therefore propose, to etch the thermally grown oxide during the KOH wet etch, since the SiO_2 layer is as well attacked by the KOH etch [93]. In order to compensate for the slow etch speed of SiO_2 in KOH, the convex corner compensation structures would need to be adjusted [68]. This modification of the process flow would result in the conservation of SiN layer symmetry that can influence the final bending of the cantilever and preserve the apex of the SiN tip, since KOH does not etch the SiN layer [67].

5.2.3 Fabrication and integration of hard tips

In order to obtain sharp tips on AFM cantilevers, various techniques exist. Thermal oxidation of silicon tips is a common technique, where first a SiO_2 mask was patterned with round shapes. The silicon underneath the round SiO_2 patterns were then wet-etched anisotropically [201] or isotropically [210] until the tip mask fell off. The obtained silicon tips underwent a thermal oxidation in order to sharpen the apex region of the silicon tip. Although the thermal oxidation allows an atomically sharp silicon tip, the final tip after SiO_2 removal and consecutive native oxidation in air was found to be around 10 nm for this technique [201].

Different techniques used oxidation of silicon-rich SiN layer in order to sharpen the apex of the cantilever tip down to a radius of 17 nm [211]. Furthermore, a fracture technique was applied using a rather exotic method in order to obtain sharp silicon tips, although the silicon apex oxidizes in air to naturally form SiO_2, thus blunting the tip radius [212]. Tips were as well deposited using an electron beam and growing a spike of organic material allowing a tip radius of less than 10 nm [159, 213, 214]. Recent techniques using nanostencil lithography deposited SiNW and carbon nanotube tips on AFM cantilevers allowing a radius of less than 5 nm and a very high aspect ratio of over 90:1 (tip height to radius) [215].

Our approach to hard tip fabrication was to first fabricate the sharp cantilever tip on the wafer, which we then bond to a complementary wafer. The wafer bond is then further processed to obtain the final cantilever. Our approach allows batch fabrication and a hard tip integration on the full wafer scale.

Our first results were achieved by using standard photolithography to pattern a SiO_2 layer. Circular patterns were written directly onto the photoresist with a ultraviolet (UV) light source at $\lambda = 355$ nm (VPG200, Heidelberg Instruments Mikrotechnik). The obtained results showed that the circular pattern suffered from a non-uniformity in respect to the symmetry of the circular patterns with a diameter of up to 10μm. The resulted V-shaped

pit after KOH etch had a rectangular shape unlike the results showed in figure 5.3. To counteract this issue, we switched to e-beam lithography in order to pattern the circular shape with a high degree of uniformity regarding the symmetry of the circular patterns.

Even though we used e-beam lithography for the patterning of the circular shapes, we did not obtain a square V-shaped pit throughout all patterns on the wafer by using SiO_2 as a KOH etch mask. The obtained cantilever tips after the whole process flow showed tip radii of up to 100 nm. An explanation would be that the 400 nm thick SiO_2 layer is non-uniformly etched around the circular patterns throughout the wafer during the 25 min KOH etch at 60° C. The resulting non-symmetry would result in a slightly rectangular V-shaped pit, affecting the final tip shape as shown in figure 5.10e.

By choosing low stress SiN as a KOH etch material, we did not observe the aforementioned etching effect of the mask and obtained a square shape of the V-shaped pits after KOH etching repeatably on the full wafer size. The results were confirmed on three different wafers with two independent KOH and HF wet etching steps. Moreover, SiO_2 is known to be etched in the range of a few nanometers per second in KOH, whereas SiN was not observed to be etched in KOH [216].

In order to not alter the lowermost point of the V-shaped pit after KOH etching, we relied on wet etching of the mask material instead of RIE. Although SiO_2 can easily be removed through HF or BHF and not affecting the silicon, we used HF as well in oder to remove the SiN layer used in the later generation as the KOH etch mask. An alternative choice would be, if the equipment is present, hot phosphoric acid at 160° C [67].

Figure 5.9 represents a full wafer evaluation of cantilever states after a process flow run during the microfabrication. The cantilever shape was evaluated together with the tip placement and tip radius. Figure 5.10 represents different cases encountered during the evaluation and shows the nomenclature used in figure 5.9. The loss of cantilever tips, and as well cantilevers, is depicted by black cells. The concentration on one side of the wafer could be explained by fabrication defects during the processing, since other areas of the wafer having cantilevers with the same dimensions, contain usable cantilevers with acceptable tip radii of <25 nm. Note that through the vertical SEM analysis of cantilever tip shown in figures 5.10e and 5.10f, we evaluate the tip diameter as applied in figure 5.9, and not directly the commonly used tip radius. The SEM analysis represents only a rough estimation of the tip radius, which is determined more precisely later on in the laboratory by AFM. For this wafer, we have a total of 42% of all chip bodies that contain a usable cantilever with a tip radius of less than 25 nm. 22% of cantilevers contain a tip radius between roughly 25 nm and 50 nm. The remaining 36% of cantilever chip bodies are

Wafer #5709

Cantilever	0=broke; 1=bad; 2=usable; 3=good; 4=perfect
Tip	0=not present/fully etched; 1=under-etched; 2=whole present
Tip Diameter	0=too large >100nm; 1=<100nm; 2=<50nm

Figure 5.9 – Evaluation of a wafer at the end of the process flow. A cell consisting of three vertical values from white to dark gray represents a placement of a cantilever chip body on the wafer. Each cantilever is evaluated by three values regarding the cantilever shape (top, white), tip placement (middle, gray), and tip diameter (bottom, dark gray). Black and very dark gray cells indicate a chip body without a cantilever/tip or a defect cantilever/tip respectively.

not usable due to a too large tip radius (>50 nm), or an etched tip that can be caused by misalignment during the photolithography step defining the cantilever outline. Only a small amount of cantilevers are broken at the end of the processing, and a few cantilevers

(a) Cantilever shape: 1 = bad.

(b) Cantilever shape: 3 = good.

(c) Tip state: 1 = partially under-etched.

(d) Tip state: 2 = whole present.

(e) Tip diameter: 0 = too large >100 nm.

(f) Tip diameter: 2 = <50 nm.

Figure 5.10 – SEM images of the evaluated cantilevers and tips with their corresponding nomenclature used in figure 5.9.

contain different inconsistencies marked by the *x* next to the *cantilever state* number in figure 5.9, making them suboptimal for further evaluation with the AFM.

The cantilever shape depicted in figure 5.10a could be improved by a better adhesion of the photoresist to the aluminum mask during the wet aluminum etching step. The *bad* shape of the final cantilevers is due to the same shape of the aluminum hard mask during BCB dry etching. The aluminum mask on the other hand is defined by photolithography

and wet etching of the aluminum. We suggest that the photoresist is under-etched during the wet etching and attacking the underlaying aluminum on particular areas of the wafer, thus resulting in the non-uniform shape of some cantilevers. Although the fabrication yield of the cantilever chip bodies is optimized, the output of usable cantilever tips on the full wafer scale can still be improved at this point of development.

5.2.4   Characterization of multilayer hard tip cantilevers

The characterization results of the fabricated cantilevers are listed in table 5.3. The results correspond to cantilevers with a BCB polymer thickness of 4 μm and SiN layer thicknesses of 20 nm. We performed the tests on our laboratory setup using the Bruker Dimension FastScan AFM head. We tested the cantilever by first determining the deflection sensitivity by engaging on a standard calibration sample. Thereafter we measured the quality factor Q, the resonance frequency in air f and the cantilever stiffness k using the thermal tune method [19]. The values in table 5.3 represent average values of three consecutive measurements that were taken for the measured parameter on at least one cantilever of the denoted dimensions. For comparison, we listed three commonly used AFM cantilevers at the bottom of table 5.3, whereas the width and the length (and stiffness for FastScan-A) were taken from the datasheet of the manufacturer Bruker, since ScanAsyst-Air and FastScan-A have a triangular shape. The values for Q, f, and k of the commercial cantilevers were determined in the same way as for our fabricated cantilevers.

The listed results in table 5.3 are an improvement of previously obtained data from multilayer cantilevers with a SiN thickness of 40 nm on both sides, having Q values above 100. Nevertheless, the quality factor is still slightly higher as compared to the commercially available cantilevers (30 by 120 μm cantilever with Q= 61 versus ScanAsyst-Air with Q=55.5). There is still room for improvement and the quality factor could further be lowered by adjusting the degree of BCB polymerization during the curing after wafer bonding. Instead of a hard cure that occurs at 250° C in 60 min after bonding, a soft cure (e.g. 210° C for 30 min or 180° C in 9 h, data supplied by the manufacturer The Dow Chemical Company) will lead to a different degree of polymerization, thus different material properties of the BCB polymer.

For the determination of tip radii of the fabricated hard tip cantilevers we used a titanium roughness tip-check sample that we scanned with 0.5 Hz with a resolution of 512 by 512 pixels on a 1.5 μm scan size. The value for the radius of the tip is taken at 10 nm from the tip apex, whereas the tip estimation is done with the software Gwyddion [217]. We obtained radii values of 12 $\pm$ 4 nm for the latest generation of our fabricated multilayer

width [μm]	length [μm]	quality factor Q	freq. f [kHz]	stiffness k [N m^{-1}]
50	200	49.7	30	0.5
	150	57.5	58	1.1
	100	65.5	118	3.5
40	160	52.5	50	0.8
	120	68	82	2.4
	80	76.8	175	4
30	120	61	89	1.6
	90	69.2	138	3
	60	70.8	253	8.9
20	80	69.3	179	2
	40	75.8	527	2.3
ScanAsyst-Air				
25	115	55.5	78	0.5
FastScan-A				
33	27	201	1800	18
AC40				
16	38	29	97	0.09

Table 5.3 – Characterization of multilayer cantilevers with a 4 μm thick BCB in between 20 nm thick SiN layers.

hard tip cantilevers. This compares to values of commercially available cantilevers such as the ScanAsyst-Fluid with a tip radius of 20 nm as given by the manufacturer Bruker. Nevertheless, the obtained tip radii are higher than e.g. for the ScanAsyst-Air with a nominal tip radius of 2 nm or the FastScan-A cantilever with a nominal tip radius of 5 nm, as given by the manufacturer Bruker.

5.3 Conclusion and outlook of multilayer cantilevers

We have demonstrated the fabrication and full wafer-scale integration of hard tips in the multilayer cantilevers. Specifically with my work done in the scope of this project, the fabrication yield on the full wafer scale was significantly increased. Over 99% of the cantilever chip bodies survived the processing and the sparse failures can be lead back to inconsistencies in the BCB layer during coating and curing. Moreover, a wafer chuck is not needed during the overnight KOH etching, enabling mass production on the full wafer scale. Nevertheless, optimization can still be achieved on the output of usable cantilevers per wafer regarding the cantilever shape as well as the tip radius.

Furthermore, the presented microfabrication of multilayer cantilever allows an encapsulation possibility for self-sensing components. Self-sensing components allow a readout without the AFM laser for the detection of the cantilever deflection, thus lowering the AFM imaging noise [218, 219]. Our microfabrication technique allows the protection of the self-sensing components against surrounding aqueous solutions, enabling AFM analysis in liquid. The developed process flow for the integration of the self-sensing elements into the multilayer cantilever with hard tips is currently being applied in the laboratory. By coating the self-sensing cantilever tips with material of specific properties, e.g. for magnetic or biomolecular recognition, we enable a variety of investigation possibilities with the AFM.

6 Conclusion and outlook

6.1 Bacterial traps as a versatile tool in microbiology

With this thesis, we present a novel bacterial immobilization technique for AFM analysis that is based on physical immobilization and active microfluidics. As detailed in chapter 3, de demonstrated that our approach is independent of bacterial species and the imaging medium. Each strain was analyzed with the AFM in the corresponding physiological medium, whereas the physiological conditions can as well contain sulfuric acid an a pH = 3 in specific cases. Sulfuric acid attacks materials such as PDMS and millipore filters not made out of PTFE (Teflon), thus the immobilization and the physiological conditions around the bacterium when the chemical etching reactions start, can be compromised. Therefore, we consider our medium independent imaging possibility as a major advantage compared to other physical immobilization methods.

Immobilization methods using a chemical treatment of the substrate, as described in section 1.3, necessitate a protocol for each specific bacterial strain. A well established chemical modification of the substrate may or may not work for a different bacterial species and even strain. For example, when the envelope properties of a genetically modified gram-negative bacterium lack specific features such as the lipopolysaccharide (LPS) layer or pili as compared to the wild type, the the bacterium presents modified attachment sites on the bacterial envelope. Thus, the immobilization method is compromised, which was relying on e.g. chemical bonding with the attachment sites of the wild type. With our bacterial traps we demonstrated that not only strain independent, but as well species independent bacterial immobilization and AFM analysis is possible. Gram-positive and -negative bacterial species with entirely different envelope compositions were successfully immobilized and scanned, stating the advantage of physical immobilization and our

approach. Furthermore, the bacterial traps are spatially well localized, making the search for immobilized bacteria on the substrate prior to AFM analysis futile. The AFM scanning can be done immediately after the bacterial suspension is placed on top of the bacterial traps. The bacterial suspension can be added even while the AFM is scanning the area of interest, containing the bacterial traps, due to the active microfluidic trapping and release.

Throughout the years the experiment setups change and during my time in the laboratory, three different combined AFM and optical microscope setups were present. In spite of the similarities, an AFM head on top of an inverted microscope, the setup of the bacterial traps had to be maintained compatible. Overall, we have conducted over 200 independent AFM immobilization experiments with the bacterial traps on the three different AFM/optical microscope setups. Two setups were used for the experiments discussed in chapter 3 and one setup was used as an proof-of-concept. The initial 90 to 100 experiments were conducted in order to optimize various device parameters as mentioned in section 2.4. At the reported development stage, we are able to immobilize and analyze bacteria during every experiment regardless of the medium and bacterial species for fluorescence and AFM analysis.

6.2   Nanotailored fabrication of bacterial traps

This thesis describes two entirely different cleanroom microfabrication methods of the bacterial traps. The first developed method is based on SOI wafers and relies on the anisotropic etch properties of KOH in order to obtain the slanted walls of the bacterial traps. The process flow steps of the SOI wafer based technique were optimized over multiple iteration and the device outcome per wafer were significantly improved as compared to the first iteration: 126 devices on a four-inch wafer of the latest iteration versus 14 devices of the first iteration. Regarding commercial industrialization, the process flow can easily be extended to six-inch wafers and larger, assuming the cleanroom processing machines are equipped with the corresponding holders for the wafer size.

With the SOI wafer based technique detailed in section 2.2, we can produce only rectangular shaped bacterial traps, being suboptimal for cylindrically shaped bacteria. Parts of a single bacterial trap that are void, namely the corners of the rectangular traps immobilizing a bacterium, allow the surrounding aqueous medium to pass through. Thus, any particles in the medium will be attracted to the void part during the experiment and can alter the data acquisition. This parasitic flow is because a pressure difference across the membrane containing bacterial traps is always present. Even though we used a pressure

controller, a pressure difference of exactly zero across the membrane, which would halt such a parasitic flow, is experimentally almost unattainable with the current microfluidic design of the device. We overcame this limitation by thoroughly filtering all aqueous media, except the bacterial suspension, which allowed an unaltered data acquisition with the AFM during a couple of hours. For experiments stretching over multiple days or weeks, a new microfluidic setup would have to be engineered. Although an alternative would be to tailor the design of the bacterial trap to fit the dimensions of the analyzed bacteria.

Nanotailored bacterial traps are enabled by the t-SPL technique. We developed a novel process flows detailed in section 2.3 and demonstrated the proof of concept results in section 3.4.1. Having no voids for parasitic flow since the bacterial traps takes the shape to encompass a bacterium results in unaltered AFM data acquisition throughout the duration of the experiment. Moreover, the bacterial immobilization is independent of the bacterial shape: round traps can immobilize cylindrically shaped bacteria by the poles and crescent shaped traps can be made for the immobilization of specific bacterial species. From the microfabrication perspective, rapid prototyping of the nanometer scale is possible with the t-SPL technique on the wafer as well as chip size. Although a different selectivity during the pattern transfer with RIE between wafer and chips exist, the selectivity can be adjusted for membranes of different materials and thicknesses. The t-SPL technique allows the immobilization of bacteria regardless of the shape and dimensions of the bacterium itself. To expand this possibility, helically coiled bacteria, namely spirochaete, could be immobilized by e.g. creating traps in the periodicity of the helical coil.

The t-SPL process flow can be optimized in at different steps. In order to overcome the long etching time when a SiO_2 membrane is used as a hard mask for KOH etching, the processing steps can be decomposed into two steps: an initial dry etch step removing the bulk silicon to the proximity of the layer containing the transferred bacterial traps, followed by a smooth KOH wet etch removing the remaining silicon up to the bacterial traps. This modification would save processing time compared to the extensively long KOH etch at low temperatures. Furthermore, we used SiO_2 due to the smooth intrinsic structure of the layer, since we had issues with low stress silicon nitride deposition at the CMi. Various wafer suppliers ship silicon wafers with SiN layers that do not show the encountered issues. Therefore, by switching back to SiN layers as the bacterial membrane material, the KOH etch time can drastically be reduced using SiN as the hard mask, compared to the current process flow.

Furthermore, the t-SPL technique is at the moment a rapid nanoscale prototyping technique. For the industrialization of the t-SPL process flow for bacterial traps, significant

changes would have to be applied. Given here is an examples encountered during the microfabrication following the SOI wafer based and t-SPL process flow: The e-beam lithography step creating the patterns of the bacterial traps takes per four-inch wafer roughly 30 min, whereas excluding the vacuum pumping and wafer handling time, less than 5 min are dedicated directly to the e-beam writing; using t-SPL, we needed 30 min to pattern roughly 50 individual bacterial traps. By extending both techniques to larger wafers or mass production, the SOI wafer based technology is advantageous in respect to the patterning time. An idea to overcome this hurdle for the t-SPL technique it to create a master wafer that is used as a stamp during nanoimprint lithography (NIL) [220, 221]. Even though the patterning of the master wafer would take the corresponding amount of time, the master wafer as a stamp for NIL would allow a significant improvement in respect to processing time. Albeit the NIL technology being applied to various materials [222, 223], a feasibility study of this idea would first need to be performed for the used materials and dimensions.

6.3 Future of the bacterial traps

In order to evaluate the potential as well as state current drawbacks of the bacterial traps as a tool in microbiology, we relied on a focus group analysis [224, 225]. The participants of the focus group knowledgeable in microbiology and familiar with the AFM technology and data acquisition. This section contains topics and cases discussed in the focus group, whereas the focus group outline and detailed focus group analysis is given in annexe D.

Bacterial traps formed an array of four by five for the initial design itterations. The membrane containing the bacterial traps, had a square design with dimensions over 100 μm. The array design was initially chosen in order to fit all bacterial traps into the scan range of the AFM, which is roughly 30 μm by 30 μm for the Bruker's FastScan AFM head. As stated by the participants of the focus group, a bacterial traps array spanning across the whole membrane would be favorable. The immobilization of bacteria would be tracked by fluorescence microscopy at first, in order to select for a well immobilized bacterium, followed by engaging and scanning with the AFM at the selected area. The latest iteration of the bacterial traps design, done after the focus group discussion, implemented such wide arrays of up to 15 by 20 traps. We did not find any difficulties during the microfabrication following the well established process flow and the integrity of the membrane was maintained.

We can expand the idea of multiple immobilization sites for bacteria even further. Instead of only one single membrane containing bacterial traps on a microfluidic chip, we can
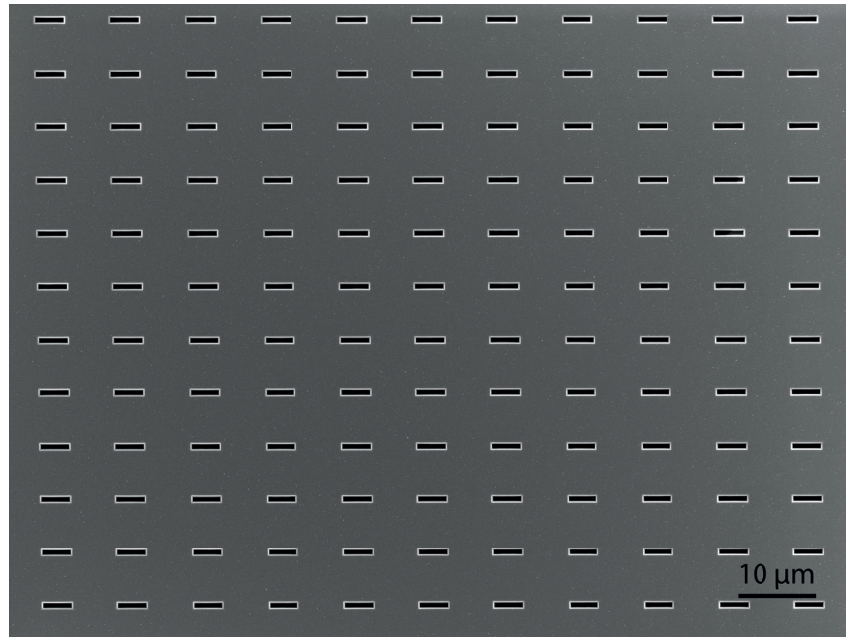
Figure 6.1 – SEM image of the latest design iteration containing a large array of the bacterial trap spanning across the entire membrane. The fabrication method is based on the SOI wafer fabrication technology.

implement multiple membranes on one single microfluidic chip. In order to maintain the established process flows and only changing the design, the distance between the membranes on a single microfluidic chip is a function of the wafer thickness: the cavity underneath the membrane has walls with an inclination angle of 54.7° due to the anisotropic etch properties of the KOH. Therefore, the thinner the wafer, the closer the membranes resulting from the KOH etch can be obtained. Although from personal experience, the thickness of a four-inch wafer allowing safe handling and manipulation is 200 μm and above. Both presented techniques, the SOI wafer based as well as the t-SPL based technique can benefit from this approach.

The bacterial traps do not need to be solely applied to immobilize bacteria. Any samples, living or solid state, having dimensions in the lower micron and submicron range can be immobilized and scanned by the AFM using the active microfluidic trapping mechanism. To give an example, by mimicking the physiological buffer inside an eukaryotic cell, organelles such as mitochondria could be immobilized and analyzed by the AFM. Furthermore, despite the explicit design for AFM analysis, any type of analysis tool can be placed on top of the microfluidic chip. On of the major benefits of the bacterial traps is that the immobilization of bacteria is ordered and spatially confined in one plane on the membrane. This allows imminent analysis with e.g. the fluorescence microscope,

instead of searching for a suitable analysis site. Since the bacterial traps allow as well the immobilization of motile bacteria, we suggest that experiments that necessitated tracking of the motile bacteria could benefit from our technological approach.

Nevertheless, a strong need as well stated during the focus group discussion, is the implementation of a temperature control. Experiments with bacteria often need to be done above room temperature in order to better mimic the physiological conditions of a specific bacterial species. Together with this amelioration, we suggest as well to implement a robust microfluidic delivery system. Bacteria as well as the analytical buffer containing different physiological conditions, such as antibiotics, could be exchanged on demand and thus facilitating the overall user handling. To conclude, we are confident that the bacterial traps and our presented approach bare the potential to make a significant impact in the field of nanoscopic analysis of bacteria.

A Appendix: Process flow for bacterial traps based on SOI wafers

Hereafter is the cleanroom process flow for the microfabrication of bacterial traps based on the SOI wafer technology, as described in section 2.2.1. The fabrication was entirely done in our microfabrication facility CMi.

Projet : Microfluidic cellular immobilization for AFM
Operator : Oliver Peric
Created : 26.05.2016 **Last revision** : 09.06.2016
Substrates : SOI 725-2-0.34 Ø100mm

Step N°	Description	Equipement	Program / Parameters	Target	Actual	Remarks	Name	Date
0	**WAFER PREPARATION**							
0.1	Stock out & check							
1	**LPCVD nitride**							
1.1	RCA1 clean	Z3/WB_PreOx_Clean	H2O:NH4OH:H2O2 (5:1:1)	15min 75°C		all done by Cmi		
1.2	HF dip	Z3/WB_PreOx_Clean	HF:H2O (1:10)	15s				
1.3	RCA2 clean	Z3/WB_PreOx_Clean	H2O:HCl:H2O2 (6:1:1)	15min 75°C				
1.4	Fast fill rinse	Z3/WB_PreOx_Clean		15min				
1.5	Trickle tank	Z3/WB_PreOx_Clean		15min				
1.6	Spin rinser dryer	Z3/Semitool	Prog. 1					
1.7	LPCVD nitride	Z3/Centrotherm		100 nm				
1.8	Nitride thick. meas.	Z3/Nanospec/AFT6100						
2	**LITHOGRAPHY - ebeam**							
2.1	O2 plasma clean	Z5/Tepla	5min @ 200W					
2.2	Dehydration	Z7	do @180°C (=set point at 200°C in Z7)	5min				
2.3	Zep spin on	Z7	4000 rpm for 60s	125nm		50% ZEP		
2.4	PR bake	Z7	do @180°C (=set point at 200°C in Z7)	5min		clean backside w/ aceton		
2.5	PR expose	Z7/eBeam	dose: 250 uC/cm^2					
2.6	PR develope	Z7	1min n-Amyl-Acetate + 1min ZEP Remover + N2 blow dry			don't let dry btw. baths		
2.7	Inspection	Z7/uScope	Resolution and alignment					
3	**Nitride DRY ETCHING**							
3.1	SiN dry etch	Z2/SPTS APS	SiO2 PR 5:1	100 nm	22s	40s (with overetch)		
3.2	Inspection	Z2/uScope						
3.3	O2 plasma clean	Z2/Tepla	7min @ 600W					
3.4	Inspection	Z2/uScope						
4	**PHOTOLITHOGRAPHY - Back Side**							
4.1	O2 plasma clean	Z11/Tepla	30s @ 200W			alt. If not SiN: use HMDS		
4.2	Frontside protection with PR	Z13/SSE Manual Coater	AZ 1512HS 2000rpm	1.7 um				
4.3	Frontside protection with PR	Z13/Hotplate	do @180°C	50s		clean backside w/ aceton		
4.4	O2 plasma surface activation	Z11/Tepla	10s @ 200W					
4.5	AZ 1512 coating	Z6/ EVG150	AZ_1512_1um1_noEBR	1.1 um		6000 rpm for 30s		
4.6	PR bake	Z6/ EVG150	AZ_1512_1um1_noEBR					
4.7	PR expose	Z6/MA/BA6	First mask, HC, 10.0 mW/cm2	1.5s		CP mode		
4.8	PR develope	Z6/ EVG150	Dev_AZ1512_upto_1um3			manual: AZ726 MIF for 40s		
4.9	PR postbake	Z6/ EVG150	Dev_AZ1512_upto_1um3			if manual: no postbake		
4.10	Inspection	Z6/uScope	Resolution and alignment					
5	**Nitride DRY ETCHING - Back Side**							
5.1	Descum	Z2/Tepla	Program: 02			10s @ 200W		
5.2	SiN dry etch	Z2/SPTS APS	SiO2 PR 5:1	100 nm	22s	40s (with overetch)		
5.3	Inspection	Z2/uScope						
5.4	O2 plasma clean	Z2/Tepla	7min @ 600W					
5.5	Remover 1165	Z2/WB_PR_Strip	Bath 1 : main remover	15min, 70°C				
5.6	Remover 1165	Z2/WB_PR_Strip	Bain 2 : clean remover	15min, 70°C				

5.7	Fast fill rinse	Z2/WB_PR_Strip	DI Rinse			
5.8	Trickle tank	Z2/WB_PR_Strip	DI Rinse			
5.9	Spin Rinser Dryer	Z2/Semitool SRD	prog 1			full Spin/Rinse/Dry
5.10	Inspection	Z2/uScope				
6	**KOH Etching**					
6.1	KOH Etching	Z5/ Plade Six Sigma	40% KOH at 60°C	340 nm	3min	
6.2	FFR	Z5/ Plade Six Sigma				x 2
6.3	Neutralization	Z5/ Plade Six Sigma	in HCl at room temperature	2h		
6.4	FFR	Z5/ Plade Six Sigma				
6.5	Nitrogen blow dry	Z5/ Plade Six Sigma	manual; no spin drying			
6.6	Inspection	Z6/uScope & Z15/SEM				
7	**ProTEK coating - Front Side**					
7.1	O2 plasma clean	Z2/Tepla	30s @ 200W			
7.2	Spin coat Primer	Z6/Süss RC8 (middle)	1500rpm for 60s; acc. 1000rpm/s			dispense w/ pipette + spread: 500rpm; acc: 2000 for 3s
7.3	Soft bake	Z6/Süss RC8 (middle)	205°C for 60s			
7.4	Spin coat ProTEK	Z6/Süss RC8 (middle)	1500rpm for 60s; acc. 1000rpm/s	6.5um		dispense from beaker + spread: 500rpm; acc 500 for 15s
7.5	First bake	Z6/Süss RC8 (end)	120°C for 120s			
7.6	Second bake	Z6/Süss RC8 (middle)	205°C for 60s			transfer w/o damage!
8	**KOH Etching**					
8.1	KOH Etching	Z5/ Plade Six Sigma	23% KOH at 90°C	740um	6h 10min	CHECK timing!
8.2	FFR	Z5/ Plade Six Sigma				x 2
8.3	Neutralization	Z5/ Plade Six Sigma		2h		
8.4	FFR	Z5/ Plade Six Sigma				
8.5	Air dry	Z5				
8.6	Inspection	Z6/uScope &/or Z1/SEM				
9	**ProTEK stripping and OXIDE Wet Etching**					
9.1	Oxide wet etch	Z14/Acid bench	3min in 50% HF	3 min		chip by chip
9.2	Rinsing	Z14/Acid bench	Rinse 2x in 2 beaker with H2O			
9.3	Inspection	Z6/uScope & Z15/SEM				

B Appendix: Process flow for bacterial traps based on t-SPL

Hereafter is the cleanroom process flow for the microfabrication of bacterial traps based on thermal scanning probe lithography, as described in section 2.3.1. The fabrication was entirely done in our microfabrication facility CMi with the exception of the thermal scanning probe lithography, which was done outside the cleanroom in the microsystems laboratory LMIS1.

Projet : Microfluidic cellular immobilization for AFM by thermal scanning probe lithography
Operator : Oliver Peric
Created : 11.09.2015 **Last revision** : 14.09.2015
Substrates : Silicon double side polished 380µm Ø100mm + 500nm SiN-LS layer

Step N°	Description	Equipement	Program / Parameters	Target	Actual	Remarks	Name	Date
0	**WAFER PREPARATION**							
0.1	Stock out							
0.2	Check height	Z3/Nanospec AFT-6100	Si+SiN-LS	500nm				
1	**PHOTOLITHOGRAPHY - Front Side**							
1.1	O2 plasma clean	Z5/Tepla	Prog 43: 30s @ 200W	30s				
1.2	AZ 1512 coating	Z6/ EVG150	AZ_1512_1um1_noEBR	1.1 um		6000 rpm for 30s		
1.3	PR bake	Z6/ EVG150	AZ_1512_1um1_noEBR					
1.4	PR expose	Z1/DWL200	direct wafer write			alternative: Z5/VPG200		
1.5	PR develope	Z6/ EVG150	Dev_AZ1512_upto_1um3			manual: AZ726 MIF for 40s		
1.6	PR postbake	Z6/ EVG150	Dev_AZ1512_upto_1um3			if manual: no postbake		
1.7	Inspection	Z6/uScope	Resolution and alignment					
2	**Nitride DRY ETCHING - Front Side**							
2.1	SiN dry etch	Z2/SPTS APS	SiO2 PR 5:1	100 nm		40s (overetch)		
2.2	Inspection	Z2/uScope						
2.3	O2 plasma clean	Z5/Tepla	Prog. 05; Resist strip	7min				
2.4	Inspection	Z6/uScope						
3	**PHOTOLITHOGHRAPHY - Back Side**							
3.1	O2 plasma clean	Z5/Tepla	Prog 43: 30s @ 200W	30s				
3.2	AZ 1512 coating	Z6/ EVG150	AZ_1512_1um1_noEBR	1.1 um		6000 rpm for 30s		
3.3	PR bake	Z6/ EVG150	AZ_1512_1um1_noEBR					
3.4	PR expose	Z6/MA6-BA6	With Mask, HC, 10.0 mW/cm2	1.5s		CP mode		
3.5	PR develope	Z6/ EVG150	Dev_AZ1512_upto_1um3			manual: AZ726 MIF for 40s		
3.6	PR postbake	Z6/ EVG150	Dev_AZ1512_upto_1um3			if manual: no postbake		
3.7	Inspection	Z6/uScope	Resolution and alignment					
4	**Nitride DRY ETCHING - Back Side**							
4.1	SiN dry etch	Z2/SPTS APS	SiO2 PR 5:1	500 nm		120s (overetch)		
4.2	Inspection	Z2/uScope						
4.3	O2 plasma clean	Z5/Tepla	Prog. 05; Resist strip	7min				
4.4	Remover 1165	Z2/WB_PR_Strip	Bath 1 : main remover	15min, 70°C				
4.5	Remover 1165	Z2/WB_PR_Strip	Bain 2 : clean remover	15min, 70°C				
4.6	Fast fill rinse	Z2/WB_PR_Strip	DI Rinse					
4.7	Trickle tank	Z2/WB_PR_Strip	DI Rinse					
4.8	Spin Rinser Dryer	Z2/Semitool SRD	prog 1					
4.9	Inspection	Z6/uScope						
5	**Thermal scanning probe lithography - OUTSIDE CLEANROOM**							
5.1	Frontside PR patterning	LMIS1/NanoFrazor				patterning of bacterial traps		
6	**Nitride DRY ETCHING - Pattern transfer**							
6.1	SiN dry etch	Z2/SPTS	SiO2 PR 3:1 optimized	500 nm	2min 45s	use optimized recipe		
6.2	Inspection	Z2/uScope						
6.3	O2 plasma clean	Z5/Tepla	Prog. 05; Resist strip	7min				
6.4	Remover 1165	Z2/WB_PR_Strip	Bath 1 : main remover	15min, 70°C				
6.5	Remover 1165	Z2/WB_PR_Strip	Bain 2 : clean remover	15min, 70°C				
6.6	Fast fill rinse	Z2/WB_PR_Strip	DI Rinse					

No.	Step	Tool	Setting			Comments
6.7	Trickle tank	Z2/WB_PR_Strip	DI Rinse			
6.8	Spin Rinser Dryer	Z2/Semitool SRD	prog 1			
6.9	Inspection	Z6/uScope				
7	**ProTEK coating - Front Side**					
7.1	O2 plasma clean	Z5/Tepla	Program: 02			30s
7.2	Spin coat Primer	Z1/Süss RC8 (middle)	1500rpm for 60s; acc. 1000rpm/s			dispense w/ pipette + spread: 500rpm; acc: 2000 for 3s
7.3	Soft bake	Z1/Süss RC8 (middle)	205°C for 60s			
7.4	Spin coat ProTEK	Z1/Süss RC8 (middle)	1500rpm for 60s; acc. 1000rpm/s	6.5um		dispense from beaker + spread: 500rpm; acc 500 for 15s
7.5	First bake	Z1/Süss RC8 (end)	120°C for 120s			transfer w/o damage!
7.6	Second bake	Z1/Süss RC8 (middle)	205°C for 60s			
8	**KOH Etching**					
8.1	KOH Etching	Z14/Base Wet bench	20% KOH at **35°C**	380um	~77h	CHECK timing!
8.2	DI rinse	Z14/Base Wet bench				x 2
8.3	Neutralization	Z14/Acid Wet bench			2h	
8.4	DI rinse	Z14/Acid Wet bench				x 2
8.5	Air dry	Z14				
8.6	Inspection	Z6/uScope				
9	**ProTEK stripping**					
9.1	O2 plasma clean	Z2/Tepla	High_Strip_10min; 600W	10min		
9.2	Inspection	Z6/uScope & Z15/SEM				

C Appendix: Process flow for multi-layer cantilevers

Hereafter is the cleanroom process flow for the microfabrication of multilayer cantilevers, as described in section 5.2.1. The fabrication was entirely done in our microfabrication facility CMi.

Projet : Hard-tip polymer AFM cantilevers
Operator : Oliver Peric
Created : 27.09.2016 **Last revision** : 27.6.2017
Substrates : silicon <100>, 100mm, 380um, double side polished, 2 wafers

Step N°	Description	Equipement	Program / Parameters	Target	Actual	Remarks	Name	Date
0	**WAFER PREPARATION**							
0.1	Stock out & check							
1	**Low-stress silicon nitride (SiN-LS) deposition**							
1.1	RCA1 clean	Z3/WB_PreOx_Clean	H2O:NH4OH:H2O2 (5:1:1)	15min 75°C		CMi staff to perform		
1.2	HF dip	Z3/WB_PreOx_Clean	HF:H2O (1:10)	15s		CMi staff to perform		
1.3	RCA2 clean	Z3/WB_PreOx_Clean	H2O:HCl:H2O2 (6:1:1)	15min 75°C		CMi staff to perform		
1.4	Fast fill rinse	Z3/WB_PreOx_Clean		15min		CMi staff to perform		
1.5	Trickle tank	Z3/WB_PreOx_Clean		15min		CMi staff to perform		
1.6	Spin rinser dryer	Z3/Semitool	Prog. 1			CMi staff to perform		
1.7	Nitride deposition	Z3/Centrotherm LPCVD	Low stress nitride	20 nm		CMi staff to perform; deposit also 20nm		
2	**e-beam LITHOGRAPHY**							
2.1	O2 plasma clean	Z5/Tepla	5min @ 200W	5min				
2.2	Dehydration	Z7	do @180°C (=set point at 200°C in Z7)	5min				
2.3	Zep spin on	Z7	1000 rpm for 240s	>200nm		50% ZEP		
2.4	PR bake	Z7	do @180°C (=set point at 200°C in Z7)	5min		clean backside w/ aceton		
2.5	PR expose	Z7/eBeam	dose: 250 uC/cm^2			align with microscope to wafer flat		
2.6	PR develope	Z7	1min n-Amyl-Acetate + 1min ZEP Remover + N2 blow dry			don't let dry btw. baths		
2.7	Inspection	Z7/uScope	Resolution and alignment					
3	**Silicon nitrite DRY ETCHING**							
3.1	O2 plasma descum	Z2/Tepla	10s @ 200W					
3.1	SiO2 dry etch	Z2/SPTS APS	SiO2 PR 3:1	20nm	10s	overetch included; etches SiN-LS at 215nm/min & Si at 30nm/min		
3.2	Inspection	Z2/uScope						
3.3	O2 plasma clean	Z2/Tepla	7min @ 600W					
4	**KOH Etching**							
4.1	KOH Etching	Z5/ Plade Six Sigma	40% KOH at 60°C	7.1um	25min	check exactly bath density: should be at 1.37		
4.2	FFR	Z5/ Plade Six Sigma				x 2		
4.3	Neutralization	Z5/ Plade Six Sigma	in HCl at room temperature	2h				
4.4	FFR	Z5/ Plade Six Sigma						
4.5	Nitrogen blow dry	Z5/ Plade Six Sigma						
4.6	Inspection	Z15/SEM				check tip sharpness!		
5	**SiN-LS removal**							
5.1	HF etching	Z2/ Plade Oxide	HF 4:1	20nm	1h	maybe 30min is enough; 1h removes 40nm as well		
5.2	FFR	Z2/ Plade Oxide				x 3		
5.3	SRD	Z2/ Plade Oxide				Spin-Rince-Dry		

6	**WetOx for tip sharpening and low-stress nitride deposition**					
6.1	RCA1 clean	Z3/WB_PreOx_Clean	H2O:NH4OH:H2O2 (5:1:1)	15min 75°C		CMi staff to perform
6.2	HF dip	Z3/WB_PreOx_Clean	HF:H2O (1:10)	15s		CMi staff to perform
6.3	RCA2 clean	Z3/WB_PreOx_Clean	H2O:HCl:H2O2 (6:1:1)	15min 75°C		CMi staff to perform
6.4	Fast fill rinse	Z3/WB_PreOx_Clean		15min		CMi staff to perform
6.5	Trickle tank	Z3/WB_PreOx_Clean		15min		CMi staff to perform
6.6	Spin rinser dryer	Z3/Semitool	Prog. 1			CMi staff to perform
6.7	Thermal oxidation	Z3/Centrotherm WOX	Wet oxide std process	400 nm		CMi staff to perform
6.8	Nitride deposition	Z3/Centrotherm LPCVD	Low stress nitride	20 nm		CMi staff to perform; deposit also 20nm
7	**Photolithography - "Backside registry" mask**					
7.1	Surface activation	Z2/Tepla GigaBatch	1min @ 200W O2 plasma			
7.2	Spin on	Z6/EVG150	AZ1512_2um_noEBR	2um		
7.3	Expose	Z6/MA6	Hard contact, CP mode	3.1s		Backside align. +0.1s for machine expose compensation
7.4	PR develop	Z6/EVG150	Dev_AZ1512_upto3um			!!! Clean backside with acetone!!!
8	**Oxide/nitride dry etch backside registry**					
8.1	Dry etch	Z2/SPTS	SiO2 PR 3:1	1min30s		To etch through oxide and nitride in one step
8.2	Inspection	Z2/microscope				
8.3	O2 plasma	Z2/Tepla GigaBatch	Strip high: 7 min @ 600W			
8.4	Remover 1165	Z2/UFT resist	5 min bath 1, 5 min bath 2, QDR, TT			
8.5	Spin rinser dryer	Z2/UFT resist	prog 1			
8.6	Inspection	Z2/microscope	Visual inspection for resist residue			
9	**BCB caoting and bondig**					
9.1	Surface activation	Z2/Tepla	10s @ 200W			alternative: dehydration for 5min @ 150°C
9.2	BCB primer coating	Z6/Wet bench	500rpm for 10s & 3000rpm for 30s (w/ N2)			BCB Primer AP3000; put 2ml & wait for 20s; N2 only after 3000rpm was reached
9.3	BCB coating	Z6/RC8 mid zone	700rpm for 9s & 4000rpm for 30s			700rpm w/ acc. 500rpm & 4000rpm w/ acc. 1000rpm
9.4	BCB pre-baking 1	Z6/RC8 entrance	80s @80°C			
9.5	BCB pre-baking 2	Z6/RC8 mid zone	20min@150°C			
9.6	Relaxation	in wafer box	1-2h minimum			
9.7	BCB bonding	Z6/SB6	prog LBNI-BCB bonding/manual bonding			align wafer flats by eye; first bond pyrex wafer with Si wafer to check for bonding uniformity
9.8	Relaxation	in wafer box	overnight			
9.9	BCB hard baking	Z2/Heraeus T6060	30min ramp to 250°C + 1h @250°C (+ down ramp to RT)		2h	
10	**Photolithography - "Chip release V4" mask - on bonded unprocessed SiN wafer**					
10.1	Surface activation	Z11/Tepla 300 or Z2/Tepla GigaBatch	Program 3 (300) or Strip high 1 min (GigaBatch)			
10.2	Spin on	Z13/SSE SB20	AZ1512HS, STD-4000-RPM	1.2 um		dispense resist over all wafer
10.3	PR bake	Z13/SSE SB20	100 °C on hotplate	1 min		
10.4	Expose	Z6/MA6	Hard contact, CP mode	2.4 s		for 10 mW/cm2 broadband

10.5	PR develop	Z13/Develop bench	MFCD26	40 sec		
10.6	DI Rinse	Z13/Develop bench	3 fill-exchanges			
10.7	N2 dry	Z13/Develop bench				
10.8	Inspection	Z13/microscope				Make sure backside of wafer is clean for next step. Clean with acetone if needed
11	**Dry etch - chip body openings**					
11.1	Nitride dry etch	Z2/SPTS	SiO2 PR 3:1	20 nm		Use EPD, long overetch is ok. 30s etch should be plenty long.
11.2	Inspection	Z2/microscope				
11.3	O2 plasma	Z2/Tepla GigaBatch	Strip high 7 min @ 600W			
11.4	Inspection	Z2/Visual	Visual inspection for resist residue			
12	**Dry etch opening on "tip" wafer side**					
12.1	Nitride dry etch	Z2/SPTS	SiO2 PR 3:1	20 nm		Use EPD, long overetch is ok. 30s etch should be plenty long. **No mask**
12.2	Inspection	Z2/Visual				
13	**KOH etching - Si bulk removal and membrane release**					
13.1	KOH Etching	Z5/ Plade Six Sigma	40%, 60°C, control density to 1.37 at 60°C	380 um		Check that bubbles start before leaving (~1 min delay). Overnight etch, takes approx 17.5 h
13.2	FFR	Z5/ Plade Six Sigma	3 fill-exchanges			
13.3	Neutralization	Z5/ Plade Six Sigma	HCL room temp	2h		
13.4	FFR	Z5/ Plade Six Sigma	3 fill-exchanges			Remove eventual off-pealing BCB parts at the wafer edge
13.5	Air dry	Z5/ Plade Six Sigma				Dry overnight, or at least a few hours
14	**HF etch of Wet oxide for tip release**					
14.1	HF etch	Z2/Plade oxide	BHF 7:1 WetOx etchrate:77nm/min	400nm	10min	5min15s for 400nm WetOx and massive overetch
14.2	Trickle tank	Z2/Plade oxide	3 fill-exchanges			
14.3	Air dry	Z2/Plade oxide				Dry overnight, or at least a few hours
15	**Aluminum deposition**					
15.1	Etch stop Al coating	Z11/EVA760	250 Al 160	2 um		back side (with chip bodies)
15.2	Hard mask Al coating	Z11/EVA760	450 Al 50 with uniformity handle	300nm		top side (with BCB)
16	**Photolithography - "Cantilever V2" mask - onto "tip" wafer side of trilayer membrane**					
16.1	Surface activation	Z13/SSE SB20	110 °C for 5 min on hotplate	5min		Or alternate thermal dehydration
16.2	Spin on	Z13/SSE SB20	AZ9260, STD-1200-RPM for 100s spin time & slow ramp	12 um		dispense resist over all chips on wafer
16.3	PR bake	Z13/SSE SB20	110 °C on hotplate	4 min		
16.4	Rehydration delay	Z13/wafer carrier	at least 1 h delay in ambient			
16.5	Expose	Z13/MJB4	Soft contact	3 x 10s		for 20 mW/cm^2 i-line. Split into 3, 10 second exposures with 10s waiting time
16.6	PR develop	Z13/Develop bench	AZ developer full conc.	4 min		slight agitation
16.7	DI Rinse	Z13/Develop bench	3 fill-exchanges			Careful with fragile membrane
16.8	air dry	Z13/Develop bench				Dry overnight, or at least a few hours
16.9	post bake	Z2/Heraeus T6060	baking at 145°C for 5min with moderate cool down	5min		should reinforce surface adhesion during aluminum wet etching
16.10	Inspection	Z13/microscope	Tip must be UNDER photoresist pattern			

Step	Process	Tool	Detail	Amount	Time	Notes
16.11	Inspection	Z15/SEM Merlin	Tip must NOT BE visible			at 0.5 kV or lower, else charging
17	**Aluminum wet etch and resist removal**					
17.1	Alu wet etch	Z2/Plade metal	ANP @ 35 °C	300 nm	1min15	Check visually until aluminum pattern is visible on frontside + overetch slightly (15s)!
17.2	Trickle tank	Z2/Plade metal	TrickleTank only	3 times		
17.3	Remover 1165	Z2/UFT resist	5 min bath 1, 5 min bath 2, Cascade rinsing (TT)		at 80°C	NO QRD
17.4	Trickle tank	Z2/UFT resist	ONLY cascade bath (Trickle Tank); NO QRD	2 times		
17.5	Air dry	Z2/UFT resist				Dry overnight, or at least a few hours
17.6	Inspection	Z15/SEM Merlin				
18	**Dry etch - sandwich etch for cantilever shape definition**					
18.1	nitride dry etch	Z2/STS	LBNI-BCB custom process	20 nm	10s	Use EPD, but signal difficult to see.
18.2	BCB dry etch	Z2/STS	LBNI-BCB custom process	4 um	8min	Using gases: 20sccm O2 & 10sccm CHF3
18.3	Nitride dry etch	Z2/STS	LBNI-BCB custom process	20 nm	10s	Might not be needed: remaining SiN-LS removed by BCB main etch process
19	**Aluminum wet etch**					
19.1	Alu wet etch	Z2/Plade metal	ANP @ 35 °C	2 um	8min	Check visually until all aluminum is gone!
19.2	Trickle tank	Z2/Plade metal	TrickleTank only	3 times		
19.3	Air dry	Z2/Plade metal				Dry overnight, or at least a few hours
20	**Metal reflective coating deposition**					
20.1	Ti/Au evap	Z11/DP650 Sputterer	RTU-Ti-Au	5 nm/20 nm	16s/16s	back side (with chip bodies); put on backing wafer with tape as spacer to protect tips
20.2	Inspection	Z15/SEM Merlin				

D Appendix: Focus group analysis

The focus group was done in the scope of the PhD course entitled *Qualitative Research Methods* given by Prof. Matthias Finger. The names of the participants of the focus group are not given in the text hereafter, in order to maintain their anonymity.

D.1 Focus group selection process and criteria

D.1.1 Criteria for participants

The participants for the focus group were carefully chosen according to their skills and knowledge in the desired research field [226]. The following three criteria were applied to the participants during the selection process:

1. The participant should use the atomic force microscope (AFM) in his research or should have a thorough knowledge about the technology

2. The participant should be knowledgeable in microbiology and conduct experiments on bacteria, or eukaryotic cells as a function of interaction with bacteria.

3. The participants would ideally use a microfluidic device for the experiments

The last requirement is usually automatically fulfilled when the participant fits the first two requirements and does research in an aqueous environment, which is mandatory in order to conduct experiments on living cells.

The participants present in this focus group study originate from three different laboratories at EPFL. All laboratories focus partially on AFM research in combination with bacteria,

albeit different bacteria are examined and different approaches towards the analysis are made. All participants were thoroughly examined to meet the set criteria for the focus group.

D.1.2 Incentives

In order to compensate the participants for their contribution to the focus group, food and drinks were provided. This approach was chosen in order to accommodate the participants in the best way, as well as to set a friendly atmosphere for the discussion.

D.2 Focus group outline and discussion topics

D.2.1 Introduction and visual presentation

At the beginning of the focus group, the participants were averted that the whole discussion was recorded. Total anonymity was confirmed and the goal of the focus group was explained to the participants.

The introduction of the focus group continued by every participant presenting him-/herself to the group. Thereafter, a visual presentation of the project was given consisting of three technical slides explaining the purpose, device design, and experiment setup.

D.2.2 Needs and requirements for the microfluidic device and setup

In the beginning, the goal is to get familiar with the participants approach to experiments with AFM and microfluidic devices for analysis of bacteria. The opening question was therefore:

- "First, I'd like to hear in which way you've been involved with AFM experiments and/or experiment with microfluidic devices handling bacteria. In what way were these analysis methods and tools helpful to you?"

The follow up questions was made to understand the participant's behavior during experiment preparations and the analysis with the used tools. We anticipate from our knowledge already that the AFM tip choice or AFM tip functionalization and in particular sample preparation are known to be the most critical parts for AFM users, as reported extensively in literature.

- "What was the most critical part in the experiment setup?"

Once the participants were accustomed amongst each other to the different point of views and approaches to experiments, the following set of questions were prepared in order to get an analysis of the requirements for a newly developed microfluidic device. The participants are meant to take the role of potential customers and share their needs towards new technology, which some of them develop as well by themselves. The goal is to understand the participants weighing of the different aspects, such as ease-of-use, complexity, robustness, and reusability of the device, as well as their safety concerns, when the device is used in combination with experiments on pathogens.

- "For you, what are the critical aspects for handling a newly developed microfluidic device?"

- "When analyzing bacteria with a microfluidic device, what would be the main requirements?"

- "How important is the reusability of a microfluidic device to you?"

- "Of all the things discussed, what to you is the most important?"

This concludes the analysis of the participant regarding a novel microfluidic device. The participants, each one of them an expert in their field, should give valuable insight from their point of view as a researcher and give specific requirements to the developed device. The first part of the focus group is thus a market analysis of the developed microfluidic device.

Research topics on single cell level

This topic is intended to get the perception from the point of view of the participants, in what way the presented device can be used. Hot topics, such as the morphological changes on the bacterial envelope, are expected to be mentioned. Nevertheless, more interesting research topics should be mentioned, since the participants do know the possibilities, but as well the limitations of the presented techniques and the used equipment. The following two questions will be discussed for this intent:

- "Which phenomena would you investigate if provided with technology?"

- "Would you see another domain, where the presented device would be helpful?"

No clues on already concluded research with the developed device was given to the participant prior to the discussion; only a brief mentioning that trapping and analysis of bacteria is possible on a repeatable basis.

AFM in microbiology and microfluidic devices

The focus group study is concluded with the following two questions:

- "How useful would you judge the atomic force microscope?"

- "What needs improvement?"

The participants are expected to give their honest opinion about the AFM technology in general. Since some participants have a strong biology background and others an engineering background, the opinions and views in this particular discussion topic are expected to differ the most amongst the participants.

D.3 Outcome and analysis

D.3.1 Needs and requirements for the microfluidic device and setup

From the points of view of the present participants, each an expert in his field, multiple requirements towards the presented microfluidic device were established. First, the needs of the participants according to their own projects were analyzed and thereafter, the participants were questioned as potential customers for the presented device.

The general requirement for bacterial or mammalian cell analysis is the confinement of the cell. The fluidic device is either closed or open, according to the needs of the experiment. For AFM analysis, an open fluidic setup eases the sample preparation and experiment setup time. Nevertheless, participants reported closed microfluidic setups, where the AFM cantilever is enclosed with bacteria. For this, bacteria were attached to the cantilever and assembled within the microfluidic device. The fluidic device was closed and sealed thereafter and the cantilever deflections were read out by a laser through a transparent layer.

For another microfluidic setup, cells were put through a droplet into a microfluidic chamber that was closed thereafter. Through a semi-permeable layer, nutrients could be delivered to the chamber. Other participant use simple glass slides coated with poly-dimethysiloxane (PDMS), a commonly used material in bioengineering. The PDMS allows

the sticking of the bacterium *Mycobacterium smegmatis* onto the surface and provides enough stability for AFM measurements; this technique is mostly limited to this bacterial species thought.

With our presented fluidic device, bacteria are as well in a physiological medium. Below the bacteria, underneath the membrane with the traps, a physiological buffer is as well present; the delivery of nutrients or other aqueous media is possible from the bottom side. From the top side, the buffer needs to be exchanged manually through pipettes. This can be achieved as well during an experiment, while bacteria are being analyzed, supposing a careful handling of the user.

Nutrients can be delivered to the cells through a semi-transparent membrane, which is assembled with the microfluidic device, as aforementioned. Other methods use fluid exchange through channels assembled with the fluidic device, in a continuous way or when the experiment is paused.

One principal demand for fluidic devices is the transparency of the device. If the fluidic device is a closed environment, at least one side of the device needs to be fully transparent, in order to allow phase microscopy, fluorescence microscopy, or cantilever deflection read-out through a laser beam. A fluidic device used by participant that is intended for simultaneous fluorescence and atomic force microscopy, is exposed to the environment from the top side and transparent on the bottom side. Since our presented device contains both, an enclosed part underneath the membrane, and as well the top part that is open to the environment, both requirements apply. Therefore, the actual concept is judged as promising by the participants, since the bacteria can be analyzed by the AFM from the top side, and from the bottom side, fluorescence microscopy can be done simultaneously.

Participants interested in cell growth and antibiotic resistance analysis of the cell express the desire to be able to analyze the bacterium during multiple buffer exchanges, in order to test various antibiotics and the response of the bacterium. Moreover, physical space must be present, not only for the growth of the cell, but as well for eventual bulging of the bacterium as a result of increase in turgor pressure due to antibiotic treatment. Neverthe-less, the experiments should allow the extraction of the stiffness of the bacterium. This is possible through various techniques and is routinely done in our laboratory [227] and by others [228, 229]; direct extraction of the data can nowadays be done by Bruker's Peak-Force Qantitative Mechanical Mapping (PF-QNM) [187] supposing a correct calibration of the AFM tip [19, 99, 187].

A requirement discovered as a strong need by the participants is the ability to heat and

maintain the fluidic device at a certain temperature, at which the bacteria can optimally grow. Such a temperature control has temporarily been implemented into the current device, but discarded after several experiments. The strong need for this feature expressed by the participants concluded that the future models of the fluidic device and its holding frame should have the ability to heat up the aqueous environment and monitor the temperature of the present liquid medium.

A topic vividly discussed is the ease-of-use of fluidic devices. Every participant has its own approach to sample preparation. Moreover, due to the diversity of the experiments, no common technique can be established. The ease-of-use for a novel device was well described by one of the participants: "The final user should not spend a huge amount of time figuring out how the device works. If it's not an intuitive way, a how-to guide should be provided. Also, no specific laboratory equipment should be needed, but the operation should work with standard laboratory tools." For now, the device assembly is quite specific and necessitates skilled craftsmanship in order to have a correct assembly of the fluidic chip. The assembly embedding into the holder frame is a straight forward approach. Standard connectors allow for simple connections to fluid or pressure controllers. On the other hand, AFM analysis necessitates a skilled operator with experience in imaging of soft samples or optimally, bacteria.

Temporal stability of a used microfluidic device is perceived differently by participants. Where some experiments last roughly two hours, others can last for several days. Participants were conducting experiments even over two to three weeks in a regular manner. The stability of the device must be provided over the period of the user's experiments. The current experiments on the device were up to 24 hours, whereas the continuous imaging on one trapped bacterium was done over 6 hours in a stable and robust manner. The trapped bacterium remained confined and the AFM imaging was stable over the whole experiment time. Further investigations with experiments over several days or weeks should be conducted in order to determine the long-term stability of our presented fluidic device.

From the point of view as a final product, the participants judge that the microfluidic assembly should definitely not be provided in parts, but already as a final device assembly, even if the price tag is higher. The discussion didn't result in a consensus for this topic, but there were rather two distinct opinions. The price should be seen as a function of reusability. A high price indicates the participants that they should reuse the device, where for a low price they are willing to dispose it. As a participant stated: "The best would be something very cheap and disposable. The second best would be something expensive, but that you can wash easily. Afterwards it's a compromise."

Nevertheless, some participants issued concerns about the reusability, since the microfluidic device is used together with bacteria and for thorough cleaning, the device must be sterilized by autoclaving for any further use. At this point of development, the device needs to be disassembled and washed, which alone takes a certain amount of time, since hazardous chemistry is used for the thorough cleaning of the chip. The fluidic chip assembly is immersed overnight in acetone and all the reusable parts are cleaned with a piranha solution, consisting of a mixture of sulfuric acid and hydrogen peroxide. Only thereafter a re-assembly can be done. Participants issued that the proposed fluidic device should be autoclaved before use, but other participants argue that when they fabricate and assemble their fluidic devices in the cleanroom, they skip the autoclave step and never had any issues with contamination in the past years of their experiments.

As for the design of the traps, the participants expressed a desire to have more traps on a membrane. Currently a fluidic chip contains up to 15 traps for a specific width of bacteria. By adding more traps per chip, the users would be able to detect and select a bacterium of interest with fluorescence microscopy and analyze it thereafter with AFM. Furthermore, on a chip there should be tarps with various widths and lengths for bacteria; even though the analyzed bacteria originate from one single colony, the overall dimensions can differ. The length of the bacterium is a function of the state of growth of a bacterium and even widths of bacteria can vary slightly from one colony to the other of the exact same species of a bacterium, as seen throughout the conducted experiments with the presented device.

One critical aspect about the presented device is that once a bacterium is immobilized inside the trap, the correct height cannot be determined. Moreover, due to the design of the microfluidic device, the traps are not in proximity to the objective and a microscope objective with a high working distance must be used. Furthermore, some participants express their desire to add continuous flow to the microfluidic device setup, to not be dependent to the user's pipetting skills.

To sum up, through the focus group, various requirements for the next iteration in the development of the microfluidic device were established. Amongst the requirements that the current microfluidic device fulfills are reliable confinement of cells in an aqueous environment and the possibility of fluid exchange by adding nutrients or other user-selected buffers. Moreover, the device allows fluorescence microscopy from the back side, while AFM analysis can be done simultaneously. By modifying the dimensions of the traps, bacteria with various dimensions could be analyzed. The ease-of-use should be optimized for a smooth end-user experience, or the assembly method should be changed in order to allow an easy user-based assembly of the microfluidic device. Furthermore, a temperature control should be implemented in the fluidic chip holder frame, as expressed by the focus

group participants. More investigations should be focused into the robustness over longer periods of time for experiments lasting several days up to several weeks.

D.3.2 Research topics on single cell level

The presented device can as well be used for other promising experiments. The focus group elucidated possible future experiment in areas beyond the initially intended aim.

Based on current project of some participants, first suggestions were the observation of bacterial growth inside the traps and the DNA distribution inside the cell. The growth would be observed by AFM from the top side of the microfluidic device and using fluorescence microscopy from the bottom side of the device, the DNA distribution would be visible as a function of local fluorescent intensity inside the bacterium.

Participants would as well use the fluidic device in order to confirm their initial experiment. In particular, when they use a coated substrate like a PDMS coated cover slip, the exact interaction between the coating and the bacterium remains obscure and the exact influence of the coating remains unknown. By using a chemically inert surface, all chemical interactions between the substrate and the bacterium can be excluded. By repeating the experiments, their recent findings could therefore be confirmed.

Without having mentioned any conducted experiments with the device, one focus group participant proposed that antibiotic effects could be observed on the bacterial envelope in combination with the fluorescence signal, by notably mentioning beta-lactam antibiotics. Beta-lactam antibiotics are responsible for a malfunctioning of the bacterial envelope synthesis during the growth of the bacterium, which leads to the death of the bacterium [230]. Nevertheless, up to that moment, experiments were conducted using a specific antibiotic compound named CM15 belonging to the class of antimicrobial peptides, which was used to induce the killing of bacteria. This antimicrobial peptide is knows to create pores in the bacterial envelope and thus induce an imminent roughening of the bacterial envelope [13, 132]. Experiments were made with the microfluidic device in order to observe simultaneously the killing of the bacterium by AFM and fluorescence microscopy using fluorescent dies indicating the bacterial vitality. Moreover, these experiments were conducted in physiological buffer solution.

These experiments could be extended to test antibiotics in a sequential manner. The possibility to trap, release, and to trap the bacteria again, opens the opportunity to examine a multitude of bacteria in one experiment. Furthermore, a trapped bacterium could as well be exposed to various buffers containing different antibiotics or different concentrations of one antibiotic.

A very interesting suggestion by a participant would be the analysis of bacterial killing behavior during bacterial cell-cell interaction. Using the bacterial secretion system, the bacterium *Pseudomonas aeruginosa* is able to inject through an organelle an effector protein into an adjacent bacterium, thus killing the bacterium [231]. By trapping two cells in predefined places, this mechanism could be elucidated in detail by the AFM with a higher special resolution, and the process could be monitored simultaneously through fluorescent microscopy.

The use of the microfluidic device must not be confined to only bacterial analysis. Participants suggested to observe neurons, in particular the synaptic contact formation. Pioneering work was done on neurons by using AFM for imaging of the topography and as well the stiffness mapping [232], but with our presented device, the sample preparation would be facilitated and no chemical modification of the surface would influence the measurements. We could elucidate with a high special and temporal resolution the process of formation of synapses and investigate thoroughly which phenomena are involved.

Another very interesting investigative pathway could be to include the potential of optical tweezers into the whole system [233]. This would include another degree of complexity and the experiment setup would have to be modified. Nevertheless, this method would allow the exact selection of a bacterium of particular interest, which would have been previously identified by the already implemented methods, followed by a cultivation of the identified bacterium of interest.

During the focus group discussion concerning this topic, more interesting ideas were given. Amongst them would be the analysis of molecular motors and their specific binding process, as it has been shown in recent publications [14]. Or the confinement of DNA or nanoparticles for analysis without any chemical modification of the substrate. For these experiments, the trap dimensions would have to be significantly altered and a thorough microfluidic analysis would have to be done prior to any microfabrication processing.

In summary, the principal intended use can be extended to a large range of application. Focusing on its primary use though, a myriad of experiments can be conducted by only studying microbial or mammalian cells, which do not adhere to a chemically inert substrate. Mobile bacteria or cancerous blood cells could for example be immobilized in the traps and their envelope morphology or mechanical properties could be elucidated.

D.3.3 AFM in microbiology and microfluidic devices

"The AFM for biology is great", citing a member of the focus group. It would be the only tool to their knowledge that allows accurate measurements of the bacterial cell size, volume

and stiffness. Different data can be obtain in respect to fluorescence microscopy, and by combining an AFM with a fluorescence microscope, even more microbial phenomena can be investigated by correlating the obtained datasets.

With the AFM, the bacterial envelope can be accurately analyzed. The envelope is the boundary between the cell and the environment, and at this boundary the interactions happen. To elucidate phenomena at the bacterial envelope could provide us with more insights when we correlate the data with cell internal events by using specific fluorescent tags. Hitherto, studies are based only on bacterial size and how they grow. By adding topography and mechanical property datasets, the participants are certain that more information will be extractable.

Nevertheless, the AFM is perceived as a complementary tool by the present experts in microbiology. This is mainly due to the difficulty for using it. As a participant stated: "If the AFM would be easier to use, it would have much more impact in biology." The principal investigation tool remains the optical microscopy in combination with either fluorescence or various other extension modes, such as phase microscopy.

Specialized laboratories for AFM exist in order to train experienced users, whereas biological investigations with the AFM remain a coproduct. A perceived disadvantage is that compared to other techniques, the AFM only allows accurate measurements of one cell or frame at a time, on a timescale perceived as very long. Moreover, the participants judge that the AFM is still a tool, where it's considered as normal to stay and monitor the experiment overnight.

Sample preparation remains still one of the most important parts in AFM analysis, where the user is obliged to be knowledgeable about the AFM technique and know its limitations, in order to maximize the usable experiment data output. All participants of the focus group have their own microfluidic devices and modified components for the AFM analysis; a critique is that the lack of standardization between the atomic force microscopes of different manufacturers. It is common to manufacture a custom fluidic cell in order to be compatible between different AFMs or the laboratory focuses only on one brand of AFMs.

After all, participants agree that the most enjoyable memories regarding their past research moments are experiments that could be concluded as planned. Even though no further insights in respect to biological know-how could be generated, the experiment is a success when all components of the setup didn't break down and functioned as planned. This shows the state of development: single investigative tool can work flawlessly on their own, but today researchers combine multiple techniques together for simultaneous analysis.

The flawless functioning of all parts of the setup is important in order to gain further insight into unanswered questions in microbiology. Moreover, sample preparation will remain specific for each research subject, and robust and reproducible sample preparation is essential for every AFM analysis.

D.3.4 General observations during focus group discussion

Through the analysis of the focus group, valuable insight into user experience with the manipulation of microfluidic devices was gained. Moreover, due to the presence of AFM users with experiences regarding daily routines and weak points of the used technology, different aspects were elucidated from multiples points of views.

The focus group participants shared their needs for microfluidic devices and elucidated the critical aspect, when AFM, microfluidic, and optical microscopy is combined in order to investigate microbiological phenomena. Moreover, potential future topics of investigation were discussed by using the presented microfluidic device.

D.4 Conclusion on the focus group analysis

The focus group was the ideal solution to get insight from participants, each one being an expert in their domain. The focus group was also used as a market analysis tool; participants were asked, what their requirements towards a novel microfluidic device with the indicated purpose would be. Moreover, valuable insight was gained in respect to potential areas of application of the device, which were initially never planned.

During the focus group, a lot of question were asked to the facilitator. The questions were typically very specific and the participants were eager to know more about the technology. The questions could have been answered at the very beginning during the presentation of the device, but the presentation was intended to be as brief as possible in order to not overwhelm the participants at the beginning with technical details. Therefore the facilitator was obliged to answer the open questions, but as brief as possible in order to keep the conversation between the participants. Moreover, an equal sharing of insights requires an equal speaking time for the participants; the facilitator specifically targeted people, who remained quiet for a longer period, with direct questions. Overall, the focus group remained a vivid discussion about the given topics and all intended topics were discussed.

Bibliography

[1] E. Abbe, "Beiträge zur Theorie des Mikroskops und der mikroskopischen Wahrnehmung," *Archiv für Mikroskopische Anatomie*, vol. 9, no. 1, pp. 413–418, 1873.

[2] S. Kawata, Y. Inouye, and P. Verma, "Plasmonics for near-field nano-imaging and superlensing," *Nature Photonics*, vol. 3, pp. 388–394, 2009.

[3] S. W. Hell, "Microscopy and its focal switch," *Nature Methods*, vol. 6, pp. 24–32, 2009.

[4] F. Balzarotti, Y. Eilers, K. C. Gwosch, A. H. Gynnå, V. Westphal, F. D. Stefani, J. Elf, and S. W. Hell, "Nanometer resolution imaging and tracking of fluorescent molecules with minimal photon fluxes," *Science*, vol. 355, pp. 606–612, 2017.

[5] J. G. Tappert, "An Experimental Investigation of de Broglie's Equation," *Physical Review*, vol. 54, pp. 1085–1088, 1938.

[6] E. Ruska, "The Development of the Electron Microscope and of Electron Microscopy (Nobel Lecture)," *Angewandte Chemie International Edition in English*, vol. 26, pp. 595–605, 1987.

[7] N. de Jonge and F. M. Ross, "Electron microscopy of specimens in liquid," *Nature Nanotechnology*, vol. 6, pp. 695–704, 2011.

[8] G. Binnig, C. C. F. Quate, and C. Gerber, "Atomic Force Microscope," *Physical Review Letters*, vol. 56, no. 9, pp. 930–933, 1986.

[9] G. Binnig, H. Rohrer, C. Gerber, and E. Weibel, "Tunneling through a controllable vacuum gap," *Applied Physics Letters*, vol. 40, pp. 178–180, 1982.

[10] C. Gerber and H. P. Lang, "How the doors to the nanoworld were opened," *Nature Nanotechnology*, vol. 1, pp. 3–5, 2006.

[11] G. Binnig, H. Rohrer, C. Gerber, and E. Weibel, "7 × 7 Reconstruction on Si(111) Resolved in Real Space," *Physical Review Letters*, vol. 50, pp. 120–123, 1983.

[12] B. Drake, D. S. Cannell, H. G. Hansma, and P. K. Hansma, "Imaging Crystals, Polymers, and Processes in Water with the Atomic Force Microscope," *Science*, vol. 243, no. 4898, pp. 1586–1589, 1989.

[13] G. E. Fantner, R. J. Barbero, D. S. Gray, and A. M. Belcher, "Kinetics of antimicrobial peptide activity measured on individual bacterial cells using high-speed atomic force microscopy," *Nature Nanotechnology*, vol. 5, pp. 280–285, 2010.

[14] N. Kodera, D. Yamamoto, R. Ishikawa, and T. Ando, "Video imaging of walking myosin V by high-speed atomic force microscopy," *Nature*, vol. 468, pp. 72–76, 2010.

[15] G. Kada, F. Kienberger, and P. Hinterdorfer, "Atomic force microscopy in bionanotechnology," *Nano Today*, vol. 3, pp. 12–19, 2008.

Bibliography

[16] Y. F. Dufrêne, T. Ando, R. Garcia, D. Alsteens, D. Martinez-martin, A. Engel, C. Gerber, and D. J. Müller, "Imaging modes of atomic force microscopy for application in molecular and cell biology," *Nature Nanotechnology*, vol. 12, no. 4, pp. 295–307, 2017.

[17] P. D. Odermatt, A. Shivanandan, H. Deschout, R. Jankele, A. P. Nievergelt, L. Feletti, M. W. Davidson, A. Radenovic, and G. E. Fantner, "High-Resolution Correlative Microscopy: Bridging the Gap between Single Molecule Localization Microscopy and Atomic Force Microscopy," *Nano Letters*, vol. 15, pp. 4896–4904, 2015.

[18] G. Pharr and W. Oliver, "Measurement of Thin Film Mechanical Properties Using Nanoindentation," *MRS Bulletin*, vol. 17, pp. 28–33, 1992.

[19] J. L. Hutter and J. Bechhoefer, "Calibration of atomic-force microscope tips," *Review of Scientific Instruments*, vol. 64, no. 7, pp. 1868–1873, 1993.

[20] J. Sader and I. Larson, "Method for the calibration of atomic force microscope cantilevers," *Review of Scientific Instruments*, vol. 66, no. July, pp. 3789–3798, 1995.

[21] N. A. Burnham, X. Chen, C. S. Hodges, G. A. Matei, E. J. Thoreson, C. J. Roberts, M. C. Davies, and S. J. B. Tendler, "Comparison of calibration methods for atomic-force microscopy cantilevers," *Nanotechnology*, vol. 14, pp. 1–6, 2003.

[22] H. Hertz, "Ueber die Berührung fester elastischer Körper," *Journal für die reine und angewandte Mathematik*, vol. 92, no. February, pp. 156–171, 1882.

[23] K. L. Johnson, K. Kendall, and A. D. Roberts, "Surface Energy and the Contact of Elastic Solids," *Proceedings of the Royal Society A: Mathematical, Physical and Engineering Sciences*, vol. 324, pp. 301–313, 1971.

[24] B. Derjaguin, V. Muller, and Y. Toporov, "Effect of contact deformations on the adhesion of particles," *Journal of Colloid and Interface Science*, vol. 53, pp. 314–326, 1975.

[25] D. Tabor, "Surface forces and surface interactions," *Journal of Colloid and Interface Science*, vol. 58, pp. 2–13, 1977.

[26] I. Sneddon, "The relation between load and penetration in the axisymmetric boussinesq problem for a punch of arbitrary profile," *Int. J. Engng Sci.*, vol. 3, no. 638, pp. 47–57, 1965.

[27] I. Sokolov, S. Iyer, V. Subba-Rao, R. M. Gaikwad, and C. D. Woodworth, "Detection of surface brush on biological cells in vitro with atomic force microscopy," *Applied Physics Letters*, vol. 91, pp. 1–3, 2007.

[28] H. Wang, J. J. Wilksch, T. Lithgow, R. a. Strugnell, and M. L. Gee, "Nanomechanics measurements of live bacteria reveal a mechanism for bacterial cell protection: the polysaccharide capsule in Klebsiella is a responsive polymer hydrogel that adapts to osmotic stress," *Soft Matter*, vol. 9, no. 31, pp. 7560–7567, 2013.

[29] N. Guz, M. Dokukin, V. Kalaparthi, and I. Sokolov, "If Cell Mechanics Can Be Described by Elastic Modulus: Study of Different Models and Probes Used in Indentation Experiments," *Biophysical Journal*, vol. 107, pp. 564–575, 2014.

[30] H. C. Berg, "The Rotary Motor of Bacterial Flagella," *Annual Review of Biochemistry*, vol. 72, no. 1, pp. 19–54, 2003.

[31] E. Lauga and T. R. Powers, "The hydrodynamics of swimming microorganisms," *Reports on Progress in Physics*, vol. 72, pp. 1–36, 2009.

[32] T. J. Beveridge and L. L. Graham, "Surface layers of bacteria," *Microbiological reviews*, vol. 55, pp. 684–705, 1991.

[33] H.-J. Butt, E. Wolff, S. Gould, B. Dixon Northern, C. Peterson, and P. Hansma, "Imaging cells with the atomic force microscope," *Journal of Structural Biology*, vol. 105, pp. 54–61, 1990.

[34] D. Pum and U. Sleytr, "Monomolecular reassembly of a crystalline bacterial cell surface layer (S-layer) on untreated and modified silicon surfaces," *Supramolecular Science*, vol. 2, no. 1995, pp. 193–197, 1995.

[35] F. Schabert, C. Henn, and A. Engel, "Native Escherichia coli OmpF porin surfaces probed by atomic force microscopy," *Science*, vol. 268, pp. 92–94, 1995.

[36] A. Beaussart, A. E. Baker, S. L. Kuchma, S. El-Kirat-Chatel, G. A. O'Toole, and Y. F. Dufrêne, "Nanoscale Adhesion Forces of Pseudomonas aeruginosa Type IV Pili," *ACS Nano*, vol. 8, pp. 10723–10733, 2014.

[37] E. J. Hayhurst, L. Kailas, J. K. Hobbs, and S. J. Foster, "Cell wall peptidoglycan architecture in Bacillus subtilis," *Proceedings of the National Academy of Sciences*, vol. 105, pp. 14603–14608, 2008.

[38] T. Ando, T. Uchihashi, and S. Scheuring, "Filming Biomolecular Processes by High-Speed Atomic Force Microscopy," *Chemical Reviews*, vol. 114, pp. 3120–3188, 2014.

[39] Y. F. Dufrêne, D. Martínez-Martín, I. Medalsy, D. Alsteens, and D. J. Müller, "Multiparametric imaging of biological systems by force-distance curve-based AFM," *Nature methods*, vol. 10, no. 9, pp. 847–854, 2013.

[40] Y. F. Dufrêne, "Using nanotechniques to explore microbial surfaces," *Nature Reviews Microbiology*, vol. 2, pp. 451–460, 2004.

[41] M. Radmacher, R. W. Tillmann, M. Fritz, and H. E. Gaub, "From molecules to cells: imaging soft samples with the atomic force microscope," *Science*, vol. 257, pp. 1900–1905, 1992.

[42] S. Karrasch, M. Dolder, F. Schabert, J. Ramsden, and A. Engel, "Covalent binding of biological samples to solid supports for scanning probe microscopy in buffer solution," *Biophysical Journal*, vol. 65, pp. 2437–2446, 1993.

[43] S. Kasas and A. Ikai, "A method for anchoring round shaped cells for atomic force microscope imaging," *Biophysical Journal*, vol. 68, pp. 1678–1680, 1995.

[44] A. Razatos, Y. L. Ong, M. M. Sharma, and G. Georgiou, "Molecular determinants of bacterial adhesion monitored by atomic force microscopy," *Proceedings of the National Academy of Sciences of the United States of America*, vol. 95, pp. 11059–11064, 1998.

[45] R. L. Meyer, X. Zhou, L. Tang, A. Arpanaei, P. Kingshott, and F. Besenbacher, "Immobilisation of living bacteria for AFM imaging under physiological conditions," *Ultramicroscopy*, vol. 110, pp. 1349–1357, 2010.

[46] Y. Liu, J. Strauss, and T. A. Camesano, "Adhesion forces between Staphylococcus epidermidis and surfaces bearing self-assembled monolayers in the presence of model proteins," *Biomaterials*, vol. 29, pp. 4374–4382, 2008.

[47] V. Vadillo-Rodríguez, H. J. Busscher, H. C. Van Der Mei, J. De Vries, and W. Norde, "Role of lactobacillus cell surface hydrophobicity as probed by AFM in adhesion to surfaces at low and high ionic strength," *Colloids and Surfaces B: Biointerfaces*, vol. 41, no. 1, pp. 33–41, 2005.

[48] T. Zhang, Y. Chao, K. Shih, X.-Y. Li, and H. H. Fang, "Quantification of the lateral detachment force for bacterial cells using atomic force microscope and centrifugation," *Ultramicroscopy*, vol. 111, pp. 131–139, 2011.

[49] Y. F. Dufrêne, "Atomic force microscopy and chemical force microscopy of microbial cells," *Nature Protocols*, vol. 3, pp. 1132–1138, 2008.

117

Bibliography

[50] Y. Liu and T. A. Camesano, "Immobilizing Bacteria for Atomic Force Microscopy Imaging or Force Measurements in Liquids," in *Microbial Surfaces: Structure, Interactions and Reactivity (ACS Symposium Series)*, vol. 984, ch. 10, pp. 163–188, American Chemical Society, 2008.

[51] M. Doktycz, C. Sullivan, P. Hoyt, D. Pelletier, S. Wu, and D. Allison, "AFM imaging of bacteria in liquid media immobilized on gelatin coated mica surfaces," *Ultramicroscopy*, vol. 97, pp. 209–216, 2003.

[52] M. Obst and M. Dittrich, "Living under an atomic force microscope," *Geobiology*, vol. 3, pp. 179–193, 2005.

[53] D. P. Allison, C. J. Sullivan, N. P. Mortensen, S. T. Retterer, and M. Doktycz, "Bacterial Immobilization for Imaging by Atomic Force Microscopy," *Journal of Visualized Experiments*, pp. 5–7, 2011.

[54] A. E. Pelling, Y. Li, W. Shi, and J. K. Gimzewski, "Nanoscale visualization and characterization of Myxococcus xanthus cells with atomic force microscopy," *Proceedings of the National Academy of Sciences*, vol. 102, pp. 6484–6489, 2005.

[55] N. Read, S. Connell, and D. G. Adams, "Nanoscale visualization of a fibrillar array in the cell wall of filamentous cyanobacteria and its implications for gliding motility," *Journal of Bacteriology*, vol. 189, no. 20, pp. 7361–7366, 2007.

[56] K. Colville, N. Tompkins, A. D. Rutenberg, and M. H. Jericho, "Effects of Poly(L-lysine) Substrates on Attached Escherichia coli Bacteria," *Langmuir*, vol. 26, pp. 2639–2644, 2010.

[57] B. Y. Liu, G. M. Zhang, X. L. Li, and H. Chen, "Effect of glutaraldehyde fixation on bacterial cells observed by atomic force microscopy.," *Scanning*, vol. 34, no. 1, pp. 6–11, 2012.

[58] V. Vadillo-Rodriguez, H. J. Busscher, W. Norde, J. de Vries, R. J. B. Dijkstra, I. Stokroos, and H. C. van der Mei, "Comparison of Atomic Force Microscopy Interaction Forces between Bacteria and Silicon Nitride Substrata for Three Commonly Used Immobilization Methods," *Applied and Environmental Microbiology*, vol. 70, pp. 5441–5446, 2004.

[59] H. C. van der Mei, H. J. Busscher, R. Bos, J. de Vries, C. J. Boonaert, and Y. F. Dufrêne, "Direct Probing by Atomic Force Microscopy of the Cell Surface Softness of a Fibrillated and Nonfibrillated Oral Streptococcal Strain," *Biophysical Journal*, vol. 78, pp. 2668–2674, 2000.

[60] R. Turner, N. Thomson, J. Kirkham, and D. Devine, "Improvement of the pore trapping method to immobilize vital coccoid bacteria for high-resolution AFM: a study of Staphylococcus aureus," *Journal of Microscopy*, vol. 238, pp. 102–110, 2010.

[61] L. Kailas, E. C. Ratcliffe, E. J. Hayhurst, M. G. Walker, S. J. Foster, and J. K. Hobbs, "Immobilizing live bacteria for AFM imaging of cellular processes," *Ultramicroscopy*, vol. 109, pp. 775–780, 2009.

[62] P. Chen, L. Xu, J. Liu, F. J. H. Hol, J. E. Keymer, F. Taddei, D. Han, and A. B. Lindner, "Nanoscale Probing the Kinetics of Oriented Bacterial Cell Growth Using Atomic Force Microscopy," *Small*, vol. 10, pp. 3018–3025, 2014.

[63] K. J. Regehr, M. Domenech, J. T. Koepsel, K. C. Carver, S. J. Ellison-Zelski, W. L. Murphy, L. A. Schuler, E. T. Alarid, and D. J. Beebe, "Biological implications of polydimethylsiloxane-based microfluidic cell culture," *Lab on a Chip*, vol. 9, no. 15, pp. 2132–2139, 2009.

[64] O. Peric, M. Hannebelle, J. D. Adams, and G. E. Fantner, "Microfluidic bacterial traps for simultaneous fluorescence and atomic force microscopy," *Nano Research*, vol. 10, pp. 3896–3908, 2017.

[65] D. Mijatovic, J. C. T. Eijkel, and A. van den Berg, "Technologies for nanofluidic systems: top-down vs. bottom-up—a review," *Lab on a Chip*, vol. 5, no. 5, p. 492, 2005.

118

[66] G. M. Whitesides, "The 'right' size in nanobiotechnology," *Nature Biotechnology*, vol. 21, pp. 1161–1165, 2003.

[67] K. R. Williams and R. S. Muller, "Etch Rates for Micromachining Processing," *Journal of Microelectromechanical Systems*, vol. 5, no. 4, pp. 256–269, 1996.

[68] W. Fan and D. Zhang, "A simple approach to convex corner compensation in anisotropic KOH etching on a (100) silicon wafer," *Journal of Micromechanics and Microengineering*, vol. 16, pp. 1951–1957, 2006.

[69] R. M. Finne and D. L. Klein, "A Water-Amine-Complexing Agent System for Etching Silicon," *Journal of The Electrochemical Society*, vol. 114, no. 9, pp. 965–970, 1967.

[70] A. Hölke and H. Thurman Henderson, "Ultra-deep anisotropic etching of (110) silicon," *Journal of Micromechanics and Microengineering*, vol. 9, pp. 51–57, 1999.

[71] D. L. Kendall, "A new theory for the anisotropic etching of silicon and some underdeveloped chemical micromachining concepts," *Journal of Vacuum Science & Technology A: Vacuum, Surfaces, and Films*, vol. 8, pp. 3598–3605, 1990.

[72] H. Seidel, L. Csepregi, A. Heuberger, and H. Baumgärtel, "Anisotropic Etching of Crystalline Silicon in Alkaline Solutions," *Journal of The Electrochemical Society*, vol. 137, no. 11, pp. 3612–3626, 1990.

[73] Z. Zhu and C. Liu, "Anisotropic crystalline etching simulation using a continuous cellular automata algorithm," *CMES - Computer Modeling in Engineering and Sciences*, vol. 1, no. 1, pp. 11–19, 2000.

[74] R. Haken, I. Baker, and J. Beynon, "An investigation into the dependence of the chemically-etched edge profiles of silicon dioxide films on etchant concentration and temperature," *Thin Solid Films*, vol. 18, pp. S3–S6, 1973.

[75] H. J. Mamin and D. Rugar, "Thermomechanical writing with an atomic force microscope tip," *Applied Physics Letters*, vol. 61, no. 8, pp. 1003–1005, 1992.

[76] D. Pires, J. L. Hedrick, A. De Silva, J. Frommer, B. Gotsmann, H. Wolf, M. Despont, U. Duerig, and A. W. Knoll, "Nanoscale Three-Dimensional Patterning of Molecular Resists by Scanning Probes," *Science*, vol. 328, pp. 732–735, 2010.

[77] Y. Lisunova, M. Spieser, R. Juttin, F. Holzner, and J. Brugger, "High-aspect ratio nanopatterning via combined thermal scanning probe lithography and dry etching," *Microelectronic Engineering*, vol. 180, pp. 20–24, 2017.

[78] M. Pace, "KOH Silicon Etch Calculator," *Web, accessed: Nov. 2015*, p. http://lelandstanfordjunior.com/KOH.html, 2013.

[79] R. C. Zeller and R. O. Pohl, "Thermal Conductivity and Specific Heat of Noncrystalline Solids," *Physical Review B*, vol. 4, pp. 2029–2041, 1971.

[80] B. L. Zink and F. Hellman, "Specific heat and thermal conductivity of low-stress amorphous Si-N membranes," *Solid State Communications*, vol. 129, no. 3, pp. 199–204, 2004.

[81] H. Chen, V. V. Ginzburg, J. Yang, Y. Yang, W. Liu, Y. Huang, L. Du, and B. Chen, "Thermal conductivity of polymer-based composites: Fundamentals and applications," *Progress in Polymer Science*, vol. 59, pp. 41–85, 2015.

[82] J. De Winter, A. P. Dove, A. Knoll, P. Gerbaux, P. Dubois, and O. Coulembier, "Control over molar mass, dispersity, end-groups and kinetics in cyclopolymerization of ortho-phthalaldehyde: adapted choice of a phosphazene organocatalyst," *Polym. Chem.*, vol. 5, no. 3, pp. 706–711, 2014.

Bibliography

[83] F. Holzner, *Thermal scanning probe lithography using polyphthalaldehyde.* PhD thesis, ETH Zürich, 2013.

[84] H. Ito and R. Schwalm, "Thermally Developable, Positive Resist Systems with High Sensitivity," *Journal of The Electrochemical Society*, vol. 136, no. 1, pp. 241–245, 1989.

[85] P.-O. Chapuis, J.-J. Greffet, K. Joulain, and S. Volz, "Heat transfer between a nano-tip and a surface," *Nanotechnology*, vol. 17, pp. 2978–2981, 2006.

[86] J. P. Mulet, K. Joulain, R. Carminati, and J. J. Greffet, "Nanoscale radiative heat transfer between a small particle and a plane surface," *Applied Physics Letters*, vol. 78, no. 19, pp. 2931–2933, 2001.

[87] B. Gotsmann, U. Duerig, J. Frommer, and C. J. Hawker, "Exploiting Chemical Switching in a Diels–Alder Polymer for Nanoscale Probe Lithography and Data Storage," *Advanced Functional Materials*, vol. 16, pp. 1499–1505, 2006.

[88] B. A. Nelson and W. P. King, "Modeling and Simulation of the Interface Temperature Between a Heated Silicon Tip and a Substrate," *Nanoscale and Microscale Thermophysical Engineering*, vol. 12, no. 1, pp. 98–115, 2008.

[89] A. Duncan and G. Peterson, "Review of microscale heat transfer," *Appl. Mech. Rev.*, vol. 47, no. 9, pp. 397–428, 1994.

[90] D. Y. Tzou, *Macro- to Microscale Heat Transfer.* Chichester, UK: John Wiley & Sons Ltd, 2 edition ed., 2014.

[91] B. Gotsmann and M. a. Lantz, "Quantized thermal transport across contacts of rough surfaces," *Nature Materials*, vol. 12, no. 1, pp. 59–65, 2012.

[92] D. Bartholomeusz, R. Boutté, and J. Andrade, "Xurography: rapid prototyping of microstructures using a cutting plotter," *Journal of Microelectromechanical Systems*, vol. 14, pp. 1364–1374, 2005.

[93] K. R. Williams, K. Gupta, and M. Wasilik, "Etch rates for micromachining processing-part II," *Journal of Microelectromechanical Systems*, vol. 12, pp. 761–778, 2003.

[94] Z. D. Blount, "The unexhausted potential of E. coli," *eLife*, vol. 4, pp. 1–12, 2015.

[95] E. Rojas, J. a. Theriot, and K. C. Huang, "Response of Escherichia coli growth rate to osmotic shock," *Proceedings of the National Academy of Sciences*, vol. 111, pp. 7807–7812, 2014.

[96] T. S. Ursell, J. Nguyen, R. D. Monds, A. Colavin, G. Billings, N. Ouzounov, Z. Gitai, J. W. Shaevitz, and K. C. Huang, "Rod-like bacterial shape is maintained by feedback between cell curvature and cytoskeletal localization," *Proceedings of the National Academy of Sciences*, vol. 111, pp. E1025–E1034, 2014.

[97] Y. Abe, P. Polyakov, S. Skali-Lami, and G. Francius, "Elasticity and physico-chemical properties during drinking water biofilm formation," *Biofouling*, vol. 27, no. 7, pp. 739–750, 2011.

[98] H. H. Tuson, G. K. Auer, L. D. Renner, M. Hasebe, C. Tropini, M. Salick, W. C. Crone, A. Gopinathan, K. C. Huang, and D. B. Weibel, "Measuring the stiffness of bacterial cells from growth rates in hydrogels of tunable elasticity," *Molecular Microbiology*, vol. 84, pp. 874–891, 2012.

[99] H.-J. Butt, B. Cappella, and M. Kappl, "Force measurements with the atomic force microscope: Technique, interpretation and applications," *Surface Science Reports*, vol. 59, pp. 1–152, 2005.

[100] L. R. Huang, "Continuous Particle Separation Through Deterministic Lateral Displacement," *Science*, vol. 304, pp. 987–990, 2004.

[101] C. Wyatt Shields IV, C. D. Reyes, and G. P. López, "Microfluidic cell sorting: a review of the advances in the separation of cells from debulking to rare cell isolation," *Lab Chip*, vol. 15, pp. 1230–1249, 2015.

[102] J. W. Schroeder and L. A. Simmons, "Complete Genome Sequence of Bacillus subtilis Strain PY79," *Genome Announcements*, vol. 1, p. 1, 2013.

[103] M. T. Cabeen and C. Jacobs-Wagner, "Bacterial cell shape," *Nature Reviews Microbiology*, vol. 3, pp. 601–610, 2005.

[104] M. G. Pinho, M. Kjos, and J.-W. Veening, "How to get (a)round: mechanisms controlling growth and division of coccoid bacteria," *Nature Reviews Microbiology*, vol. 11, pp. 601–614, 2013.

[105] J. M. Skerker and M. T. Laub, "Cell-cycle progression and the generation of asymmetry in Caulobacter crescentus," *Nature Reviews Microbiology*, vol. 2, pp. 325–337, 2004.

[106] K. M. Douglass, C. Sieben, A. Archetti, A. Lambert, and S. Manley, "Super-resolution imaging of multiple cells by optimized flat-field epi-illumination," *Nature Photonics*, vol. 10, no. 11, pp. 705–708, 2016.

[107] A. Gahlmann and W. E. Moerner, "Exploring bacterial cell biology with single-molecule tracking and super-resolution imaging," *Nature Reviews Microbiology*, vol. 12, no. 1, pp. 9–22, 2013.

[108] S. Ardissone, C. Fumeaux, M. Bergé, A. Beaussart, L. Théraulaz, S. K. Radhakrishnan, Y. F. Dufrêne, and P. H. Viollier, "Cell cycle constraints on capsulation and bacteriophage susceptibility," *eLife*, vol. 3, pp. 1–30, 2014.

[109] F. Baquero, J. M. Beltren, and E. Loza, "A review of antibiotic resistance patterns of Streptococcus pneumoniae in Europe," *Journal of Antimicrobial Chemotherapy*, vol. 28, pp. 31–38, 1991.

[110] O. Massidda, L. Nováková, and W. Vollmer, "From models to pathogens: How much have we learned about Streptococcus pneumoniae cell division?," *Environmental Microbiology*, vol. 15, no. 12, pp. 3133–3157, 2013.

[111] D. W. Adams, L. J. Wu, and J. Errington, "Cell cycle regulation by the bacterial nucleoid," *Current Opinion in Microbiology*, vol. 22, pp. 94–101, 2014.

[112] L. J. Wu and J. Errington, "Nucleoid occlusion and bacterial cell division," *Nature Reviews Microbiology*, vol. 10, no. 1, pp. 8–12, 2011.

[113] D. Fadda, A. Santona, V. D'Ulisse, P. Ghelardini, M. G. Ennas, M. B. Whalen, and O. Massidda, "Streptococcus pneumoniae DivIVA: Localization and Interactions in a MinCD-Free Context," *Journal of Bacteriology*, vol. 189, pp. 1288–1298, 2007.

[114] R. van Raaphorst, M. Kjos, and J.-W. Veening, "Chromosome segregation drives division site selection in Streptococcus pneumoniae," *Proceedings of the National Academy of Sciences*, vol. 114, pp. E5959–E5968, 2017.

[115] W. Margolin, "FtsZ and the division of prokaryotic cells and organelles," *Nature Reviews Molecular Cell Biology*, vol. 6, pp. 862–871, 2005.

[116] A. P. Harrison, "Acidiphilium cryptum gen. nov., sp. nov., Heterotrophic Bacterium From Acidic Mineral Environments," *International Journal of Systematic Bacteriology*, vol. 31, no. 3, pp. 327–332, 1981.

[117] B. M. Goebel and E. Stackebrandt, "Cultural and phylogenetical analysis of mixed microbial populations found in natural and commercial bioleaching environments," *Appl Environ Microbiol*, vol. 60, no. 5, pp. 1614–1621, 1994.

[118] Y. F. Dufrêne, "Atomic Force Microscopy in Microbiology: New Structural and Functional Insights into the Microbial Cell Surface," *mBio*, vol. 5, pp. 1–14, 2014.

[119] G. Longo and S. Kasas, "Effects of antibacterial agents and drugs monitored by atomic force microscopy," *Wiley Interdisciplinary Reviews: Nanomedicine and Nanobiotechnology*, vol. 6, pp. 230–244, 2014.

Bibliography

[120] P. C. Braga and D. Ricci, "Atomic Force Microscopy : Application to Investigation of Escherichia coli Morphology before and after Exposure to Cefodizime," *Antimicrobial agents and chemotherapy*, vol. 42, no. 1, pp. 18–22, 1998.

[121] G. Francius, O. Domenech, M. P. Mingeot-Leclercq, and Y. F. Dufrêne, "Direct observation of Staphylococcus aureus cell wall digestion by lysostaphin," *Journal of Bacteriology*, vol. 190, no. 24, pp. 7904–7909, 2008.

[122] S. Pistolesi, R. Pogni, and J. B. Feix, "Membrane Insertion and Bilayer Perturbation by Antimicrobial Peptide CM15," *Biophysical Journal*, vol. 93, pp. 1651–1660, 2007.

[123] R. E. W. Hancock and D. S. Chapple, "Peptide Antibiotics," *Antimicrobial agents and chemotherapy*, vol. 43, no. 6, pp. 1317–1323, 1999.

[124] Y. J. Gordon, E. G. Romanowski, and A. M. McDermott, "A Review of Antimicrobial Peptides and Their Therapeutic Potential as Anti-Infective Drugs," *Current Eye Research*, vol. 30, pp. 505–515, 2005.

[125] M. Zasloff, "Antimicrobial peptides of multicellular organisms," *Nature*, vol. 415, pp. 389–395, 2002.

[126] R. Hancock and A. Patrzykat, "Clinical Development of Cationic Antimicrobial Peptides: From Natural to Novel Antibiotics," *Current Drug Target -Infectious Disorders*, vol. 2, pp. 79–83, 2002.

[127] F. C. O. Los, T. M. Randis, R. V. Aroian, and A. J. Ratner, "Role of Pore-Forming Toxins in Bacterial Infectious Diseases," *Microbiology and Molecular Biology Reviews*, vol. 77, pp. 173–207, 2013.

[128] D. I. Andersson and D. Hughes, "Antibiotic resistance and its cost: is it possible to reverse resistance?," *Nature Reviews Microbiology*, vol. 8, pp. 260–271, 2010.

[129] H. C. Neu, "The crisis in antibiotic resistance.," *Science*, vol. 257, pp. 1064–73, 1992.

[130] V. M. D'Costa, C. E. King, L. Kalan, M. Morar, W. W. L. Sung, C. Schwarz, D. Froese, G. Zazula, F. Calmels, R. Debruyne, G. B. Golding, H. N. Poinar, and G. D. Wright, "Antibiotic resistance is ancient," *Nature*, vol. 477, pp. 457–461, 2011.

[131] J. H. Rex, "ND4BB: addressing the antimicrobial resistance crisis," *Nature Reviews Microbiology*, vol. 12, pp. 231–232, 2014.

[132] K. A. Brogden, "Antimicrobial peptides: pore formers or metabolic inhibitors in bacteria?," *Nature Reviews Microbiology*, vol. 3, pp. 238–250, 2005.

[133] M. D. Peraro and F. G. van der Goot, "Pore-forming toxins: ancient, but never really out of fashion," *Nature Reviews Microbiology*, vol. 14, pp. 77–92, 2015.

[134] M. R. Yeaman and N. Y. Yount, "Mechanisms of Antimicrobial Peptide Action and Resistance," *Pharmacological reviews*, vol. 55, no. 1, pp. 27–55, 2003.

[135] C. D. Fjell, J. A. Hiss, R. E. W. Hancock, and G. Schneider, "Designing antimicrobial peptides: form follows function," *Nature Reviews Drug Discovery*, vol. 11, pp. 37–51, 2011.

[136] H. Sato and J. B. Feix, "Osmoprotection of bacterial cells from toxicity caused by antimicrobial hybrid peptide CM15," *Biochemistry*, vol. 45, no. 33, pp. 9997–10007, 2006.

[137] S. Williams, Y. Hong, D. Danavall, M. Howard-Jones, D. Gibson, M. Frischer, and P. Verity, "Distinguishing between living and nonliving bacteria: Evaluation of the vital stain propidium iodide and its combined use with molecular probes in aquatic samples," *Journal of Microbiological Methods*, vol. 32, pp. 225–236, 1998.

[138] H. M. Davey and P. Hexley, "Red but not dead? Membranes of stressed Saccharomyces cerevisiae are permeable to propidium iodide," *Environmental Microbiology*, vol. 13, no. 1, pp. 163–171, 2011.

[139] P. Stiefel, S. Schmidt-Emrich, K. Maniura-Weber, and Q. Ren, "Critical aspects of using bacterial cell viability assays with the fluorophores SYTO9 and propidium iodide," *BMC Microbiology*, vol. 15, pp. 1–9, 2015.

[140] J. N. Lee, C. Park, and G. M. Whitesides, "Solvent Compatibility of Poly(dimethylsiloxane)-Based Microfluidic Devices," *Analytical Chemistry*, vol. 75, pp. 6544–6554, 2003.

[141] E. C. Hett and E. J. Rubin, "Bacterial Growth and Cell Division: a Mycobacterial Perspective," *Microbiology and Molecular Biology Reviews*, vol. 72, pp. 126–156, 2008.

[142] N. Wang, Y. Cai, and R. Zhang, "Growth of nanowires," *Materials Science and Engineering: R: Reports*, vol. 60, pp. 1–51, 2008.

[143] Y. Xia, P. Yang, Y. Sun, Y. Wu, B. Mayers, B. Gates, Y. Yin, F. Kim, and H. Yan, "One-Dimensional Nanostructures: Synthesis, Characterization, and Applications," *Advanced Materials*, vol. 15, pp. 353–389, 2003.

[144] R. S. Wagner and W. C. Ellis, "Vapor-liquid-solid mechanism of single crystal growth," *Applied Physics Letters*, vol. 4, pp. 89–90, 1964.

[145] A. M. Morales and C. M. Lieber, "A Laser Ablation Method for the Synthesis of Crystalline Semiconductor Nanowires," *Science*, vol. 279, pp. 208–211, 1998.

[146] Y. Xing, Z. Xi, X. Zhang, J. Song, R. Wang, J. Xu, Z. Xue, and D. Yu, "Thermal evaporation synthesis of zinc oxide nanowires," *Applied Physics A*, vol. 80, pp. 1527–1530, 2005.

[147] R. He and P. Yang, "Giant piezoresistance effect in silicon nanowires," *Nature Nanotechnology*, vol. 1, pp. 42–46, 2006.

[148] R. He, X. L. Feng, M. L. Roukes, and P. Yang, "Self-transducing silicon nanowire electromechanical systems at room temperature.," *Nano letters*, vol. 8, pp. 1756–61, 2008.

[149] C. Pang, G.-y. Lee, T.-i. Kim, S. M. Kim, H. N. Kim, S.-H. Ahn, and K.-Y. Suh, "A flexible and highly sensitive strain-gauge sensor using reversible interlocking of nanofibres," *Nature Materials*, vol. 11, no. 8, pp. 1–7, 2012.

[150] F. Puppo, M.-A. Doucey, J.-F. Delaloye, T. S. Y. Moh, G. Pandraud, P. M. Sarro, G. De Micheli, and S. Carrara, "SiNW-FET in-Air Biosensors for High Sensitive and Specific Detection in Breast Tumor Extract," *IEEE Sensors Journal*, vol. 16, pp. 3374–3381, 2016.

[151] E. B. Alaca, "Integration of one-dimensional nanostructures with microsystems: an overview," *International Materials Reviews*, vol. 54, pp. 245–282, 2009.

[152] P. E. Allain, F. Parrain, A. Bosseboeuf, S. Maaroufi, P. Coste, and A. Walther, "Large-Range MEMS Motion Detection With Subangström Noise Level Using an Integrated Piezoresistive Silicon Nanowire," *Journal of Microelectromechanical Systems*, vol. 22, pp. 716–722, 2013.

[153] M. Zervas, D. Sacchetto, G. D. Micheli, and Y. Leblebici, "Microelectronic Engineering Top-down fabrication of very-high density vertically stacked silicon nanowire arrays with low temperature budget," *Microelectronic Engineering*, vol. 88, no. 10, pp. 3127–3132, 2011.

[154] K. a. Shaw, Z. Zhang, and N. C. MacDonald, "SCREAM I: A single mask, single-crystal silicon, reactive ion etching process for microelectromechanical structures," *Sensors and Actuators A: Physical*, vol. 40, pp. 63–70, 1994.

[155] Z. Tasdemir, O. Peric, D. Sacchetto, G. E. Fantner, Y. Leblebici, and B. E. Alaca, "Monolithic Fabrication of Silicon Nanowires Bridging Thick Silicon Structures," *IEEE Nanotechnology Express*, vol. 1, no. November, pp. 2–5, 2015.

Bibliography

[156] Z. Tasdemir, N. Wollschläger, W. Österle, Y. Leblebici, and B. E. Alaca, "A deep etching mechanism for trench-bridging silicon nanowires," *Nanotechnology*, vol. 27, pp. 1–8, 2016.

[157] H. J. Butt and M. Jaschke, "Calculation of thermal noise in atomic force microscopy," *Nanotechnology*, vol. 6, pp. 1–7, 1995.

[158] J. L. Hutter, "Comment on Tilt of Atomic Force Microscope Cantilevers: Effect on Spring Constant and Adhesion Measurements," *Langmuir*, vol. 21, pp. 2630–2632, 2005.

[159] D. a. Walters, J. P. Cleveland, N. H. Thomson, P. K. Hansma, M. a. Wendman, G. Gurley, and V. Elings, "Short cantilevers for atomic force microscopy," *Review of Scientific Instruments*, vol. 67, pp. 3583–3590, 1996.

[160] M. a. Hopcroft, W. D. Nix, and T. W. Kenny, "What is the Young's Modulus of Silicon?," *Journal of Microelectromechanical Systems*, vol. 19, pp. 229–238, 2010.

[161] H. S. Park and P. A. Klein, "Surface stress effects on the resonant properties of metal nanowires: The importance of finite deformation kinematics and the impact of the residual surface stress," *Journal of the Mechanics and Physics of Solids*, vol. 56, pp. 3144–3166, 2008.

[162] Q. Wu, A. A. Volinsky, L. Qiao, and Y. Su, "Surface effects on static bending of nanowires based on non-local elasticity theory," *Progress in Natural Science: Materials International*, vol. 25, no. 5, pp. 520–524, 2015.

[163] H. F. Zhan and Y. T. Gu, "Modified beam theories for bending properties of nanowires considering surface/intrinsic effects and axial extension effect," *Journal of Applied Physics*, vol. 111, pp. 1–9, 2012.

[164] Y. E. Yaish, Y. Calahorra, O. Shtempluck, and V. Kotchetkov, "Three-point bending analysis of doubly clamped silicon nanowire beams; Young's modulus, initial stress, and crystal orientation," *Journal of Applied Physics*, vol. 117, pp. 1–11, 2015.

[165] A. Heidelberg, L. T. Ngo, B. Wu, M. A. Phillips, S. Sharma, T. I. Kamins, J. E. Sader, and J. J. Boland, "A Generalized Description of the Elastic Properties of Nanowires," *Nano Letters*, vol. 6, pp. 1101–1106, 2006.

[166] B. Wen, J. E. Sader, and J. J. Boland, "Mechanical properties of ZnO nanowires," *Physical Review Letters*, vol. 101, no. October, pp. 2–5, 2008.

[167] B. Wu, A. Heidelberg, and J. J. Boland, "Mechanical properties of ultrahigh-strength gold nanowires," *Nature Materials*, vol. 4, pp. 525–529, 2005.

[168] Q. Xiong, N. Duarte, S. Tadigadapa, and P. C. Eklund, "Force-Deflection Spectroscopy: A New Method to Determine the Young's Modulus of Nanofilaments," *Nano Letters*, vol. 6, pp. 1904–1909, 2006.

[169] Y. Calahorra, O. Shtempluck, V. Kotchetkov, and Y. E. Yaish, "Young's Modulus, Residual Stress, and Crystal Orientation of Doubly Clamped Silicon Nanowire Beams," *Nano Letters*, vol. 15, pp. 2945–2950, 2015.

[170] J. L. Drury and D. J. Mooney, "Hydrogels for tissue engineering: scaffold design variables and applications," *Biomaterials*, vol. 24, pp. 4337–4351, 2003.

[171] K. Y. Lee and D. J. Mooney, "Hydrogels for Tissue Engineering," *Chemical Reviews*, vol. 101, pp. 1869–1880, 2001.

[172] A. S. Hoffman, "Hydrogels for biomedical applications," *Advanced Drug Delivery Reviews*, vol. 64, pp. 18–23, 2012.

[173] G. D. Nicodemus and S. J. Bryant, "Cell Encapsulation in Biodegradable Hydrogels for Tissue Engineering Applications," *Tissue Engineering Part B: Reviews*, vol. 14, pp. 149–165, 2008.

[174] A. Béduer, T. Braschler, O. Peric, G. E. Fantner, S. Mosser, P. C. Fraering, S. Benchérif, D. J. Mooney, and P. Renaud, "A Compressible Scaffold for Minimally Invasive Delivery of Large Intact Neuronal Networks," *Advanced Healthcare Materials*, vol. 4, pp. 301–312, 2015.

[175] S. Kondo, T. Hiroi, Y.-S. Han, T.-H. Kim, M. Shibayama, U.-i. Chung, and T. Sakai, "Reliable Hydrogel with Mechanical "Fuse Link" in an Aqueous Environment," *Advanced Materials*, vol. 27, pp. 7407–7411, 2015.

[176] S. R. Caliari and J. A. Burdick, "A practical guide to hydrogels for cell culture," *Nature Methods*, vol. 13, no. 5, pp. 405–414, 2016.

[177] S. a. Bencherif, R. W. Sands, D. Bhatta, P. Arany, C. S. Verbeke, D. a. Edwards, and D. J. Mooney, "Injectable preformed scaffolds with shape-memory properties," *Proceedings of the National Academy of Sciences*, vol. 109, pp. 19590–19595, 2012.

[178] S. Kriks, J.-W. Shim, J. Piao, Y. M. Ganat, D. R. Wakeman, Z. Xie, L. Carrillo-Reid, G. Auyeung, C. Antonacci, A. Buch, L. Yang, M. F. Beal, D. J. Surmeier, J. H. Kordower, V. Tabar, and L. Studer, "Dopamine neurons derived from human ES cells efficiently engraft in animal models of Parkinson's disease," *Nature*, vol. 480, pp. 1–7, 2011.

[179] K. van Kuyck, M. Welkenhuysen, L. Arckens, R. Sciot, and B. Nuttin, "Histological Alterations Induced by Electrode Implantation and Electrical Stimulation in the Human Brain: A Review," *Neuromodulation: Technology at the Neural Interface*, vol. 10, pp. 244–261, 2007.

[180] P. B. Welzel, J. Friedrichs, M. Grimmer, S. Vogler, U. Freudenberg, and C. Werner, "Cryogel Micromechanics Unraveled by Atomic Force Microscopy-Based Nanoindentation," *Advanced Healthcare Materials*, vol. 3, pp. 1849–1853, 2014.

[181] Z. Taylor and K. Miller, "Reassessment of brain elasticity for analysis of biomechanisms of hydrocephalus," *Journal of Biomechanics*, vol. 37, pp. 1263–1269, 2004.

[182] P. Moshayedi, G. Ng, J. C. Kwok, G. S. Yeo, C. E. Bryant, J. W. Fawcett, K. Franze, and J. Guck, "The relationship between glial cell mechanosensitivity and foreign body reactions in the central nervous system," *Biomaterials*, vol. 35, pp. 3919–3925, 2014.

[183] H. Kamata, Y. Akagi, Y. Kayasuga-Kariya, U.-i. Chung, and T. Sakai, ""Nonswellable" Hydrogel Without Mechanical Hysteresis," *Science*, vol. 343, pp. 873–875, 2014.

[184] J.-Y. Sun, X. Zhao, W. R. K. Illeperuma, O. Chaudhuri, K. H. Oh, D. J. Mooney, J. J. Vlassak, and Z. Suo, "Highly stretchable and tough hydrogels," *Nature*, vol. 489, pp. 133–136, 2012.

[185] S. Kondo, H. Sakurai, U.-i. Chung, and T. Sakai, "Mechanical Properties of Polymer Gels with Bimodal Distribution in Strand Length," *Macromolecules*, vol. 46, pp. 7027–7033, 2013.

[186] T. Sakai, T. Matsunaga, Y. Yamamoto, C. Ito, R. Yoshida, S. Suzuki, N. Sasaki, M. Shibayama, and U.-i. Chung, "Design and Fabrication of a High-Strength Hydrogel with Ideally Homogeneous Network Structure from Tetrahedron-like Macromonomers," *Macromolecules*, vol. 41, pp. 5379–5384, 2008.

[187] B. Pittenger, N. Erina, and C. Su, "Quantitative Mechanical Property Mapping at the Nanoscale with PeakForce QNM," tech. rep., Veeco, 2009.

[188] J. D. Adams, B. W. Erickson, J. Grossenbacher, J. Brugger, A. Nievergelt, and G. E. Fantner, "Harnessing materials damping properties for high-speed atomic force microscopy," *Nature nanotechnology*, vol. in press, no. November, pp. 1–6, 2015.

[189] T. Ando, T. Uchihashi, and N. Kodera, "High-Speed AFM and Applications to Biomolecular Systems," *Annual Review of Biophysics*, vol. 42, pp. 393–414, 2013.

[190] J. E. Sader, "Frequency response of cantilever beams immersed in viscous fluids with applications to the atomic force microscope," *Journal of Applied Physics*, vol. 84, pp. 64–76, 1998.

[191] T. E. Schäffer, J. P. Cleveland, F. Ohnesorge, D. A. Walters, and P. K. Hansma, "Studies of vibrating atomic force microscope cantilevers in liquid," *Journal of Applied Physics*, vol. 80, pp. 3622–3627, 1996.

[192] H. Butt, P. Siedle, K. Seifert, K. Fendler, T. Seeger, E. Bamberg, and A. L. Weisenhorn, "Scan speed limit in atomic force microscopy," *Journal of Microscopy*, vol. 169, pp. 75–84, 1992.

[193] G. Y. Chen, R. J. Warmack, T. Thundat, D. P. Allison, and A. Huang, "Resonance response of scanning force microscopy cantilevers," *Review of Scientific Instruments*, vol. 65, no. 8, pp. 2532–2537, 1994.

[194] T. Ando, N. Kodera, E. Takai, D. Maruyama, K. Saito, and A. Toda, "A high-speed atomic force microscope for studying biological macromolecules," *Proceedings of the National Academy of Sciences*, vol. 98, pp. 12468–12472, 2001.

[195] S. Alexander, L. Hellemans, O. Marti, J. Schneir, V. Elings, P. K. Hansma, M. Longmire, and J. Gurley, "An atomic-resolution atomic-force microscope implemented using an optical lever," *Journal of Applied Physics*, vol. 65, pp. 164–167, 1989.

[196] G. Meyer and N. M. Amer, "Novel optical approach to atomic force microscopy," *Applied Physics Letters*, vol. 53, pp. 1045–1047, 1988.

[197] M. Li, H. X. Tang, and M. L. Roukes, "Ultra-sensitive NEMS-based cantilevers for sensing, scanned probe and very high-frequency applications," *Nature Nanotechnology*, vol. 2, pp. 114–120, 2007.

[198] A. Boisen, O. Hansen, and S. Bouwstra, "AFM probes with directly fabricated tips," *Journal of Micromechanics and Microengineering*, vol. 6, no. 1, pp. 58–62, 1999.

[199] T. R. Albrecht, S. Akamine, T. E. Carver, and C. F. Quate, "Microfabrication of cantilever styli for the atomic force microscope," *Journal of Vacuum Science & Technology A: Vacuum, Surfaces, and Films*, vol. 8, pp. 3386–3396, 1990.

[200] Y. Mitsuoka, T. Niwa, S. Ichihara, K. Kato, H. Muramatsu, K. Nakajima, M. Shikida, and K. Sato, "Microfabricated silicon dioxide cantilever with subwavelength aperture," *Journal of Microscopy*, vol. 202, pp. 12–15, 2001.

[201] R. J. Grow, S. C. Minne, S. R. Manalis, and C. F. Quate, "Silicon nitride cantilevers with oxidation-sharpened silicon tips for atomic force microscopy," *Journal of Microelectromechanical Systems*, vol. 11, no. 4, pp. 317–321, 2002.

[202] M. B. Viani, T. E. Schaffer, A. Chand, M. Rief, H. E. Gaub, and P. K. Hansma, "Small cantilevers for force spectroscopy of single molecules," *Journal of Applied Physics*, vol. 86, no. 4, pp. 2258–2262, 1999.

[203] G. Genolet, J. Brugger, M. Despont, U. Drechsler, P. Vettiger, N. F. de Rooij, and D. Anselmetti, "Soft, entirely photoplastic probes for scanning force microscopy," *Review of Scientific Instruments*, vol. 70, pp. 2398–2401, 1999.

[204] E. Ammar and T. Rodgers, "UMOS Transistors on (100) Silicon," *IEEE Transactions on Electron Devices*, vol. 27, pp. 907–914, 1980.

[205] T. Rodgers, R. Hiltpold, J. Zimmer, G. Marr, and J. Trotter, "VMOS ROM," *IEEE Journal of Solid-State Circuits*, vol. 11, pp. 614–622, 1976.

[206] R. B. Marcus and T. T. Sheng, "The Oxidation of Shaped Silicon Surfaces," *Journal of The Electrochemical Society*, vol. 129, no. 6, pp. 1278–1282, 1982.

[207] F. Niklaus, P. Enoksson, E. Kälvesten, and G. Stemme, "Low-temperature full wafer adhesive bonding," *Journal of Micromechanics and Microengineering*, vol. 11, no. 2, pp. 100–107, 2001.

[208] P. Chinoy, "Reactive ion etching of benzocyclobutene polymer films," *IEEE Transactions on Components, Packaging, and Manufacturing Technology: Part C,* vol. 20, pp. 199–206, 1997.

[209] J. Oberhammer, F. Niklaus, and G. Stemme, "Selective wafer-level adhesive bonding with benzocyclobutene for fabrication of cavities," *Sensors and Actuators, A: Physical,* vol. 105, no. 3, pp. 297–304, 2003.

[210] T. S. Ravi, "Oxidation sharpening of silicon tips," *Journal of Vacuum Science & Technology B: Microelectronics and Nanometer Structures,* vol. 9, no. 6, pp. 2733–2737, 1991.

[211] M. Kitazawa, K. Shiotani, and A. Toda, "Batch Fabrication of Sharpened Silicon Nitride Tips," *Japanese Journal of Applied Physics,* vol. 42, pp. 4844–4847, 2003.

[212] M. G. L. Gustafsson and J. Clarke, "Scanning force microscope springs optimized for optical-beam deflection and with tips made by controlled fracture," *Journal of Applied Physics,* vol. 76, pp. 172–181, 1994.

[213] Y. Akama, E. Nishimura, A. Sakai, and H. Murakami, "New scanning tunneling microscopy tip for measuring surface topography," *Journal of Vacuum Science & Technology A: Vacuum, Surfaces, and Films,* vol. 8, pp. 429–433, 1990.

[214] D. J. Keller and C. Chih-Chung, "Imaging steep, high structures by scanning force microscopy with electron beam deposited tips," *Surface Science,* vol. 268, pp. 333–339, 1992.

[215] D. S. Engstrom, V. Savu, X. Zhu, I. Y. Y. Bu, W. I. Milne, J. Brugger, and P. Boggild, "High Throughput Nanofabrication of Silicon Nanowire and Carbon Nanotube Tips on AFM Probes by Stencil-Deposited Catalysts," *Nano Letters,* vol. 11, pp. 1568–1574, 2011.

[216] K. Bean, "Anisotropic etching of silicon," *IEEE Transactions on Electron Devices,* vol. 25, pp. 1185–1193, 1978.

[217] D. Nečas and P. Klapetek, "Gwyddion: an open-source software for SPM data analysis," *Open Physics,* vol. 10, pp. 181–188, 2012.

[218] M. Dukic, J. D. Adams, and G. E. Fantner, "Piezoresistive AFM cantilevers surpassing standard optical beam deflection in low noise topography imaging," *Scientific Reports,* vol. 5, p. 16393, 2015.

[219] G. E. Fantner, D. J. Burns, A. M. Belcher, I. W. Rangelow, and K. Youcef-Toumi, "DMCMN: In Depth Characterization and Control of AFM Cantilevers With Integrated Sensing and Actuation," *Journal of Dynamic Systems, Measurement, and Control,* vol. 131, no. 6, p. 061104, 2009.

[220] S. Y. Chou and P. R. Krauss, "Imprint lithography with sub-10 nm feature size and high throughput," *Microelectronic Engineering,* vol. 35, pp. 237–240, 1997.

[221] R. Pelzer, C. Gourgon, S. Landis, and P. Kettner, "Nanoimprint Lithography - Full Wafer Replication of Nanometer Features," *Proc. of SPIE,* vol. 5650, pp. 256–259, 2005.

[222] S. Y. Chou, C. Keimel, and J. Gu, "Ultrafast and direct imprint of nanostructures in silicon," *Nature,* vol. 417, pp. 835–837, 2002.

[223] H. Schift, S. Park, B. Jung, C.-G. Choi, C.-S. Kee, S.-P. Han, K.-B. Yoon, and J. Gobrecht, "Fabrication of polymer photonic crystals using nanoimprint lithography," *Nanotechnology,* vol. 16, pp. S261–S265, 2005.

[224] J. Kitzinger, "Qualitative Research: Introducing focus groups," *BMJ,* vol. 311, pp. 299–302, 1995.

[225] R. A. Krueger and M. A. Casey, "Designing and conducting focus group interviews," in *Social analysis, selected tools and techniques,* ch. 2, pp. 4–24, Washington, DC: Social Development Department, The World Bank, 2002.

Bibliography

[226] R. A. Krueger and M. A. Casey, "Participants in a Focus Group," in *Focus groups: A practical guide for applied research*, ch. 4, pp. 63–83, Sage Publications, 2009.

[227] C. S. Nowell, P. D. Odermatt, L. Azzolin, S. Hohnel, E. F. Wagner, G. E. Fantner, M. P. Lutolf, Y. Barrandon, S. Piccolo, and F. Radtke, "Chronic inflammation imposes aberrant cell fate in regenerating epithelia through mechanotransduction," *Nature Cell Biology*, no. November, 2015.

[228] D. J. Müller and Y. F. Dufrêne, "Atomic force microscopy - a nanoscopic window on the cell surface," *Trends in Cell Biology*, vol. 21, pp. 461–469, 2011.

[229] L. Chopinet, C. Formosa, M. P. Rols, R. E. Duval, and E. Dague, "Imaging living cells surface and quantifying its properties at high resolution using AFM in QI™ mode.," *Micron*, vol. 48, pp. 26–33, 2013.

[230] H. Cho, T. Uehara, and T. Bernhardt, "Beta-Lactam Antibiotics Induce a Lethal Malfunctioning of the Bacterial Cell Wall Synthesis Machinery," *Cell*, vol. 159, pp. 1300–1311, 2014.

[231] M. Basler, B. T. Ho, and J. J. Mekalanos, "Tit-for-tat: Type VI secretion system counterattack during bacterial cell-cell interactions," *Cell*, vol. 152, no. 4, pp. 884–894, 2013.

[232] B. a. Smith, H. Roy, P. De Koninck, P. Grütter, and Y. De Koninck, "Dendritic spine viscoelasticity and soft-glassy nature: balancing dynamic remodeling with structural stability.," *Biophysical journal*, vol. 92, no. 4, pp. 1419–30, 2007.

[233] J. R. Moffitt, Y. R. Chemla, S. B. Smith, and C. Bustamante, "Recent advances in optical tweezers.," *Annu. Rev. Biochem.*, vol. 77, pp. 205–28, 2008.

Acknowledgements

First of all, I would like to thank my thesis advisor Georg, who guided me during the 5 years of my PhD studies.

I would like express my warmest gratitude to my parents Dragica and Martin, and my brother Karlo for supporting me during all my studies, as well as my girlfriend Stéphanie for all the support during my PhD studies.

My special thanks goes to my flat mate Jamel and my fellow microengineer Philipp for all the immense support, specially during the past 5 years. You were both a huge support for me during my doctoral studies.

I would like to thank Maciek, Philippe and Marc for all the unforgettable moments in my free time outside of the lab, and as well Leo, John, Mylène, Francesca, Andrea and every single person who was a part of the memorable moments around a beer or drinks outside the laboratory.

The studies and adventures at the EPFL in Lausanne I started together with my first flat mate Pascal. It was a wonderful time with lots of interesting and fun projects during our microengineering studies for which I'm truly thankful. My gratitude goes as well to my fellow microengineering study friends Michael, Daniel, and everybody being part of our study community. Also, a huge 'thank you' to all my flat mates during my microengineering and doctoral studies, for all the time spend together. Moreover, I would like to thank Chriggi, Yassine, and Momo for the vacations spent together, reaching up as far as Guam.

I would like to thank my current and former lab mates, Mélanie, Maja, Pascal, Jonathan, Chen, Nahid, Soma, Alex, Joëlle, Santiago, Adrian, Barney, Yulia, Charlène and everybody who was part of our lab, for all the time spend together in the lab and outside during barbecues. I wish you all the best for your future scientific careers. I would also like to express my gratitude to all my collaborators during the doctoral studies, in particular to Thomas, Amélie, Zuhal, and Yuliya for the fruitful outcome of our research.

Acknowledgements

For all the support in the cleanroom, all the technical discussions around microfabrication processes, as well as for all help making the cleanroom fabrication possible, I would like to give a huge compliment to the CMi staff, in particular to Cyrille, Joffrey, Didier, Zdenek, Patrick, and everybody responsible for the trainings and maintenance of the cleanroom machines. It was truly an honor and a pleasure for me to work in the CMi.

My special thanks goes to my mentor, supporting me during my PhD studies.

Finally, I would like to express my gratitude to all the people who brought me here, all the professors, teachers, friend, and family. Thank you all!

Lausanne, 27 July 2017   Oliver Peric

Oliver Peric   15.01.1987

Ch. du Levant 3   Single

1005 Lausanne   Swiss & Croatian

oliver.peric@gmail.com

KEY SKILLS

Team player, fluent in four languages, analytic problem solving, cleanroom microfabrication

EDUCATION

Doctorate in Microsystems, EPFL   10.2012 – (09.2017)

    Specialization in atomic force microscopy, cleanroom fabrication and microbiology

Master of Science in Microengineering, EPFL   10.2006 – 06.2012

    Specialization in Micro- and Nanotechnologies

Minor in Space Technologies, EPFL   10.2010 – 06.2012

Matura in natural sciences, Kantonsschule Rämibühl, MNG, Zürich   08.2001 – 09.2005

EXPERIENCE

Cleanroom microfabrication

    Expertise in cleanroom (ISO 5 / Class 100) fabrication technique including photolithography, electron-beam lithography, isotropic and anisotropic dry and wet etching, scanning electron microscopy (SEM) and atomic force microscopy (AFM) for metrology, and focused ion beam (FIB).

Process optimization

    Optimization of cleanroom processes to yield a device outcome per wafer of **>99 %** and a device design optimization for an output of **+800 %** (126 devices per wafer vs. initially only 14 devices per wafer).

Project development

    Development of an **innovative** cleanroom process flow involving cutting-edge lithography technology with a cost reduction of over **97 %** for initial materials and further decrease of overall production time.

Project management

    Time and cost management of various projects regarding cleanroom microfabrication and laboratory equipment.

Teaching

    Teaching assistant for the EPFL bachelor course *"Structural Mechanics"* with duties for exercise sessions, drafting of exam questions and exam corrections during entire doctoral studies.

Informatics

    Computer-aided design (CAD) software (SolidWorks and Pro/ENGINEER). Wafer design (Clewin); Printed circuit board (PCB) design (EAGLE); Finite element analysis software (COMSOL), Programming (C/C++, Qt, MATLAB). All main office software.

PROJECTS

Laboratory for Bio- and Nano-Instrumentation, Doctoral project, EPFL   10.2012 – (09.2017)

    Development of a microfluidic device for robust immobilization and analysis of bacteria in liquid with nanometer resolution. Medium independent analysis of bacteria was possible with simultaneous fluorescence and atomic force microscopy. As a result, medium-dependent killing activity of antimicrobial peptides was observed on the bacterial envelope.

Microsystems for Space Technologies Laboratory LMTS, Semester project**,** EPFL   09.2011 – 01.2012

   Development of a detector for the characterization of a spacecraft propulsion system based on an ionic liquid electrospray source.

Internship at Universidad del Valle, Cali, Colombia   07.2011 – 09.2011

   Construction of a bioreactor by designing the mechanical layout, implementing sensors by designing the electronic circuits as well as programming the web accessible microcontroller.

Microsystems Laboratory LMIS4, Semester project**,** EPFL   02.2011 – 06.2011

   Development of a hemolymph gathering device combining and expanding knowledge in microfluidics, rapid prototyping and clean room assembly.

Microsystems Laboratory LMIS1, Semester project**,** EPFL   09.2010 – 01.2011

   Research project in the field of dynamic stencil lithography gaining expertise in clean room class 100 work and microstructure analysis using electron microscopy and other tools.

Introduction to Manufacturing, ETML, Lausanne, Switzerland   07.2007 – 08.2007

   Manufacturing of a letter scale designed during the first year of EPFL studies.

EXTRA-CURRICULAR ACTIVITIES

Board of directors in the General Student's Association of EPFL, Lausanne, Switzerland   09.2011 – 06.2012

   Representative of the EPFL students in the Union of Students in Switzerland. My task was to advocate local opinions and interests, and negotiate compromises with other representatives.

Space Development: Theory & Practice International Workshop, Moscow, Russia   07.2010

   This workshop provided an exchange within the Russian space program. We designed a new space station merging Russian and international know-how.

Nokia Research Laboratory (NRC), Lausanne, Switzerland   09.2009 – 01.2010

   For the Nokia Qt course and contest, my team and I developed two applications for mobile platforms, in particular for Symbian S60 and Maemo (Linux) devices.

LANGUAGES

German / Swiss German:	native language
French:	excellent, C2 of European Standard of Languages
English:	excellent, C2
Language studies	Pacific Gateway International College (PGIC), Vancouver, Canada 07.2004 – 08.2004
Croatian:	advanced, C1
Spanish:	basic, A2

PERSONAL INTERESTS

Running (Lausanne Marathon 2014 and 20km 2013 & 2016), Travelling

AWARDS | PUBLICATIONS

Awards

Gold Best Poster Award for poster entitelled "*Microfluidic Bacterial Traps for Simultaneous Fluorescence and Atomic Force Microscopy*", Nano and Micro Systems (NAMIS) Autumn School, Tokyo, Japan; **Sept. 2016**

First place in Nokia Research Laboratory contest, EPFL Innovation Park, Lausanne, Switzerland, **Jan. 2010**

Publications

The full list of publications is available at: https://scholar.google.ch/citations?user=mxkeCxgAAAAJ